

**TOBB UNIVERSITY OF ECONOMICS AND TECHNOLOGY**

**OPTICAL RESONATORS: PHOTONIC NANO-JET AND WHISPERING  
GALLERY MODE**

**DOCTOR OF PHILOSOPHY**

**Ibrahim MAHARIQ**

**Electrical and Electronics Engineering**

**Thesis Advisor: Prof. Dr. Hamza KURT**

**AUGUST 2017**



Approval of the Graduate School of Science and Technology

.....  
**Prof. Dr. Osman EROĞUL**  
Director

I certify that this thesis satisfies all the requirements as a thesis for the degree of Doctor of Philosophy.

.....  
**Assoc. Prof. Dr. Tolga GIRICI**  
Head of Department

The thesis entitled “**OPTICAL RESONATORS: PHOTONIC NANO-JET AND WHISPERING GALLERY MODE**”, by **Ibrahim MAHARIQ**, 131217007 the student of the degree of Doctoral of Philosophy, Graduate school of Natural and Applied Sciences, TOBB ETU, which has been prepared after fulfilling all the necessary conditions determined by the related regulations, has been accepted by the jury, whose signatures are as below, on 02<sup>nd</sup> August, 2017.

**Thesis Advisor:** **Prof. Dr. Hamza KURT** .....  
TOBB Ekonomi ve Teknoloji Üniversitesi

**Jury Members:** **Assoc. Prof. Dr. Ali BOZBEY (Chair)** .....  
TOBB Ekonomi ve Teknoloji Üniversitesi

**Assist. Prof. Dr. İlyas Evrim ÇOLAK** .....  
Ankara Üniversitesi

**Assist. Prof. Dr. Rohat MELİK** .....  
TOBB Ekonomi ve Teknoloji Üniversitesi

**Assist. Prof. Dr. Fikriye Nuray YILMAZ** .....  
Gazi Üniversitesi



## TEZ BİLDİRİMİ

Tez içindeki bütün bilgilerin etik davranış ve akademik kurallar çerçevesinde elde edilerek sunulduğunu, ayrıca tez yazım kurallarına uygun olarak hazırlanan bu çalışmada orijinal olmayan her türlü kaynağa eksiksiz atıf yapıldığını bildiririm.

I hereby declare that all the information provided in this thesis has been obtained with rules of ethical and academic conduct and has been written in accordance with thesis format regulations. I also declare that, as required by these rules and conduct, I have fully cited and referenced all material and results that are not original to this work.

Ibrahim MAHARIQ



## **ABSTRACT**

Doctor of Philosophy

OPTICAL RESONATORS: PHOTONIC NANO-JET AND WHISPERING  
GALLERY MODE

Ibrahim MAHARIQ

TOBB University of Economics and Technology  
Institute of Natural and Applied Sciences  
Electrical and Electronics Engineering

Supervisor: Prof. Dr. Hamza KURT

Date: August 2017

When a dielectric micro-sphere or micro-cylinder is illuminated by an incident plane wave, a strongly focused beam at the shadow side is formed and such phenomenon is known as photonic nanojet. In this thesis, the spectral element method (SEM) is adopted to investigate the behaviour of photonic jets resulting from different structures and excitations. The general formulation of SEM is presented for the sake of numerical modelling of two-dimensional, frequency-domain electromagnetic scattering problems. For the purpose of accuracy demonstration, one- and two-dimensional examples were chosen to show that SEM dominates the finite difference method and finite element method in terms of accuracy. Then, in addition to the successful modelling of photonic jets by SEM, several resonance modes that result in planewave-excited dielectric cylinders are also captured by SEM. Three different scenarios are also considered in the current study in order to verify the strong field confinement; one is under Bessel beam illumination, the second is the introduction of non-homogeneity in the material forming the cylinder, and the third is that the cylinders are excited by a point source. Moreover, nanojets and resonance resulting from hemicylindrical and corrugated cylinders under normally incident plane-wave illumination are studied. Finally, homogenous and isotropic magneto-dielectric micro-cylinders embedded in air background when illuminated by a unit-intensity plane wave are also investigated.

**Keywords:** Electromagnetic waves, Hemi cylinders, Corrugated cylinders, Photonic nanojets, Resonance, Spectral element method, Whispering gallery modes.



## ÖZET

Doktora Tezi

OPTİK REZONATÖRLER: FOTONİK NANO-JET VE FISILDAYAN GALERİ

MODU

Ibrahim MAHARIQ

TOBB Ekonomi ve Teknoloji Üniversitesi  
Fen Bilimleri Enstitüsü  
Elektrik ve Elektronik Mühendisliği

Danışman: Prof. Dr. Hamza KURT

Tarih: Ağustos 2017

Bir dielektrik mikro-küre veya mikro-silindir gelen düzlem dalga tarafından aydınlatıldığında gölge tarafında güçlü bir şekilde odaklanmış bir ışın oluşur ve bu olgu nanojet olarak adlandırılır. Bu tezde, farklı yapılar ve farklı uyartımlar için oluşan fotonik jetlerin davranışlarını incelemek için spektral eleman yöntemi kullanılmıştır. İki boyutlu, frekans domeni elektromanyetik saçılma problemlerinin sayısal modellenmesi için spektral eleman metodunun genel formülasyonu sunulmuştur. Spektral eleman yönteminin, sonlu elemanlar ve sonlu fark yöntemlerinden kesinlik açısından üstünlüğünü göstermek için bir ve iki boyutlu örnekler seçilmiştir. Ardından, fotonik jetlerin SEM ile başarılı şekilde modellenmesine ek olarak birkaç rezonans modu tarafından oluşan düzlem dalga uyartımlı dielektrik silindirler de SEM tarafından modellenmiştir. Güçlü alan kısıtlamasını doğrulamak için üç farklı senaryo dikkate alınmıştır; birincisi Bessel ışın aydınlatması altında, ikincisi silindiri oluşturan materyalin heterojenliğinin ortaya çıkması, üçüncüsü ise nokta kaynaktan uyartılan silindirler. Dahası, normal giren düzlem dalga aydınlatması altında yarı-silindir ve oluklu silindirlerden ortaya çıkan nanojet ve rezonans incelenmiştir. Son olarak, bir birim yoğunluklu düzlem dalga tarafından aydınlatıldığında hava arka planına gömülü homojen ve izotropik manyeto-dielektrik mikro silindirler de araştırılmıştır.

**Anahtar Kelimeler:** Elektromanyetik dalgalar, Yarı silindirler, Oluklu silindirler, Fotonik nanojetler, Rezonans, Spektral eleman yöntemi, Fısıldayan galeri modu.

## ACKNOWLEDGMENTS

First of all, I thank ALLAH who gave me the ability and led me to do this work. I am really indebted to my supervisor Prof. Dr. Hamza Kurt for his guidance, suggestions, criticism, encouragement during the time of research and writing of this thesis. He is really one of the few exceptional teachers whom I met in my life.

I would like to thank Assist. Prof. İlyas Evrim Çolak and Assist. Prof. Dr. Rohat Melik for their evaluations and time spent during the development of this thesis. I also would like to thank the other jury members for gathering and giving me the chance to present my thesis in front of them.

The first year of my study was partially supported by The Scientific and Technological Research Council of Turkey (TÜBİTAK). Here I would like to thank Assoc. Prof. Dr. Ayşe Melda Yüksel Turgut for helping me to be financially supported by TÜBİTAK. I also acknowledge TOBB University of Economics and Technology for the research scholarship they gave to me in the last 3 years.

I really thank all my Turkish and Palestinian colleagues and friends who were very kind and helpful to me. Here, I would like to thank my best friends Ferhat Karagoz, Atakan Erciyas and Ibrahim Arpacı for the motivation, discussions and help I received from them.

Finally, I acknowledge the continuous motivation and the good willing I was receiving from my wife Azhar, sisters, brothers, nephews, cousins and all other relatives. This thesis is dedicated to my parents; Mohammed Mahariq and Naima Mahariq who kept motivating me since my childhood upto this moment. It is also dedicated to my wife who helped me and afforded being in a foreigner country. In addition, the same appreciation and dedication is given to my children: Ahmed, Labib, and Esil. This work is also dedicated to my brothers, sisters, and all my friends and colleagues who wish all the best to me.



## CONTENTS

Sayfa

<b>TEZ BİLDİRİMİ.....</b>	<b>iii</b>
<b>ABSTRACT.....</b>	<b>iv</b>
<b>ÖZET.....</b>	<b>vi</b>
<b>ACKNOWLEDGMENTS .....</b>	<b>viii</b>
<b>CONTENTS.....</b>	<b>ix</b>
<b>LIST OF FIGURES .....</b>	<b>xi</b>
<b>LIST OF TABLES .....</b>	<b>xv</b>
<b>ABBREVIATIONS .....</b>	<b>xvi</b>
<b>LIST OF SYMBOLS .....</b>	<b>xvii</b>
<b>1. INTRODUCTION.....</b>	<b>1</b>
1.1 Brief History About Transparent Spheres .....	1
1.2 What Is A Photonic Nanojet?.....	2
1.3 Solving Maxwell's Equations .....	3
1.4 Contribution Of The Thesis.....	5
1.5 Outline Of The Thesis .....	6
<b>2. SPECTRAL ELEMENT FORMULATION OF ELECTROMAGNETIC SCATTERING .....</b>	<b>7</b>
2.1 Introduction .....	7
2.2 The Governing PDEs.....	8
2.3 SEM Formulation.....	10
2.4 The Accuracy Of SEM, FDM And FEM .....	14
2.5 Conclusion.....	18
<b>3. PHOTONIC NANOJET.....</b>	<b>19</b>
3.1 Numerical Analysis Of Photonic Nanojets .....	19
3.2 Photonic Nanojet Resulting From Dielectric Micro-cylinders.....	21
3.3 Long Photonic Nanojets .....	26
3.4 Whispering Gallery Modes In Dielectric Cylinders.....	27
3.5 Verification Of Whispering Gallery Modes.....	30
3.5 Conclusions .....	32
<b>4. RESONANCE DYNAMICS OF DIELECTRIC CYLINDERS .....</b>	<b>35</b>
4.1 Tuning Optical Resonances Of Dielectric Cylinders .....	35
4.2 Results Of Mie Theory .....	40
4.2.1 Discussions .....	43
4.3 Resonance Under Different Mechanism .....	44
4.4 Resonance Mode Tracking.....	47
4.4.1 Discussions .....	51
4.5 Point Source Illumination.....	52
4.6 Conclusions .....	55
<b>5. CYLINDERS OF DIFFERENT SHAPES AND PROPERTIES.....</b>	<b>57</b>
5.1 Hemi Cylinders.....	57
5.1.1 Introduction .....	57

5.1.2 SEM Results .....	59
5.2 Photonic Nanojet Under The Deformation Of Circular Boundary .....	64
5.2.1 Results of SEM .....	66
5.2.2 Resonance .....	69
5.3 Magnetic Cylinders .....	72
5.3.1 Results of scattered field.....	72
5.4 Conclusion.....	77
<b>6. CONCLUSION.....</b>	<b>79</b>
<b>REFERENCES.....</b>	<b>81</b>
<b>APPENDIX.....</b>	<b>91</b>
<b>CURRICULUM VITAE.....</b>	<b>95</b>



## LIST OF FIGURES

Sayfa

Figure 2. 1: A typical electromagnetic scattering problem composed of a dielectric (or magnetic) scatterer embedded in a free-space region, and domain truncation is performed by the perfectly matched layer.....	9
Figure 2. 2: Mapping an element $\Omega^e$ to the standard element $\Omega^{st}$ .....	12
Figure 2. 3: GLL grid nodes on the reference element for a ninth-order polynomial space (nodes are represented by the intersections of horizontal and vertical lines). .....	14
Figure 2. 4: Plot of first six Legendre polynomials. ....	14
Figure 2. 5: Exact and SEM solutions of the problem defined in Eq. 2.32. ....	17
Figure 2. 6: FEM solution of the 2D point source problem defined in Eq. 2.33. ..	1717
Figure 3. 1: Experimental observation of a photonic nanojet viewed along the optical axis of a $5 \mu m$ -diameter dielectric sphere made of glass, [45]......	20
Figure 3. 2: Visualization of a photonic nanojet of a plane-wave-illuminated circular dielectric cylinder of $5 \mu m$ diameter and has a refractive index of 1.7. [49]. .....	21
Figure 3. 3: Definition of the computational domain composed of a dielectric cylinder ( $\Omega_C$ ) embedded in the free space ( $\Omega_{FS}$ ) and truncated by PML. ....	22
Figure 3. 4: A possible discretization of the computational domain at $R = 1.5\lambda$ , and $N \times N = 9 \times 9$ for each element (here, only elements corresponding to $\Omega_{FS}$ and $\Omega_C$ are shown). ....	23
Figure 3. 5: Visualization of photonic nanojet at $R = 3.5\lambda$ and $n = 1.6$ .....	24
Figure 3. 6: 3D visualization of photonic nanojet at $R = 3.5\lambda$ and $n = 1.6$ .....	24
Figure 3. 7: Visualization of photonic nanojet at $R = 5\lambda$ and $n = 1.6$ .....	25
Figure 3. 8: Visualization of photonic nanojet at $R = 6.5\lambda$ and $n = 1.4$ .....	25
Figure 3. 9: Color mapping of field intensity as obtained by FDTD method for various shapes of dielectric micro-cylinders. ....	27
Figure 3. 10: Visualization of the evolution of a photonic nanojet for $R = 3.50\lambda$ and $n = 1.7$ . WGM representation gives $m=28$ and $I = 2$ .....	28
Figure 3. 11: Visualization of the evolution of a photonic nanojet for $R = 4.50\lambda$ ....	29
Figure 3. 12: FDTD visualization of the evolution of a photonic nanojet for. ....	29
Figure 3. 13: Magnitude of magnetic scattered-incident field inside the cylinder for $R = 4\lambda$ and $n = 1.4$ .as obtained by Mie theory.....	31
Figure 3. 14: The magnitude of the total magnetic field inside the cylinder .....	32
Figure 3. 15: The magnitude of the total magnetic field inside the cylinder at .....	32
Figure 4. 1: Total field absolute value inside and outside of the dielectric cylinder of radius $R = 3.5\lambda$ due to an illuminating plane wave as computed by SEM in	

	the neighborhood of resonance at (a) $n=1.6995$ , (b) $n=1.7000$ (maximum), (c) $n=1.7005$ , and (d) $n=1.7010$ .....	37
Figure 4. 2:	(a) Total field absolute value inside and outside of the dielectric cylinder of radius $R=3.5\lambda$ due to an illuminating plane wave as computed by SEM in the neighborhood of resonance at (a) $n=1.6$ , (b) $n=1.8$ . .....	38
Figure 4. 3:	Total field magnitude inside and outside of the dielectric cylinder of refractive index $n=1.7$ due to an illuminating plane wave as computed by SEM in the neighbourhood of resonance at (a) $R=3.5005$ , (b) $R=3.5010$ , respectively. ....	38
Figure 4. 4:	Magnitude of the electric field profile along the x-axis passing through the micro-cylinder's center. Data presented in figure 4.1 is used to plot the transverse field variations for four cases: (a): $n=1.6995$ , (b) $n=1.7000$ (on-resonance), (c) $n=1.7005$ , and (d) $n=1.7010$ .....	38
Figure 4. 5:	Magnitude of the total field inside and outside of the dielectric cylinder of radius $R=4.5\lambda$ due to an illuminating plane wave as computed by SEM in the neighbourhood of resonance at (a) $n=1.9995$ , (b) $n=2.0000$ (maximum), (c) $n=2.0005$ , and (d) $n=2.0010$ .....	39
Figure 4. 6:	Field magnitude inside the dielectric cylinder of radius $R=3.5\lambda$ due to an illuminating plane wave as calculated by Mie theory in the neighbourhood of resonance at (a1) $n=1.6795$ , (b1) $n=1.6800$ , (c1) $n=1.6805$ (maximum). The contributions of the mode $m=27$ to the overall intensity are shown in (a2), (b2) and (c2) at $n=1.6795, 1.6800, \text{ and } 1.6805$ , respectively.....	40
Figure 4. 7:	Total field magnitude inside the dielectric cylinder of radius $R=4.5\lambda$ and at $n=1.97259$ due to an illuminating plane wave as calculated by Mie theory: (a) For $m:=0 \rightarrow 120$ , (b) The contribution of the mode number $m=36$ .....	41
Figure 4. 8:	Illumination by Bessel's beam at $\gamma=0.6$ (a) magnitude of the exciting incident field produced by Bessel's beam, and (b) magnitude of the total scattered-incident field (3D view) inside and outside the dielectric cylinder whose parameters are $R, n=3.5\lambda, 1.7$ .....	46
Figure 4. 9:	Magnitude of the total field inside and outside a dielectric cylinder of radius $R=2.8\lambda$ for (a) $n_1=1.5$ , and (b) $n_1=1.5, n_2=1.33$ .....	46
Figure 4. 10:	Magnitude of the total field inside and outside a dielectric cylinder of radius $R=3.5\lambda$ at $n_1=1.7$ , and has a square region of $n_2=1.33$ and $2.4\lambda \times 2.4\lambda$ at its center. ....	47
Figure 4. 11:	Magnitude of the total field along x-axis for the case in figure 4.8. ....	47
Figure 4. 12:	Magnitude of the total scattered-incident field due to plane wave illumination inside and outside the dielectric cylinders of radius and refractive index (a) $(R, n) = (3.5198\lambda, 1.69)$ , (b) $(R, n) = (3.2245\lambda, 1.85)$ , (c) $(R, n) = (2.847491\lambda, 2.1)$ and (d) $(R, n) = (2.7198007\lambda, 2.2)$ .....	49
Figure 4. 13:	Magnitude of the total field along the x-axis for the case in figure 4.8 50	
Figure 4. 14:	Radius versus refractive index variation for the same type of resonance mode with dielectric micro-cylinder. Data points captured with SEM are	



plotted with markers. Cubic spline extrapolation of the relation between the physical parameters defining the micro-cylinder where two-ring resonance takes place. ....	50
Figure 4. 15: Magnitude of the total field resulting from a plane-wave illuminated dielectric cylinder of (a) $R = 5.0\lambda$ , $n = 1.4$ , and (b) $R = 4.5\lambda$ , $n = 1.905$ . ....	52
Figure 4. 16: Schematic representation of the photonic structure illuminated by a point source. ....	53
Figure 4. 17: Real part of the electric field generated by a point source. ....	53
Figure 4. 18: Illumination by a point source placed at different positions for $R, n = 3\lambda, 1.5$ (a) $d = 15\lambda$ , (b) $d = 10\lambda$ , (c) $d = 5\lambda$ , (d) $d = 3\lambda$ . ....	54
Figure 4. 19: Illumination by a point source placed at different positions for $R = 3.06267\lambda$ , $n = 1.95$ (a) $d = 10\lambda$ , (b) $d = 5\lambda$ , the associated field magnitudes along x-axis are shown in (c) and (d), respectively. ....	55
Figure 5. 1: The schematic of the hemicylindrical particle and definition of forward and backward excitation. ....	60
Figure 5. 2: The magnitude of the total scattered field due to plane wave illumination (backward excitation) inside and outside the hemicylinder with the radius and the refractive index values (a) $(R, n) = (3.5\lambda, 1.7)$ , (b) $(R, n) = (2.93\lambda, 2.0)$ . ....	61
Figure 5. 3: The magnitude of the total scattered-incident field due to plane wave illumination (back excitation) along the line of symmetry for $R = 2.93\lambda$ and different refractive indices. ....	62
Figure 5. 4: The magnitude of the total scattered field for forward plane wave illumination of the hemicylinder with the radius and refractive index of (a) $(R, n) = (1.5\lambda, 1.65)$ , (b) $(R, n) = (1.5\lambda, 1.55)$ , (c) $(R, n) = (2.93\lambda, 2.0)$ , and (d) $(R, n) = (2.96\lambda, 2.0)$ . ....	62
Figure 5. 5: The magnitude of the total scattered field in the case of forward excitation along the line of symmetry while setting $n = 2.0$ and $R = \{2.93\lambda, 2.96\lambda\}$ . ....	63
Figure 5. 6: The magnitude of the total scattered field for forward plane wave illumination of the hemicylinder with the radius and refractive index of $(R, n) = (2.96\lambda, 1.46)$ . ....	64
Figure 5. 7: The GLL grids ( $N \times N = 9 \times 9$ ) in the 12 elements for a regular cylinder (a) of radius $R_0 = 4\lambda$ , and (b) for a corrugated cylinder of $R_0 = 4\lambda$ , $m_1 = 6$ , $m_2 = 4$ , and $\beta = 0.3$ . ....	65
Figure 5. 8: The dielectric corrugated cylinder of average radius $R_0 = 4.5\lambda$ plotted at (a) $m_1 = 10$ , $m_2 = 2$ , and $\beta = 0.2$ , (b) $m_1 = 10$ , $m_2 = 2$ , and $\beta = 0.4$ , (c) $m_1 = 10$ , $m_2 = 4$ , and $\beta = 0.2$ , and (d) $m_1 = 10$ , $m_2 = 4$ , and $\beta = 0.4$ . Perfect cylinders with $R_0 = 4.5\lambda$ are superimposed in each case for easy inspection of the irregular boundaries with respect to ideal case. ....	67
Figure 5. 9: Field magnitude inside and outside the dielectric corrugated cylinder of refractive index $n = 1.5$ and average radius $R_0 = 4.5\lambda$ due to a normally	

incident plane-wave as computed by SEM for the four cases shown in Figure 5.8. ....	68
Figure 5. 10: Field magnitude inside and outside the dielectric corrugated cylinder of refractive index $n = 1.7$ and average radius $R_0 = 2.5\lambda$ due to a normally incident plane-wave as computed by SEM for (a) a circular cylinder, (b) $m_1 = 10, m_2 = 2$ , and $\beta = 0.111$ , (c) $m_1 = 10, m_2 = 2$ , and $\beta = 0.222$ , (d) $m_1 = 10, m_2 = 4$ , and $\beta = 0.111$ , and (e) $m_1 = 10, m_2 = 4$ , and $\beta = 0.222$ . ....	69
Figure 5. 11: The dielectric corrugated cylinder of average radius $R_0 = 2.5\lambda$ (a) plotted at $m_1 = 16, m_2 = 4$ , and $\beta = 0.18$ , and (b) the SEM solution ( $ E_z $ ) at $n = 1.452$ due to a normally incident plane-wave propagating in positive x direction. ....	71
Figure 5. 12: Field magnitude inside and outside the dielectric corrugated cylinder of average radius $R_0 = 2.5\lambda$ , $m_1 = 16, m_2 = 4$ due to a normally incident plane-wave as computed by SEM for (a) $n = 1.452, \beta = 0.12$ , (b) $n = 1.452, \beta = 0.18$ , (c) $n = 1.452, \beta = 0.22$ , and (d) $n = 1.455, \beta = 0.18$ . ....	71
Figure 5. 13: SEM solution to the incident-scattered field ( $E_z^{inc} + E_z^s$ ) inside and outside of a magnetodielectric cylinder of radius $R = 3\lambda$ and with $\epsilon_r = \mu_r = 1.5$ .....	73
Figure 5. 14: SEM solution to the real of incident-scattered field ( $E_z^{inc} + E_z^s$ ) inside and outside of a magnetodielectric cylinder of radius $R = 3\lambda$ and with $\mu_r = 3$ and $\epsilon_r = (4 - \mu_r) / (2\mu_r + 1)$ . ....	74
Figure 5. 15: $ E_z^{inc} + E_z^s $ inside and outside of a magneto-dielectric cylinder of radius $R = 3\lambda$ and with $\mu_r = 3$ and $\epsilon_r = (4 - \mu_r) / (2\mu_r + 1)$ . ....	74
Figure 5. 16: Magnitudes of total fields ( $ E_z^{inc} + E_z^s $ ) for a micro-cylinder of radius $R = 3\lambda$ , (a) $\epsilon_r = 2, \mu_r = 1$ , (b) $\epsilon_r = 2, \mu_r = 0.5$ , (c) $\epsilon_r = 0.5, \mu_r = 2$ (c) field magnitudes along propagation direction, i.e., along $y = 0$ , for the cases in part (a) and (b). Dimensions are normalized with $\lambda$ . ....	75
Figure 5. 17: $ E_z^{inc} + E_z^s $ inside and outside of a magnetodielectric square cylinder with $3\lambda \times 3\lambda$ and whose $\mu_r = 1.4$ and $\epsilon_r = 1/1.4$ . ....	76

## LIST OF TABLES

**Sayfa**

Table 2. 1: Maximum relative errors of FDM and SEM for the problem defined in Eq. 2.30. ....	15
Table 2. 2: Maximum errors of SEM and FEM for the problem defined in Eq. 2.32. ....	17
Table 2. 3: Maximum relative errors of FEM and SEM for the problem defined in Eq. 2.33. ....	18
Table 4. 1: $(R, n)$ pairs at which 2-ring resonance appears .....	49
Table 5. 1: Variations of radius in terms of incident wavelength .....	66
Table 5. 2: Variations of radius in terms of incident wavelength .....	67



## ABBREVIATIONS

1D	: One Dimension
2D	: Two Dimension
ABC	: Absorbing Boundary Condition
BC	: Boundary Condition
CPU	: Central Processing Unit
FEM	: Finite Element Method
FDM	: Finite Difference Method
FDTD	: Finite Difference Time Domain
FWHM	: Full Width at Half Maximum
GLL	: Gauss-Legendre-Lobatto
PDE	: Partial Differential Equation
PML	: Perfectly Matched Layer
PNJ	: Photonic Nano Jet
SEM	: Spectral Element Method
TE	: Transverse Electric
TM	: Transverse Magnetic
WGM	: Whispering Gallery Mode



## LIST OF SYMBOLS

$k$	: One Dimension
$\lambda$	: Wavelength
$\theta$	: Angle of incidence
$E$	: Electric field
$E^{inc}$	: Incident electric field
$E^{sc}$	: Scattered electric field
$\Omega^e$	: Deformed element
$\Omega^{st}$	: Standard element
$\alpha$	: Attenuation factor
$\mu$	: Magnetic permeability
$\mu_r$	: Relative permeability
$\varepsilon$	: Permittivity
$\varepsilon_r$	: Relative permittivity
$R$	: Radius
$n$	: Refractive index
$\partial$	: Partial derivative





## 1. INTRODUCTION

*“Read in the name of your Lord. Who created. Created man from a clot of congealed blood. Read, and your Lord is Most Generous. Who taught knowledge by the pen, taught man what he did not know”*

*—Al Alaq, The QURAN*

Human beings should acknowledge and not forget the Scottish physicist and mathematician James Clerk Maxwell (1831-1879), who combined these laws into a set of partial differential equations, known as Maxwell’s equations. Maxwell didn’t only simplify and reformulate these laws, but also he added another term to the differential equation corresponding to Ampere’s circuital law. This addition was the historical step that brought humanity to the technology that we enjoy nowadays. It was the prediction of existence of electromagnetic waves.

Well, progress and improvements in science occur successively, exactly as climbing a building by a ladder. Maxwell’s work wouldn’t appear at all if for instance, but not limited to, Charles Austin de Coulomb (1736-1806), Luigi Galvani (1737-1790), Hans Christian Oersted (1777-1851), Andre Marie Ampere (1775-1836), and Michael Faraday (1791-1867) didn’t form the previous steps in that ladder. In fact, the same level of acknowledgment should be given to these scientists and all others who lived before and after. As a student, and here I confirm that I don’t interpret being a student the one who seeks a certificate but rather who seeks the knowledge, I acknowledge all people who contributed to science starting from the first man who thought about optics and ending with my advisor.

### 1.1 Brief History About Transparent Spheres

Over the last 400 years, scientists have been attracted by transparent spherical particles. In fact, since ancient times, it has been known that a garden shouldn’t be watered during the afternoon because water droplets may cause sunburn to the leaves. Pliny Elder (AD 23-79) reported on the incendiary action of spheres made of glass and

such spheres when one looks at small letters through it. Ptolemy, Archimedes and most physicists knew about light refraction. Establishing the complete law of refraction, however, was not easy. Investigating the historical analysis [1], one can find that this law in its correct form was firstly established by Ibn Sahl at Baghdad's court in 984, then later was rediscovered by Thomas Harriot in 1602, Johannes Kepler in 1604, Willebrord Snellius in 1621 and Rene Descartes in 1637.

Kepler introduced the definition of focus and tried to explain the principles of pinhole cameras. He mainly described refraction of light and the concept of optical images. He then established the theory of lenses. Almost at the same time, Galileo wrote in his letter to Giovanni Trade (1614): "This science is still not well known, and I do not know anyone who would be engaged in it, unless the recall of Johannes Kepler, the Imperial mathematician who wrote a book about it, but it is so dark that it is perhaps no one understood". This forms a clue to the fact that photonic nanojets were not known. Kepler was also familiar with a question debated by ancient scientists: "Whether a million of Angels may not fit upon a needle's point?" Can one ask the same question about the pieces of light at the nanoscale?

A major step forward to light scattering by small particles was taken by Lord Rayleigh. From his point of view [2], it follows that small dielectric particles of size much less than the incident wavelength do not act as small lens but scatter light as point electric dipoles. Thus an asymmetrical jet-like field arises just in the some range of the normalized size in terms of the wavelength. Later on, in 1908, Mie theory [3] was established to provide the full description of light scattering by spherical particles.

## **1.2 What Is A Photonic Nanojet?**

The majority of the studies devoted to photonic nanojet structures has been done for single and chain of spheres [4-32] and cylinders [33-39]. When an electromagnetic plane wave is perpendicularly incident to a dielectric cylinder or to a dielectric sphere, instead of having a shadow region behind the dielectric material, a photonic nanojet is obtained at some specific choices of material dimensions and a corresponding refractive index. Photonic nanojets can be defined as a narrow electromagnetic beam having high intensity. This beam propagates into the background medium, in which the dielectric material is embedded [40]. In order to

obtain a photonic nanojet, the dielectric microspheres or micro cylinders must be lossless dielectric materials and of diameters greater than the illuminating wavelength. Due to the unique nature of the light distribution at the focal area, the phenomenon is named as photonic nanojet [4-44].

The key properties defining the photonic nanojet are [40]:

1. It is non-evanescent beam that propagate while maintaining a subwavelength full-width at half-maximum (FWHM) transverse beam width along a specific path that can extend more than twice of the wavelength behind the dielectric micro cylinder or microsphere.
2. Its minimum FWHM beam width can be as small as around one-third of the wavelength for microspheres, in another word; FWHM can be smaller than the classical diffraction limit.
3. It is a phenomenon that has a nanoresonant property. That is, it can appear for a wide range of the diameter of the microsphere or micro cylinder extending from 2 to 40 times the wavelength for a very applicable, relative refractive index (i.e., less than 2).
4. Photonic nanojets have a very high intensity which exceeds the intensity of the illuminating wave.

Photonic nanojets have several applications. They are mainly utilized in the following applications [40], [45-46]:

- Nanospectroscopy (detection and manipulation of nanoscale objects),
- Subdiffraction resolution,
- Enhanced Raman scattering,
- Waveguiding, and,
- High intensity optical storage.

Low-loss optical wave guiding, high density data storage, lithography, high resolution microscopy, and nonlinear optical effects are the other applications of photonic nanojets [47-49].

### **1.3 Solving Maxwell's Equations**

Engineers and scientists use several approaches in analysing electromagnetic phenomena that are governed by Maxwell's equations. These approaches can be mainly classified as experimental, analytical, or numerical. Being hazardous

sometimes, expensive or time consuming, experimental techniques are not preferable. The latter two approaches, on the other hand, are convenient to use in electromagnetic modelling.

Analytical methods are mainly separation of variables, series expansion, conformal mapping, integral solutions (as Laplace and Fourier transforms), and perturbation methods. The connection between analytical methods and numerical methods is very strong from the sense that numerical methods involve analytic simplification to the point where it is easy to apply a specific numerical method. However, in general, obtaining the analytical solution is very difficult. This difficulty in analytical methods leaves the numerical methods as the only convenient methods for engineers. Numerical methods are inter-related to each other and they give an approximate solution with a sufficient accuracy for engineering purposes. The most common numerical methods in electromagnetic modelling are [50]:

- a. Finite difference method
- b. Method of weighted residuals
- c. Method of moments
- d. Finite element method
- e. Transmission-line modelling
- f. Monte Carlo method
- g. Method of lines

The necessity for the application of numerical methods is best expressed by Paris and Hurd: “Most problems that can be solved formally (analytically) have been solved” [51]. In fact, until 1940s, most of electromagnetic problems that involve simplicity were solved by analytical methods, mainly by separation of variables and integral equation methods. In addition, a lot of effort was given to extend the application of these methods to a narrow range of practical problems. However, complexity in geometries associated with the most realistic problems was the main reason behind developing numerical methods that can be easily performed by computing machines. In parallel to the development of high-speed digital computers during 1960s, numerical solutions of electromagnetic problems attracted the attention of electrical engineers [50]. This is due to the fact that the computers can numerically solve very complex and realistic problems, whose analytical solutions are impossible to find. Moreover, the numerical approach allows the actual work to be performed without requiring the operator to be of high level in mathematics or physics.

Another classification of electromagnetic problems is based on the domain in which the solution is sought; that is, frequency domain and time domain. For each domain, modelling differential equations or integral equations can be utilized. Throughout this thesis, differential equations in frequency domain are used.

Spectral element method (SEM) has been recently applied to electromagnetic problems [53-58] and attracted the attention of computational electromagnetic community. The attraction of this method is mainly due to the accuracy achieved for much less degrees of freedom.

#### **1.4 Contribution Of The Thesis**

This thesis is based on the following publications that cover most of the contributions:

1. I. Mahariq, H. Kurt, H. I. Tarman, and M. Kuzuoğlu, “Photonic Nanojet Analysis by Spectral Element Method”, *IEEE Photonics Journal*, 6(5), pp. 1-14, 2014.
2. I. Mahariq, and H. Kurt, “On- and off-optical-resonance dynamics of dielectric microcylinders under plane wave illumination”, *Journal of the Optical Society of America B*, Vol. 32.6, pp. 1022-1030, 2015.
3. I. Mahariq, V. Astratov, and H. Kurt, “Persistence of photonic nanojet formation under the deformation of circular boundary”, *Journal of the Optical Society of America B*, 33.4: 535-542, 2016.
4. I. Mahariq, and H. Kurt, “Strong field enhancement of resonance modes in dielectric micro-cylinders”, *Journal of the Optical Society of America B*, 33.4: 656-662, 2016.
5. I. Mahariq, H. Kurt, and M. Kuzuoğlu, “Questioning Degree of Accuracy Offered by the Spectral Element Method in Computational Electromagnetics”, *Applied Computational Electromagnetics Society Journal*, vol. 22.7, 2015.
6. I. Mahariq, N. Eti, and H. Kurt, “Engineering Photonic Nano-jet Generation”, *Computational Electromagnetics International Workshop*, July 4-6, 2015. Izmir, Turkey.
7. N. Eti, I. Mahariq, and H. Kurt, “Mode Analysis and Light Confinement of Optical Rib Waveguides in Various Air Slot Configurations”, *17th International Conference on Transparent Optical Networks*, July 5-9, 2015, Budapest, Hungary.

The following manuscripts are currently under review:

1. I. Mahariq and H. Kurt, “Investigation of Strong Field Enhancement Resulting from Magnetodielectric Cylinders”, IEEE Photonics Technology Letters.
2. I. Mahariq, I. H. Giden, I. V. Minin, O. V. Minin, and H. Kurt “Strong electromagnetic field localization near the surface of hemicylindrical particles”, Optical and Quantum Electronics.

### **1.5 Outline Of The Thesis**

In chapter 1, an introduction is presented including some history about transparent spheres. Also, a brief summary of the numerical methods applied for solving Maxwell’s equations.

Then, the formulation of the spectral element method required to solve Maxwell’s equations governing the photonic structures is presented in chapter 2. In addition, the deterioration of spectral element method resulting from the elemental deformation is discussed. The chapter ends by a quick comparison between spectral element method, finite element method and finite difference method in terms of accuracy in both one and two dimensional problems.

Chapter 3 discusses the properties and analysis of photonic nanojets and whispering gallery modes resulting from a plane-wave excited micro-cylinders. In chapter 4, a detailed discussion about the dependency whispering gallery modes on the physical parameters of cylinders is included. The corresponding spectral element solutions is then compared with Mie theory solutions. Numerical tracking to the physical parameters combinations is also presented. The chapter also investigates the behaviour of photonic jets and whispering gallery modes under different excitation schemes.

Chapter 5 presents the analysis about the deformation of cylinders and how it affects the photonic nanojet characteristics and whispering gallery modes. The same chapter discusses the field analysis when magnetic cylinders are considered. Chapter 6 finished the thesis presentation by some conclusions.

## **2. SPECTRAL ELEMENT FORMULATION OF ELECTROMAGNETIC SCATTERING**

In this chapter, the discrete formulation of electromagnetic scattering problems to spectral element method is presented. Subsequently, the accuracy of the spectral element method is compared with that obtained by the finite element method and finite difference method.

### **2.1 Introduction**

Spectral element method was first introduced by Patera [66] in 1984 for computational fluid dynamics. Patera proposed a spectral element method that combines the flexibility of the finite element method with the accuracy of spectral methods (the case where p-type method is applied for a single-element domain). In the spectral element method, he utilized high-order Lagrangian polynomial interpolant over Chebyshev collocation points in order to represent the velocity in each element in the computational domain.

Generally speaking, spectral element methods are considered as a family of approximation schemes based on the Galerkin method. They share common characteristics with finite-element discretizations, and this provides the reason why they can be viewed as h- or p-versions of finite element method. That is, when viewed as h-version, a Lagrangian interpolation formula on the parent element exists in both, as well as the basis functions have local support. On the other hand, spectral element methods use high-degree polynomials on a fixed geometric mesh for sake of enhanced accuracy, and this is the fact characterizing the p-version of finite element methods [67].

Orthogonality of basis functions either in the h- or p-versions of the finite element is due to non-overlapping local functions. However, in spectral element methods orthogonality is related to both analytical nature and topological nature (local extension) of the basis functions. This fact tells us why spectral element method is different from finite element method of h-version or p-version [68].

There are mainly two implementations that have been proposed, one based on Chebyshev polynomials [66], and the other based on Legendre polynomials. In both cases, Gauss-Lobatto quadrature grid is utilized to perform Lagrangian interpolation. This implementation ensures the continuity of the solution and benefit from the associated numerical quadrature schemes. Patera [66] chose Chebyshev polynomials basically because of the possibility of using fast transform techniques. On the other side, the stiffness and mass matrices were evaluated by the quadratures that were performed analytically without utilizing the weighting factor associated with Chebyshev polynomials [67], (the weighting factor is  $(\sqrt{1-x^2})^{-1}$ , by which Chebyshev polynomials are orthogonal in contrast to Legendre polynomials whose orthogonality comes with unity weighting factor).

Before we proceed with spectral element formulation, it is important to summarize the set of partial differential equations (PDEs) that governs an electromagnetic scattering problem.

## 2.2 The Governing PDEs

In a typical electromagnetic scattering and/or radiation problem, there are a set of partial differential equations to be solved together with the equations governing the perfectly matched layer (PML) region that is utilized for domain truncation. Here, we summarize all of these equations in order to provide a complete set to be formulated by the spectral element method.

The computational domain is composed of several subdomains that are associated with the following set of partial differential equations in which  $\mathbf{u} = E_z^s(x, y)$  denotes the scattered electrical field polarized in z-axis [69]:

$$\frac{\partial^2 \mathbf{u}}{\partial x^2} + \frac{\partial^2 \mathbf{u}}{\partial y^2} + k^2 \mathbf{u} = 0, \quad (2.1)$$

is satisfied over the free-space region,

$$\frac{1}{a} \frac{\partial^2 \mathbf{u}}{\partial x^2} + a \frac{\partial^2 \mathbf{u}}{\partial y^2} + a k^2 \mathbf{u} = 0, \quad (2.2)$$

governs the field attenuated in x-direction in PML region,

$$a \frac{\partial^2 \mathbf{u}}{\partial x^2} + \frac{1}{a} \frac{\partial^2 \mathbf{u}}{\partial y^2} + a k^2 \mathbf{u} = 0, \quad (2.3)$$



governs the field attenuated in y-direction in PML region,

$$\frac{1}{a} \frac{\partial^2 \mathbf{u}}{\partial x^2} + \frac{1}{a} \frac{\partial^2 \mathbf{u}}{\partial y^2} + a k^2 \mathbf{u} = 0, \quad (2.4)$$

governs the field attenuated in both x- and y- directions in PML region, and

$$\nabla \cdot \left( \frac{1}{\mu_r} \nabla \mathbf{u} \right) + k^2 \varepsilon_r \mathbf{u} = k^2 (1 - \varepsilon_r) E_z^{inc}, \quad (2.5)$$

is satisfied wherever there is a dielectric object, where;  $k = 2\pi / \lambda$  is the wave number, with  $\lambda$  being the wavelength,  $a = 1 + \alpha / jk$ ,  $\alpha$  is the attenuation factor (a real number that defines amount of attenuation),  $\varepsilon_r$  is the relative permittivity of the scatterer,  $\mu_r$  is the relative permeability of the scatterer, and  $E_z^{inc}$  is the incident wave.

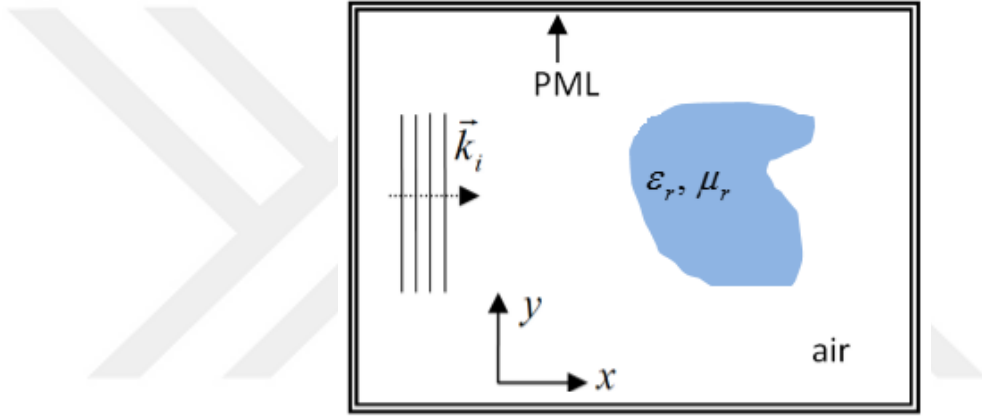


Figure 2. 1: A typical electromagnetic scattering problem composed of a dielectric (or magnetic) scatterer embedded in a free-space region, and domain truncation is performed by the perfectly matched layer.

Figure 2.1 shows a typical electromagnetic scattering domain which is composed of a scatterer of an arbitrary shape. The scatterer is embedded in a free-space region, and the domain truncation is performed by the perfectly matched layer. At this point, a tensor  $\Lambda$  is introduced so that all of the previous equations can be represented in one equation. The tensor is defined as:

$$\Lambda = \begin{bmatrix} \Lambda_{11} & 0 \\ 0 & \Lambda_{22} \end{bmatrix}, \quad (2.6)$$

where;  $[\Lambda_{11} \quad \Lambda_{22}] = \begin{bmatrix} 1 & \\ a & \end{bmatrix}$  for x-decay in the PML region,

$[\Lambda_{11} \quad \Lambda_{22}] = \begin{bmatrix} 1 \\ a \end{bmatrix}$  for y-decay in the PML region,

$$[\Lambda_{11} \quad \Lambda_{22}] = \begin{bmatrix} 1 & 1 \\ a & a \end{bmatrix} \text{ for a corner (xy-decay) in the PML region with } a = 1$$

in free-space region, and  $\varepsilon_r$  being greater than 1 in the scatterer only, and 1 elsewhere. Thus, the set of all partial differential equations governing an electromagnetic scattering problem can be written as follows:

$$\nabla \cdot \Lambda \nabla u + a \varepsilon_r k^2 u = k^2 (1 - \varepsilon_r) E_z^{inc}. \quad (2.7)$$

It is worth to mention that for transparent dielectric material and for free-space is  $\mu_r = 1$ . In addition,  $\varepsilon_r > 1$  in the dielectric material only, and  $\varepsilon_r = 1$  elsewhere. In fact, when  $\varepsilon_r = 1$ , the right-hand side of equation (2.7) vanishes to zero. In the next section, we provide the spectral element formulation for the Helmholtz equation as expressed in equation (2.7) which must be satisfied in a typical electromagnetic scattering and/or radiation problem.

### 2.3 SEM Formulation

As discussed in the previous section, a typical electromagnetic scattering and/or radiation problem in the frequency-domain can be defined as:

$$\nabla \cdot \Lambda \nabla u + a \varepsilon_r k^2 u = k^2 (1 - \varepsilon_r) E_z^{inc} \quad (2.8a)$$

for  $\mathbf{x} = (x, y) \in \Omega \subset \mathbb{R}^2$  subject to the boundary conditions:

$$u|_{\partial\Omega_D} = f, \quad \frac{\partial}{\partial n} u|_{\partial\Omega_N} = g, \quad (2.8b)$$

on the boundary  $\partial\Omega = \partial\Omega_D \cup \partial\Omega_N$ .

SEM formulation involves two function spaces, namely, test and trial spaces. An approximate solution to equation (2.8) is sought in the trial space

$$U = \left\{ u \in H \mid u|_{\partial\Omega_D} = f, \quad \frac{\partial}{\partial n} u|_{\partial\Omega_N} = g \right\}. \quad (2.9)$$

The residual resulting from the substitution of the approximate solution from the trial space into equation (3.8) vanishes in the process of projection onto the test space

$$V = \{ v \in H \mid v|_{\partial\Omega_D} = 0 \}. \quad (2.10)$$

The projection is performed by using the weighted inner product operation:

$$(v, u)_\omega \equiv \int_{\Omega} \omega \bar{v} u \, d\mathbf{x} \quad (2.11)$$

in the Hilbert space  $H$  where overbar denotes complex conjugation. The projection procedure

$$(\mathbf{v}, \nabla \cdot \Lambda \nabla \mathbf{u} + a \varepsilon_r k^2 \mathbf{u} - k^2 (1 - \varepsilon_r) E_z^{inc})_\omega = 0 \quad (2.12)$$

leads to the variational (weak) form

$$\int_{\Omega} \nabla (\omega \bar{\mathbf{v}}) \cdot \Lambda \nabla \mathbf{u} \, d\mathbf{x} - a k^2 \int_{\Omega} \omega \bar{\mathbf{v}} \mathbf{u} \, d\mathbf{x} = \int_{\partial\Omega_N} \omega \bar{\mathbf{v}} \mathbf{g} \, d\mathbf{x} - k^2 (1 - \varepsilon_r) \int_{\Omega} \omega \bar{\mathbf{v}} E_z^{inc} \, d\mathbf{x} \quad (2.13)$$

after integration by parts that introduces the boundary integrals. The trial function is then decomposed as follows

$$\mathbf{u} = \mathbf{u}_h + \mathbf{u}_b, \text{ where } \mathbf{u}_h|_{\partial\Omega_D} = 0 \quad \text{and} \quad \mathbf{u}_b|_{\partial\Omega_D} = \mathbf{f}, \quad (2.14)$$

resulting in

$$\begin{aligned} \int_{\Omega} \nabla (\omega \bar{\mathbf{v}}) \cdot \Lambda \nabla \mathbf{u}_h \, d\mathbf{x} - a k^2 \int_{\Omega} \omega \bar{\mathbf{v}} \mathbf{u}_h \, d\mathbf{x} &= - \int_{\Omega} \nabla (\omega \bar{\mathbf{v}}) \cdot \Lambda \nabla \mathbf{u}_b \, d\mathbf{x} + \\ &+ a k^2 \int_{\Omega} \omega \bar{\mathbf{v}} \mathbf{u}_b \, d\mathbf{x} - \int_{\partial\Omega_N} \omega \bar{\mathbf{v}} \mathbf{g} \, d\mathbf{x} - k^2 (1 - \varepsilon_r) \int_{\Omega} \omega \bar{\mathbf{v}} E_z^{inc} \, d\mathbf{x} \end{aligned} \quad (2.15)$$

after substitution into equation (2.13). The boundary conditions are now in place in the variational form with the introduction of the particular solution  $\mathbf{u}_b$  satisfying the nonhomogeneous Dirichlet boundary condition.

Adapting the formulation to an arbitrary domain geometry is achieved in two steps. The first step involves partitioning of the domain into mutually disjoint elements:

$$\Omega = \Omega^1 \cup \dots \cup \Omega^e \dots \cup \Omega^M = \bigcup_{e=1}^M \Omega^e. \quad (2.16)$$

A typical integral in the variational form then becomes

$$\int_{\Omega} \omega \bar{\mathbf{v}} \mathbf{u}_h \, d\mathbf{x} = \sum_{e=1}^M \int_{\Omega^e} \omega \bar{\mathbf{v}} \mathbf{u}_h \, d\mathbf{x}, \quad (2.17)$$

due to the linearity of integration operation. The second step is the introduction of the standard square element

$$\Omega^{st} = \{(\xi, \eta) \in \mathfrak{R}^2 \mid -1 \leq \xi \leq 1, -1 \leq \eta \leq 1\} \quad (2.18)$$

that will standardize and facilitate the integral operations over a general quadrilateral element  $\Omega^e$  with curved sides through mapping:

$$\mathbf{x} = \chi_1^e(\xi, \eta), \quad \mathbf{y} = \chi_2^e(\xi, \eta). \quad (2.19)$$

In another word, in order to perform the operations of integration and differentiation in an element  $\Omega^e$  that may have an arbitrary shape and orientation as shown in Figure 2.2, the introduction of the one-to-one elemental mapping defined in equation (2.19) is necessary. In fact, this mapping is also onto, which in turn becomes isomorphic transformation. The isomorphism here tells us that inverse transformation exists.

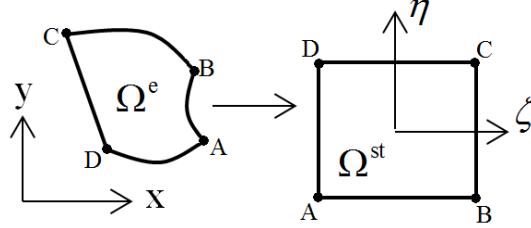


Figure 2. 2: Mapping an element  $\Omega^e$  to the standard element  $\Omega^{st}$ .

The differential operations can then be converted using the rules:

$$\begin{bmatrix} dx \\ dy \end{bmatrix} = \underbrace{\begin{bmatrix} \frac{\partial \chi_1^e}{\partial \xi} & \frac{\partial \chi_1^e}{\partial \eta} \\ \frac{\partial \chi_2^e}{\partial \xi} & \frac{\partial \chi_2^e}{\partial \eta} \end{bmatrix}}_{\mathbf{J}} \begin{bmatrix} d\xi \\ d\eta \end{bmatrix}, \quad \nabla = \begin{bmatrix} \frac{\partial}{\partial x} \\ \frac{\partial}{\partial y} \end{bmatrix} = \frac{1}{|\mathbf{J}|} \begin{bmatrix} \frac{\partial \chi_2^e}{\partial \eta} & -\frac{\partial \chi_1^e}{\partial \eta} \\ -\frac{\partial \chi_2^e}{\partial \xi} & \frac{\partial \chi_1^e}{\partial \xi} \end{bmatrix} \begin{bmatrix} \frac{\partial}{\partial \xi} \\ \frac{\partial}{\partial \eta} \end{bmatrix}, \quad (2.20)$$

where  $|\mathbf{J}|$  is the determinant of the Jacobian  $\mathbf{J}$ .

Numerical implementation of the procedure requires introduction of a spatial discretization that will facilitate the numerical evaluation of the derivatives and the integrals. This is equivalent to taking the trial and test spaces as finite dimensional spaces for which space of polynomials is the convenient choice. Jacobi polynomials as eigenfunctions of singular Sturm-Liouville differential operator provide a good basis for this space [70]. Numerically stable interpolation and highly accurate quadrature integration approximation techniques are provided by nodes and weights associated with Jacobi polynomials. In particular, Legendre polynomials are the convenient choice in that they are orthogonal under the weighted inner product with unity weight  $\omega = 1$ . The associated roots  $\zeta_m$  as nodes provide the stable form of interpolation

$$u(\zeta) = \sum_{m=0}^N u(\zeta_m) L_m(\zeta) \quad (2.21)$$

where  $L$  denotes respective Lagrange interpolants with the typical form

$$L_k(\zeta) = \prod_{\substack{\ell=0 \\ \ell \neq k}}^N \frac{(\zeta - \zeta_\ell)}{(\zeta_k - \zeta_\ell)} \quad (2.22)$$

satisfying the cardinality property  $L_k(\zeta_\ell) = \delta_{k\ell}$ . This in turn provides the means for evaluating the derivatives, say,

$$\left. \frac{d}{d\zeta} u(\zeta) \right|_{\zeta_k} = \sum_{m=0}^N u(\zeta_m) L'_m(\zeta_k) = \sum_{m=0}^N u(\zeta_m) \underbrace{L'_m(\zeta_k)}_{D_{km}} \quad (2.23)$$

where  $D_{km}$  is referred to as the differentiation matrix. It also provides Gauss-Legendre-Lobatto (GLL) quadrature

$$\int_{-1}^1 u(\zeta) d\zeta = \sum_{k=0}^N \varpi_k u(\zeta_k) \quad (2.24)$$

which is exact for the integrand of a polynomial of degree  $\leq 2N - 1$ . These can easily be extended to two dimensions over the tensor grid  $(\xi_k, \eta_\ell)$  with the mapping functions  $\chi_i(\xi, \eta)$  constructed using the linear blending function approach [71-72].

As mentioned above, the nodal basis for the reference element is usually built by Lagrangian basis polynomials associated with a tensor product grid of GLL nodes. Figure 2.3 shows such a grid for a ninth-order polynomial space. In one direction, the GLL grid nodes  $\zeta_\ell \in [-1, 1]$ ,  $0 \leq \ell \leq N$  are the roots of the polynomial:

$$(1 - x^2) \frac{dP_N(x)}{dx} \quad (2.25)$$

where  $P_N(x)$  is the Legendre polynomial of degree  $N$  in  $[-1, 1]$ :

$$\begin{aligned} P_0(x) &= 1, \\ P_1(x) &= x, \\ P_{n+1}(x) &= \frac{2n+1}{n+1} x P_n(x) - \frac{n}{n+1} P_{n-1}(x), \quad n \geq 1. \end{aligned} \quad (2.26)$$

The first six Legendre polynomials are plotted in Figure 2.4.

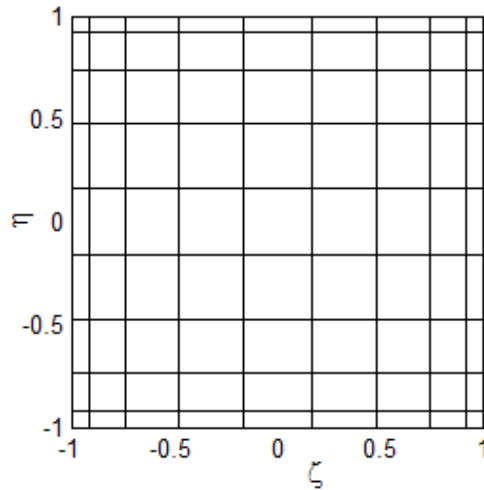


Figure 2. 3: GLL grid nodes on the reference element for a ninth-order polynomial space (nodes are represented by the intersections of horizontal and vertical lines).

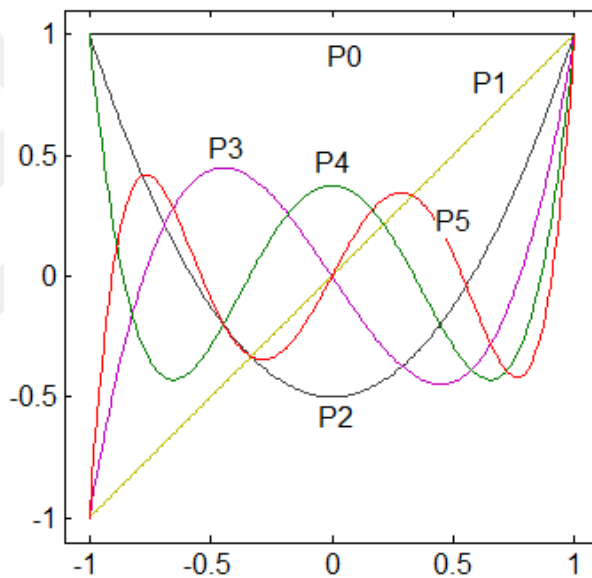


Figure 2. 4: Plot of first six Legendre polynomials.

It is important here to demonstrate the accuracy of the spectral element in one element of square shape and deformed shape. In the following section, the effect of element deformation on the accuracy of spectral element method is investigated.

#### 2.4 The Accuracy Of SEM, FDM And FEM

To get an insight about the accuracy gained from SEM, when compared to other numerical methods, demonstrations are performed using numerical examples. For this purpose, a comparison is first carried out between SEM and FDM with a stencil

composed of 3 nodes in one dimension. We considered the following one-dimensional boundary-value problem:

$$\frac{d^2 u}{dx^2} + k^2 u = 0, \text{ in the interval } [0, 1.1] \quad (2.30)$$

with  $u(0) = 1, u(1.1) = e^{-jk1.1}$

where  $k = 2\pi$ . We define an error measure as follows:

$$Err = \max_i \frac{|u_{i,exact} - u_{i,numerical}|}{|u_{i,exact}|} \quad (2.31)$$

where;  $u_{i,exact}$  is the exact solution (for this problem, it is  $e^{-jkx}$ ), and  $u_{i,numerical}$  is the numerical solution obtained by the specified numerical method at the  $i$ th node in the computational domain.

In Table 2.1, the maximum relative errors for both FDM and SEM are presented as the number of nodes (N) increases in both methods. Obviously, it can be observed that the errors of FDM are slowly decaying although the number of nodes is chosen in the order of 10. On the other hand, SEM shows high accuracy with much fewer number of nodes. That is, the accuracy obtained by FDM at 100 nodes can be achieved by 8 nodes with SEM.

Table 2. 1: Maximum relative errors of FDM and SEM for the problem defined in Eq. 2.30.

FDM		SEM	
N	Err	N	Err
10	0.1840	7	0.0103
20	0.0524	8	0.0012
30	0.0238	9	1.455e-04
40	0.0135	10	1.608e-05
50	0.0087	11	2.074e-06
60	0.0060	12	2.308e-07
70	0.0044	13	2.570e-08
80	0.0034	14	2.624e-09
90	0.0027	15	2.613e-10
100	0.0022	16	2.420e-11
110	0.0020	17	2.318e-12

To compare SEM with the first-order FEM, we consider the following 1D problem:

$$\begin{aligned} \frac{d^2 u}{dx^2} + u &= 0, \text{ in } [-1, 0], \text{ and} \\ \frac{d^2 u}{dx^2} + 4^2 u &= 0, \text{ in } [0, 1] \end{aligned} \quad (2.32)$$

with  $u(-1) = \sin(-1)$ ,  $u(1) = \sin(4)$ .

In fact the solution of (2.32) is  $u(x) = \sin(cx)$ , with  $c = 1$  in  $[-1, 0]$ , and  $c = 4$  in  $[0, 1]$ . However, for error calculations, to avoid division by zero, we compute the error (only for this problem) as the maximum difference between the exact solution and the numerical solution. The comparison is shown in Table 2.2 in which N represents the number nodes in each sub-domain. Again, it can be seen that SEM accuracy is much higher than that of FEM. Figure 2.5 shows the plot of the solution obtained by SEM for 15 nodes in each subdomain.

It is worth also to compare FEM and SEM in a two dimensional boundary value problem. For this purpose, the point source problem (2D Green's function) is considered. This problem is governed by the Helmholtz equation:

$$\nabla^2 u + k^2 u = -\delta(\vec{r}), \quad (2.33)$$

where  $k = 2\pi / \lambda$ , and  $\lambda$  is the wavelength. To avoid the singularity at the origin, the homogenous Helmholtz equation is solved inside a square element ( $\Omega$ ) of dimensions  $\lambda \times \lambda$  and  $\lambda = 1$ , and  $\Omega$  is defined in the xy-plane so that the point (0,0) does not belong to this element. On the boundary  $\partial\Omega$ , the exact solution to (2.33), which is expressed in terms of Hankel function of the second kind zero order as follows: ( $u(\vec{r}) = (j/4)H_0^{(2)}(k|\vec{r}|)$ ), is applied as boundary conditions, where  $|\vec{r}|$  is the euclidean distance from the origin to a point  $|\vec{r}|$  on the boundary  $\partial\Omega$ . Right-triangle elements are utilized in meshing the problem. Figure 2.6 shows the solution obtained by FEM at a grid of  $20 \times 20$  nodes. As observed from Table 2.3, the error profile in 2D does not differ from that of 1D case.



Table 2. 2: Maximum errors of SEM and FEM for the problem defined in Eq. 2.32.

FEM		SEM	
N	<i>Err</i>	N	<i>Err</i>
10	0.0546	7	7.033e-05
20	0.0252	8	3.340e-06
30	0.0164	9	4.697e-07
40	0.0121	10	1.876e-08
50	0.0096	11	2.593e-09
60	0.0080	12	9.092e-11
70	0.0068	13	1.132e-11
80	0.0059	14	3.481e-13
90	0.0053	15	3.941e-14
100	0.0047	16	1.587e-14

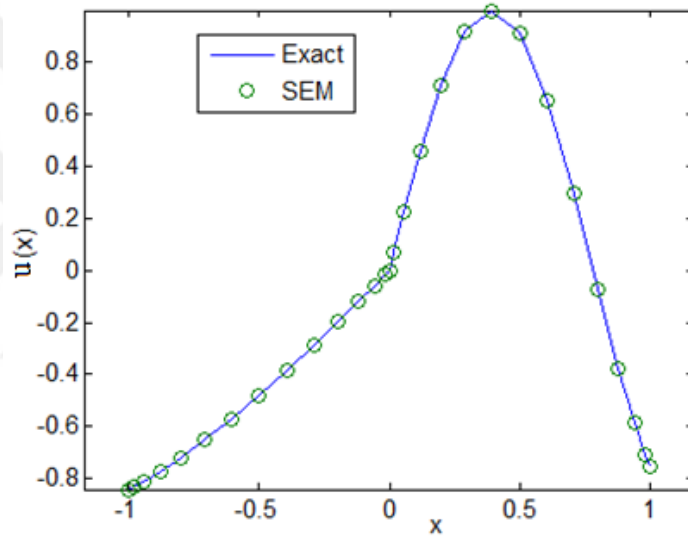


Figure 2. 5: Exact and SEM solutions of the problem defined in Eq. 2.32.

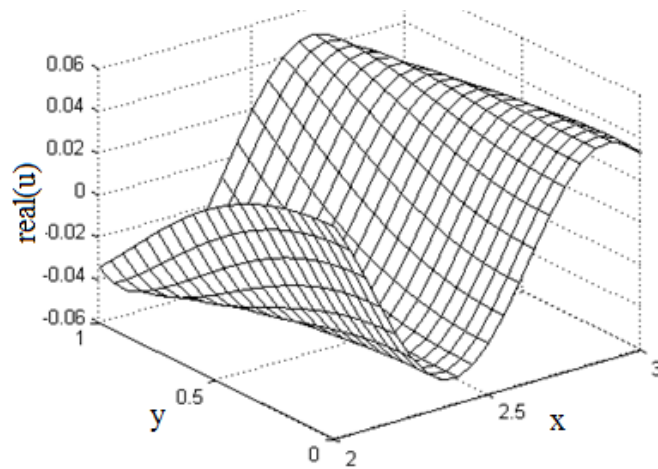


Figure 2. 6: FEM solution of the 2D point source problem defined in Eq. 2.33.

Table 2. 3: Maximum relative errors of FEM and SEM for the problem defined in Eq. 2.33.

FEM		SEM	
N	<i>Err</i>	N	<i>Err</i>
10	0.5554	7	0.00091
15	0.3229	8	1.30E-04
20	0.2018	9	1.25E-05
25	0.1356	10	1.14E-06
30	0.0967	11	1.13E-07
35	0.0724	12	1.26E-08
40	0.0562	13	1.51E-09
45	0.0447	14	2.23E-10
50	0.0364	15	2.57E-11
55	0.0302	16	3.23E-12
60	0.0255	17	2.86E-13
80	0.0145		
100	0.0103		

## 2.5 Conclusion

In this chapter, the formulation of electromagnetic scattering and radiation problems based on the spectral element method is provided. This formulation considers also domain truncation by the perfectly matched layer. For this purpose, all the partial differential equations that govern over the perfectly matched layer, free-space regions, magnetic and/or dielectric objects, are put in a single representative form that defines a typical electromagnetic scattering in frequency domain. Numerical implementation by spectral element method is then applied.

Next, the effect of element deformation on the accuracy of spectral element method is investigated. As observed from the results, in quadrilateral elements having straight or curved sides the error was less than that of rectangular elements. Thus, in general, the accuracy can deteriorate if the aspect ratio of some elements is chosen to be large. One can notice from the presented errors that there is no safe range of the aspect ratio in which high accuracy is guaranteed.

Finally, a comparison is made in terms of accuracy among SEM, FDM and FEM. As it can be clearly seen from the results, SEM dominates the other numerical methods with extremely much less resolution at the same level of accuracy.

### **3. PHOTONIC NANOJET**

In this chapter, we numerically investigate scattering of light by a dielectric, non-magnetic cylinder by SEM. By the aid of spectral element method and the perfectly matched layer formulations presented in this work, we accurately solve scattering by dielectric microcylinders. Interesting cases, which finite difference time-domain method couldn't capture with a moderate resolution, are presented and discussed in this thesis. Verification of the obtained results is then presented using the analytical solution of Mie theory.

#### **3.1 Numerical Analysis Of Photonic Nanojets**

Light as an electromagnetic field interacts with different metallic or dielectric objects of any size and shape and provides novel features via scattering, reflection, refraction, and diffraction mechanisms [49-50]. To be more specific about light interaction with an object we can assume lossless (absorption free) dielectric micro-cylinders and excitation with a normally incident plane wave. The result of the interaction produces scattered light and strongly focused beam intensity at the back side of the medium (shadow side).

Optical engineering of micron sized dielectric cylinders and spheres produce nano-scale light manipulation. Divergence behaviour of the beam whether low or high, location of the focus (inside, at the boundary or outside of the cylinder), field enhancement, and transverse dimension of the spot size compared to the illuminating wavelength (how small with respect to the wavelength) are important parameters for the photonic jet. A substantial literature has been devoted to the verification of light focusing of photonic jet into sub-diffraction-limited sizes. Squeezing light at the shadow side as well as altering the location of focal point by means of different material and structural parameters (refractive index, radius, deformation, wavelength etc.) are unique properties to create interaction between enhanced intensity and matter interaction.

Experimental observation of photonic nanojets generated by latex microspheres of varying diameters was reported in Ref. 45 (See Figure 3.1). Low loss optical guiding of light can be accomplished by touching microspheres [48]. Propagation losses as low as 0.08 dB per microsphere was measured in the same study.

Photonic nanojets have been mainly explored by numerical methods based on FDTD analysis [30], [49], [58]. For instance, Figure 3.2 shows a visualization of a photonic nanojet as obtained by FDTD for a plane-wave-illuminated circular dielectric cylinder of  $5 \mu\text{m}$  diameter at a wavelength of  $5 \text{ nm}$ . The cylinder is embedded in vacuum and has a refractive index of 1.7. Very fine meshes are required in order to get accurate and reliable results with FDTD method. Besides, the excitation mechanism such as plane wave in free space may restrict the observation of special resonance modes. Later, analytical and semi-analytical attempts were introduced in the literature [50]. The majority of analytical studies are based on Mie theory. Rigorous Mie theory was used to analyse the fundamental properties of the photonic nanojet in [50]. Recasting eigenfunction solution of the Helmholtz equation into a Debye series. Ref. 30 provided detailed optics of photonic nanojets on dielectric cylinders.

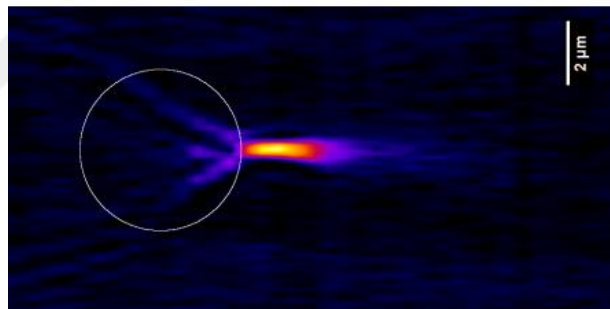


Figure 3. 1: Experimental observation of a photonic nanojet viewed along the optical axis of a  $5 \mu\text{m}$  -diameter dielectric sphere made of glass, [48].

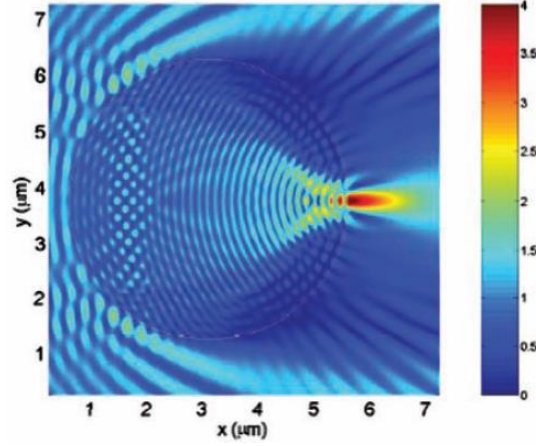


Figure 3. 2: Visualization of a photonic nanojet of a plane-wave-illuminated circular dielectric cylinder of  $5 \mu\text{m}$  diameter and has a refractive index of 1.7. [30].

As mentioned previously to have accurate results with FDTD method it is necessary to use finely discretized mesh which is a huge burden on the computational resources. Therefore, it is important to check/verify results with an alternative numerical method. In the present work, we implement the spectral element method to solve for the scattered electric field inside and outside the dielectric cylinder.

### 3.2 Photonic Nanojet Resulting From Dielectric Micro-cylinders

In the case of photonic nanojet where the scatterer is assumed to be an infinitely-long dielectric cylinder, the problem can be considered as a two-dimensional one when an incident plane wave propagating in a direction perpendicular to the cylinder axis is assumed. We consider an incident plane wave propagating in x-direction and the electric field is polarized in z-direction (i.e., in a transverse magnetic mode (TM<sub>z</sub>)):

$$E_z^{inc} = \hat{a}_z \exp(-jkx) \quad (3.1)$$

To solve the problem numerically, we should truncate the unbounded domain. Again, the formulation of the perfectly matched layer presented in chapter 2 is utilized for the domain truncation. Figure 3.3 shows, in the xy-plane, a dielectric cylinder represented by  $\Omega_c$ , free space region represented by  $\Omega_{FS}$ , and the PML region denoted by  $\Omega_{PML}$ , which represents the region surrounding  $\Omega_{FS}$ . On the outer boundary of  $\Omega_{PML}$ , zero-dirichlet boundary condition is simply imposed. In  $\Omega_{FS}$ , the homogenous Helmholtz equation is satisfied:

$$\nabla^2 E_z^s + k^2 E_z^s = 0, \quad (3.2)$$

in which  $E_z^s$  stands for the scattered electric field and polarized in the z-direction (TMz polarization is considered), and  $k$  is the wave number. While in  $\Omega_c$ , the following Helmholtz equation can be derived:

$$\nabla^2 E_z^s + k^2 \varepsilon_r E_z^s = k^2 (1 - \varepsilon_r) E_z^{inc}, \quad (3.3)$$

where;  $\varepsilon_r$  is the relative permittivity, and  $E_z^{inc}$  represents the incident plane wave. Throughout this work, we assume that the medium is non-magnetic ( $\mu_r = 1$ ). In  $\Omega_{PML}$ , the set of partial differential equations derived in chapter 2 must be satisfied. Under these assumptions, the refractive index is related to the relative permittivity as follows:

$$n = \sqrt{\varepsilon_r}. \quad (3.4)$$

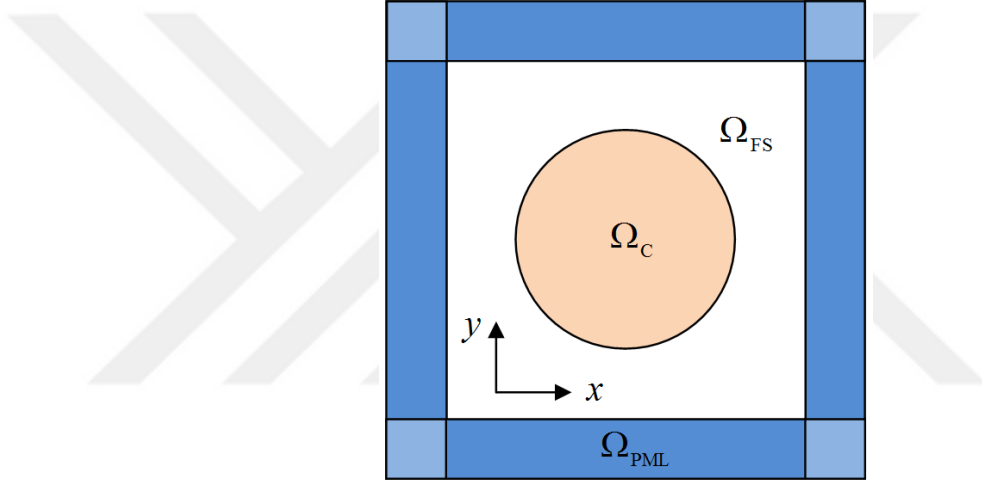


Figure 3. 3: Definition of the computational domain composed of a dielectric cylinder ( $\Omega_c$ ) embedded in the free space ( $\Omega_{FS}$ ) and truncated by PML.

Before we proceed further, it is worth to mention that the scattering dielectric cylinder is embedded in the free space that has a unity refractive index. From practical viewpoint, the cylinder can be embedded in another dielectric material that has a refractive index different than one, but it should be less than that of the scattering cylinder in order to obtain a photonic nanojet. What is important here is that the effective refractive index ( $n_{eff}$ ) which is expressed by:

$$n_{eff} = \frac{n_c}{n_m}, \quad (3.5)$$

where;  $n_c$  and  $n_m$  are the refractive indices of the cylinder and the surrounding material, respectively. In this work, we assume that the surrounding material is free space and we denote the effective index by  $n$  which, in turn, is the refractive index of

the scattering cylinder. The radius of the cylinder, denoted by  $R$ , is normalized with the wavelength  $\lambda$ .

A possible discretization of the computational domain by spectral element method when the dielectric cylinder radius is  $R = 3.5\lambda$ , is shown in Figure 3.4. In this figure, the GLL nodes are chosen as  $N \times N = 9 \times 9$  in each element for demonstration purpose. However in this work, finer resolutions are considered depending on  $R$ , for instance, when  $R = 3.5\lambda$ , the grid size of  $30 \times 30$  in each element is considered when the domain elements are chosen as shown in Figure 3.4 in order to achieve approximately 14 points per wavelength). It is important to mention that the number of elements should be increased as the radius of the cylinder increases due to the grid distribution of GLL nodes and since the radius is normalized with the wavelength.

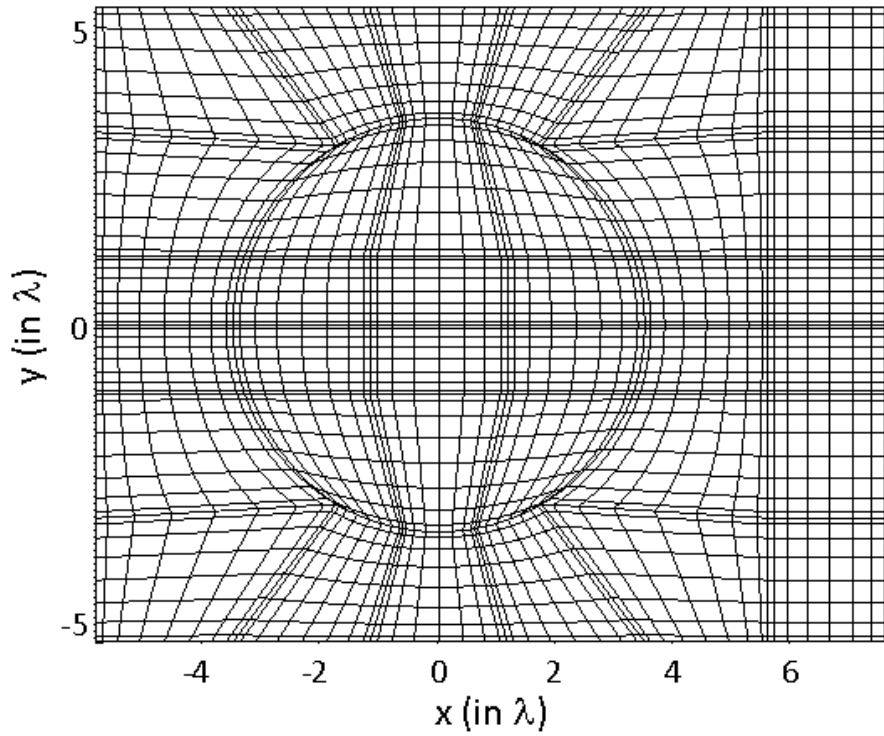


Figure 3. 4: A possible discretization of the computational domain at  $R = 1.5\lambda$ , and  $N \times N = 9 \times 9$  for each element (here, only elements corresponding to  $\Omega_{FS}$  and  $\Omega_C$  are shown).

Typical field solutions of photonic nanojets obtained by spectral element method are shown in Figure 3.5 for the cylinder radius  $R = 3.5\lambda$ , and for a refractive index  $n = 1.6$ . The plots in this chapter are illustrated using color map. In Figure 3.6, the photonic nanojet in Figure 3.5 is shown 3D. Figures 3.7 and 3.8 illustrate different photonic nanojets at  $(R = 5\lambda, n = 1.6)$  and at  $(R = 6.5\lambda, n = 1.4)$ , respectively.

It is worth to mention that, after obtaining the solution by spectral element method, which represents the scattered field, the incident plane wave is added to the scattered field in the subdomains  $\Omega_c$  and  $\Omega_{FS}$  only. One can produce the same spatial light distribution for the case where FDTD method is used. We have performed FDTD study and verified the exact photonic nanojet creations. With the application of SEM in frequency domain, it is easy to decompose the total field into incident and scattered field components.

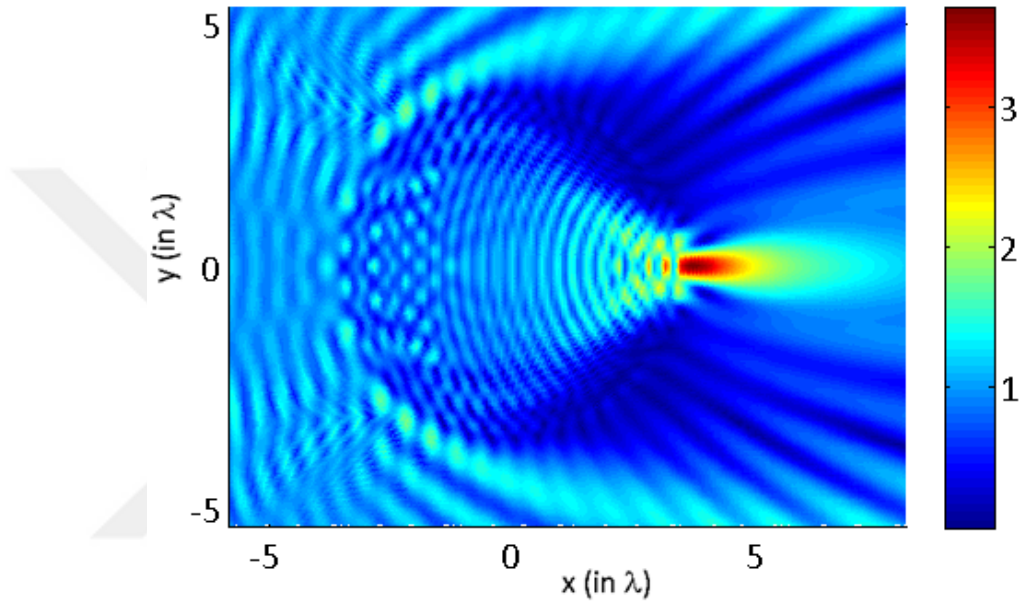


Figure 3. 5: Visualization of photonic nanojet at  $R = 3.5\lambda$  and  $n = 1.6$  .

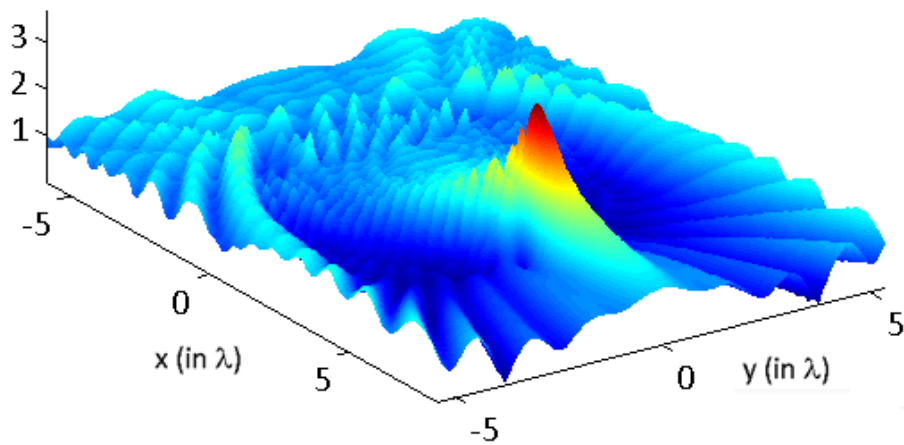


Figure 3. 6: 3D visualization of photonic nanojet at  $R = 3.5\lambda$  and  $n = 1.6$  .



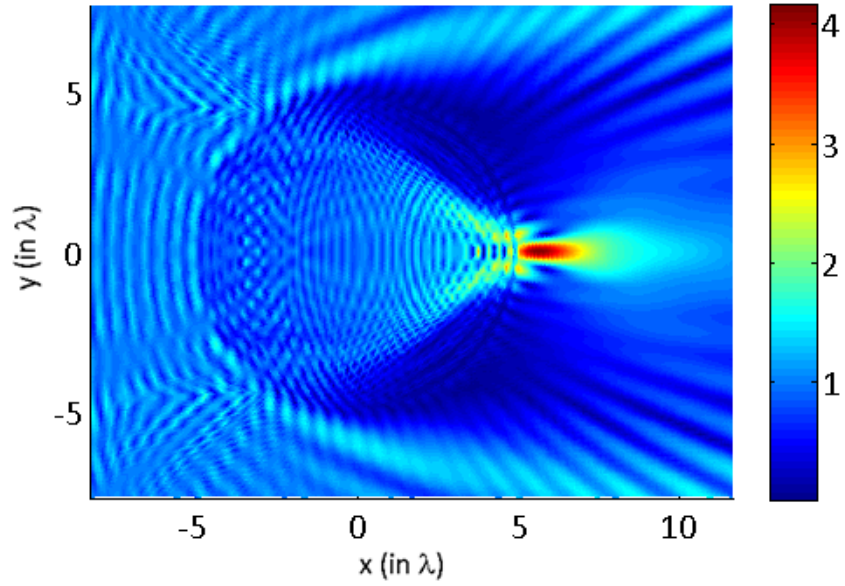


Figure 3. 7: Visualization of photonic nanojet at  $R = 5\lambda$  and  $n = 1.6$  .

The results presented in the previous figures demonstrate the capability of spectral element in the analysis of photonic nanojet generation. The input source interacts with the cylindrical object and gets focused at different locations as we change the radius and refractive index of the dielectric material. The focal point appears close to the surface in Figure 3.5 and it moves away from the back side along the optical axis ( $y=0$  line) in Figures 3.7 and 3.8.

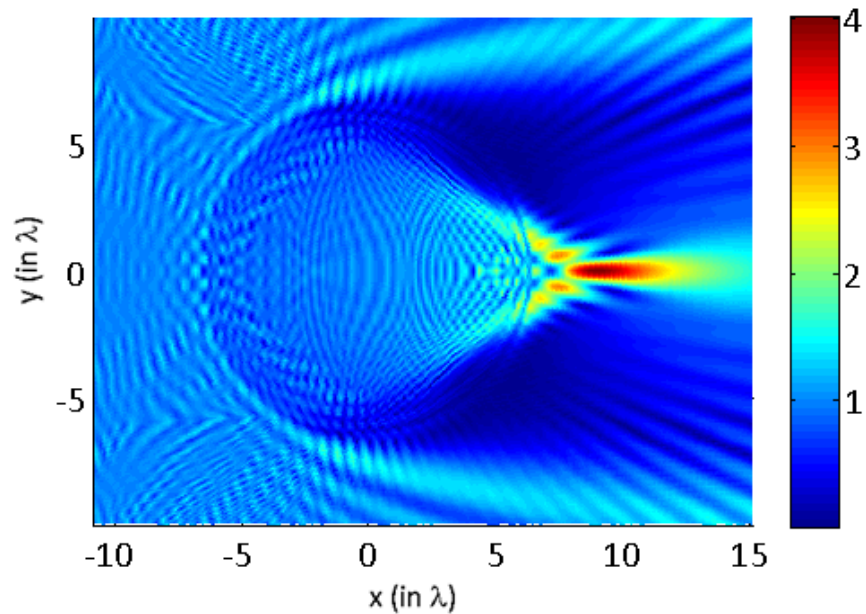


Figure 3. 8: Visualization of photonic nanojet at  $R = 6.5\lambda$  and  $n = 1.4$  .

### 3.3 Long Photonic Nanojets

In addition, photonic nanojets results with different structures. For instance, a loss-free dielectric micro-cylinder composed of two different materials is considered also in this section. The inner material has a refractive index and radius of  $n_3 = 1.40$  and  $R_3$ , respectively. Whereas the outer material is defined by  $n_2 = 1.50$  and  $R_2$ . The cylinder is placed along z-axis and embedded in a medium whose refractive index is  $n_1 = 1.33$ . This structure is illuminated by an incident plane wave propagating in x-direction and perpendicular to the cylinder axis. Four different cases are analysed by FDTD method and the results are presented in Figure 3.9. In case 1, the geometry is circular with  $R_3 = 2.2\lambda$  and  $R_2 = 2.5\lambda$ , where  $\lambda$  stands for the wavelength. Whereas in case 2, half of the cylinder is considered under same radii, and a rectangular slab is added for case 3. In case 4, we shrank the geometry to have an elliptic structure with  $R_{3,x} = 2.00\lambda$ ,  $R_{3,y} = 2.32\lambda$ ,  $R_{2,x} = 2.50\lambda$ ,  $R_{2,y} = 2.90\lambda$ . In all cases, it can be clearly observed that the generated photonic nano-jets are really ultra-long especially for case 4 (about  $20\lambda$  in x-direction). In addition, as seen from the intensity plot in Figure 3.9 (e), increasing the length of the nano-jet is accompanied with the decrease in the maximum field intensity.

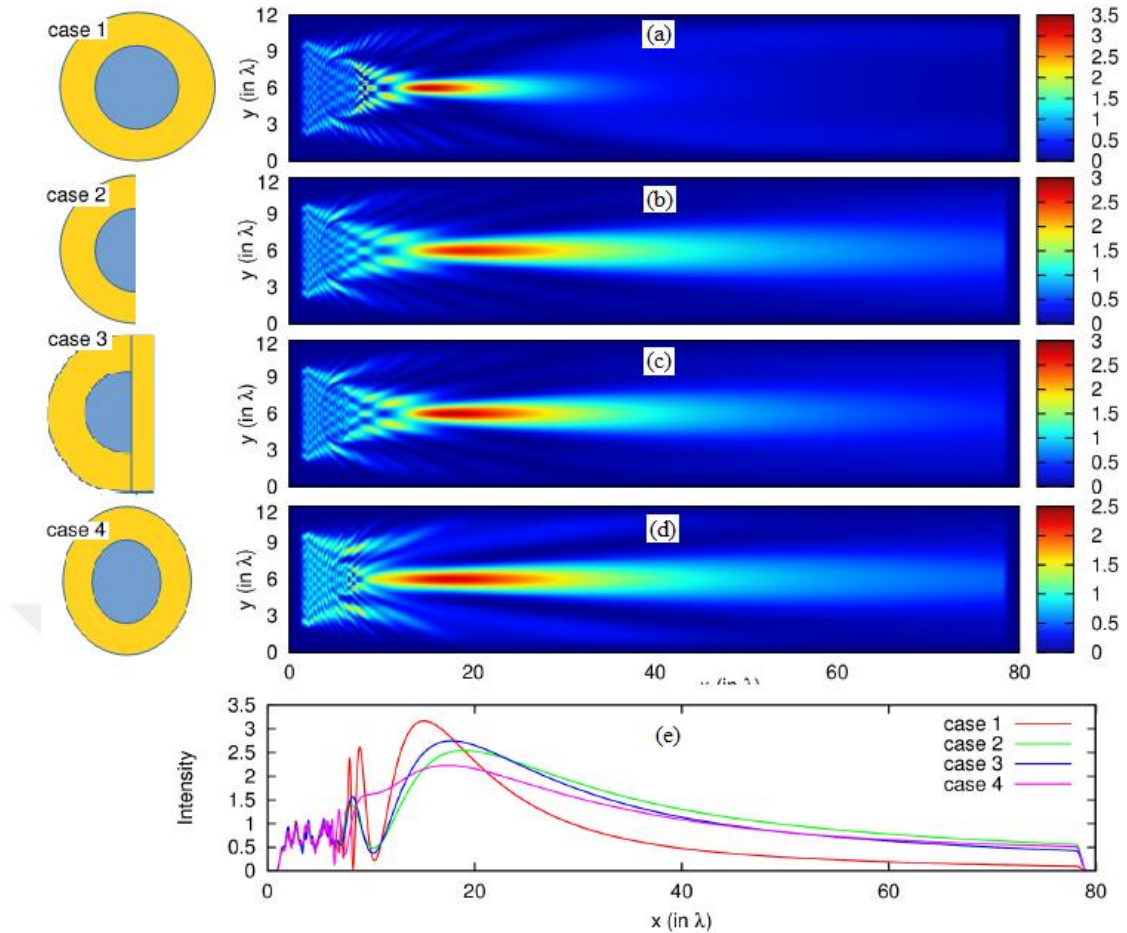


Figure 3. 9: Color mapping of field intensity as obtained by FDTD method for various shapes of dielectric micro-cylinders.

### 3.4 Whispering Gallery Modes In Dielectric Cylinders

Plane wave illumination of dielectric micro cylinders with FDTD method always produces an expected lensing/focusing effect so that the planar wave front of light gets tilted and focused at the optical axis. In the next example, we try to emphasize the advantage of SEM analysis over FDTD method. For example, when we change the refractive index of the cylinder and keeping the radius constant at  $3.50\lambda$  a resonance mode appears.

Figure 3.10 shows one of the captured resonance mode supported by a dielectric micro cylinder with  $R = 3.50\lambda$  and  $n = 1.7$ . The light focusing action with weak amplitude can be seen at the interior part of the cylinder. On the other hand, strong field localization at around the small cylinder appears with a highly symmetric light distribution in the form of two rings. Light is trapped by total internal reflection. Similarly, when we change the radius of the cylinder to  $R = 4.50\lambda$ , the resonance

mode again occurs if the refractive index value becomes 2.0. The result is presented in Figure 3.11. Light distribution with five rings is highly symmetric and strong field localization takes place at the exterior part of the micro cylinder. The evanescent field that leaks out of the dielectric cylinder radially is apparent in the plot. Figures 3.10 and 3.11 can be attributed to whispering gallery mode (WGM). The representation  $WGM_{m,l}$  indicates a WGM with the azimuthal mode number  $m$  and the radial mode number  $l$ . The resonance mode with different mode number is confined at the circumference of the cylinder by means of the total internal reflection mechanism. Using that notation we can express Figures 3.10 and 3.11 in terms of WGM resonances. By means of spectral element method we captured resonance modes as well as photonic nano jets cases. Commonly used FDTD method requires a different excitation scheme in order to gather the resonance modes of the micro-cylinder apart from the plane wave illumination.

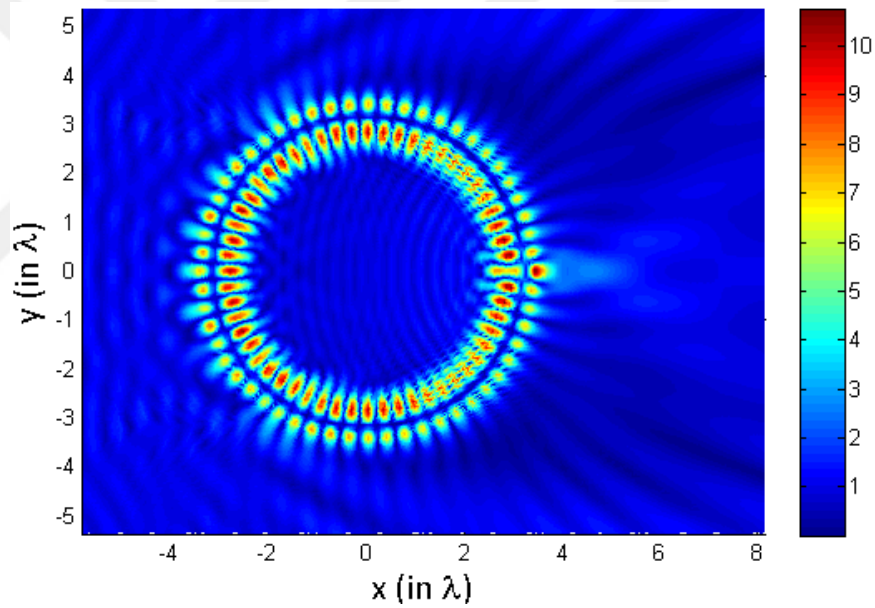


Figure 3. 10: Visualization of the evolution of a photonic nanojet for  $R = 3.50\lambda$  and  $n = 1.7$  . WGM representation gives  $m=28$  and  $l = 2$  .

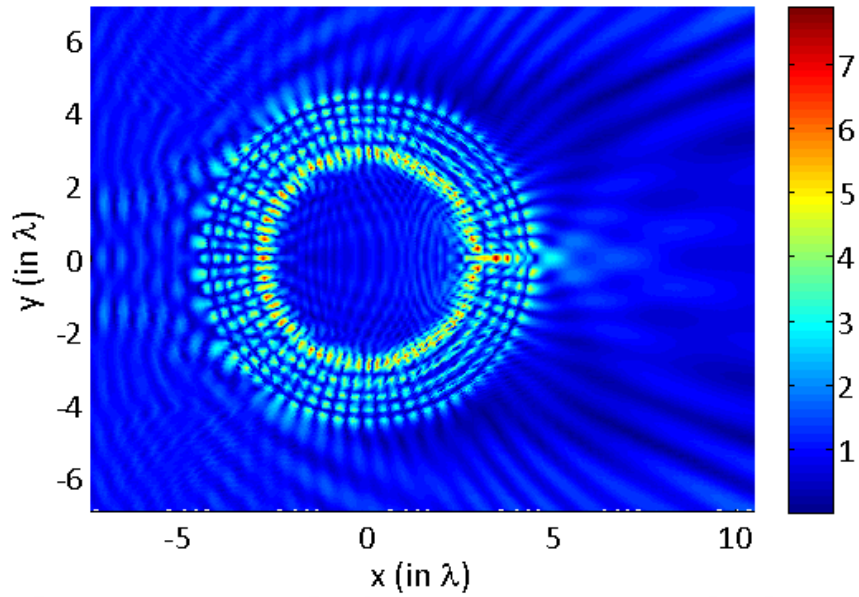


Figure 3. 11: Visualization of the evolution of a photonic nanojet for  $R = 4.50\lambda$  and  $n = 2$ . WGM parameters are  $m=34$  and  $l = 4$ .

We should point out that FDTD method gives us regular light focusing behavior but it does not indicate the creation of resonance mode. For instance, we have solved the problem at  $R = 3.50\lambda$  and  $n = 1.7$  by FDTD method using MEEP (a FDTD-based software developed by Massachusetts Institute of Technology-MIT). The corresponding real part of solution is shown on Figure 3.12. The plot is obtained by meshing the domain uniformly such that 40 nodes are used per one wavelength.

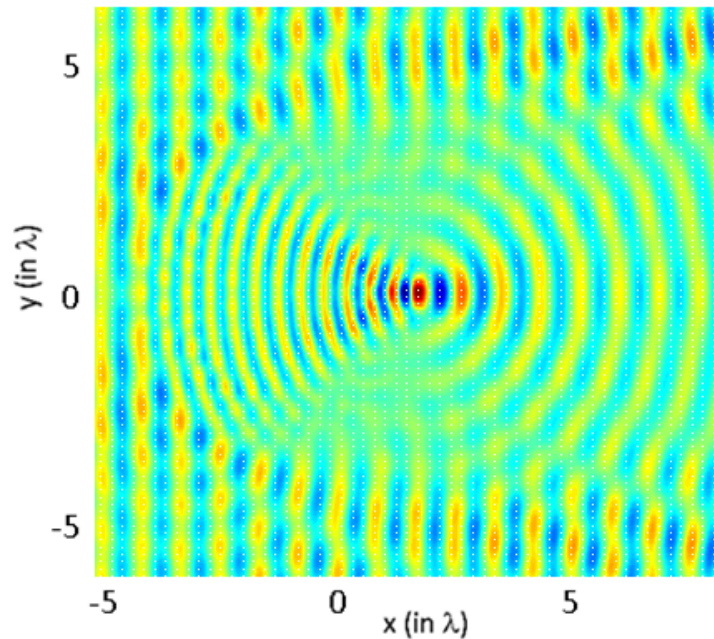


Figure 3. 12: FDTD visualization of the evolution of a photonic nanojet for  $R = 3.50\lambda$  and  $n = 1.7$ .

Phase matching condition has to be satisfied for FDTD method in order to excite the resonance mode. That condition requires special coupling techniques such as waveguide coupling or tapered optical fiber to excite the mode. The downside of the coupling approach is that the micro-resonator gets disturbed and the true resonance mode is modified due to the presence of the external waveguides.

### 3.5 Verification Of Whispering Gallery Modes

Photonic nanojet analysis can be performed analytically. Mie theory was intensively utilized in electromagnetic scattering problems. However, when the characteristic dimensions of the scattering object becomes much larger than the wavelength, improper algorithms may lead to considerable numerical errors [30]. In the examples presented in the previous section, where resonance takes places, the diameter of the micro-cylinder is larger than the wavelength but not too much. It is very important to check whether the analysis that Mie theory provides produces such resonance cases or not.

Itagi and Challener [30] provided the solution of the scattered light by a dielectric cylinder using Mie theory. Although their derivation is based on transverse magnetic mode (TE), we will use this analytical solution to verify our results. By Mie theory, the total-incident scattered magnetic field inside the cylinder can be expressed as:

$$h(\rho, \phi) = \sum_{m=0}^{\infty} a_m \cos(m\phi) J_m(nk\rho) \quad (3.6)$$

where;  $\rho$  is the Euclidean distance from the z-axis to a point lying inside the cylinder,  $\phi$  is the azimuth angle,  $J_m$  denote Bessel function of the first kind of  $m$ th order, and  $k$  is the wavenumber. The coefficients  $a_m$  are defined as:

$$a_m = c_m n \left[ \frac{H_m^{(1)'}(kR) J_m(kR) - H_m^{(1)}(kR) J_m'(kR)}{n H_m^{(1)'}(kR) J_m(nkR) - H_m^{(1)}(kR) J_m'(nkR)} \right], \quad (3.7)$$

in which  $R$  denotes the radius of the cylinder,  $H_m^{(1)}$  is Hankel function of the first kind of  $m$ th order,  $'$  denotes the derivative with respect to the argument of the function, and the coefficients  $c_m$  are given as:

$$c_m = \begin{cases} 1, & m = 0 \\ 2j^m, & m > 0. \end{cases} \quad (3.8)$$

This analytical solution is derived under the assumption that the cylinder is centered at the origin of the  $xy$ -plane. With the aid of this analytical solution, the magnitude of the magnetic scattered-incident field inside the cylinder is plotted for  $R = 4\lambda$  and  $n = 1.4$  in Figure 3.13. Here, we note that the truncation of the series at  $m = 150$  has negligible effect on the solution.

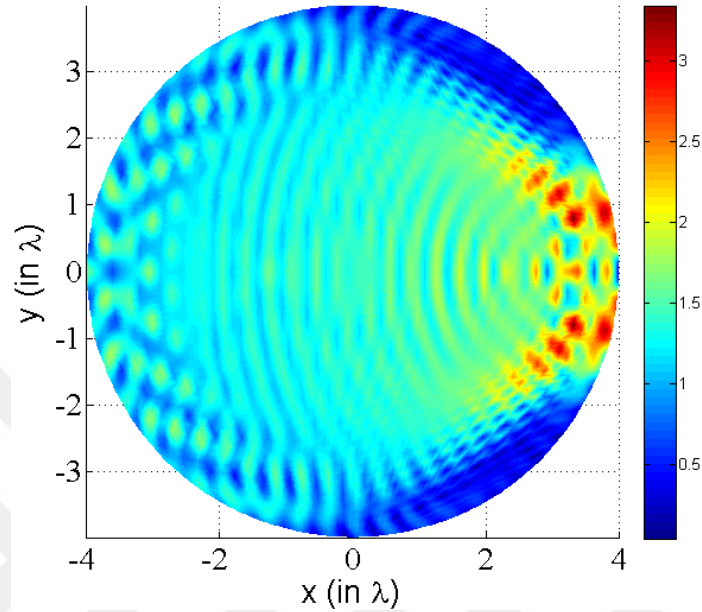


Figure 3. 13: Magnitude of magnetic scattered-incident field inside the cylinder for  $R = 4\lambda$  and  $n = 1.4$  .as obtained by Mie theory.

Considering that the accuracy of spectral element method is very high, and one of the resonance cases is captured at a refractive index of  $n = 1.7$  , we have solved the problem at the neighborhood of  $n = 1.7$  , for instance at  $n = 1.701$  and at  $n = 1.699$  , and the expected photonic nanojets were captured. So the index  $n = 1.7$  is very critical. It should be noted that since the cylinder radius is larger than the wavelength, Mie theory provides an approximate solution instead of the exact solution.

In other words, the solution obtained by Mie theory shows that there is no resonance at 1.7. We have performed a search loop in the neighborhood of 1.7 and captured the same resonance cases obtained by spectral element method. Figures 3.14 and 3.15 show the magnitude of the total magnetic field inside the cylinder at ( $R = 3.5\lambda$  and  $n = 1.6905$ ), and at ( $R = 4.5\lambda$  and  $n = 1.8911$ ), respectively.

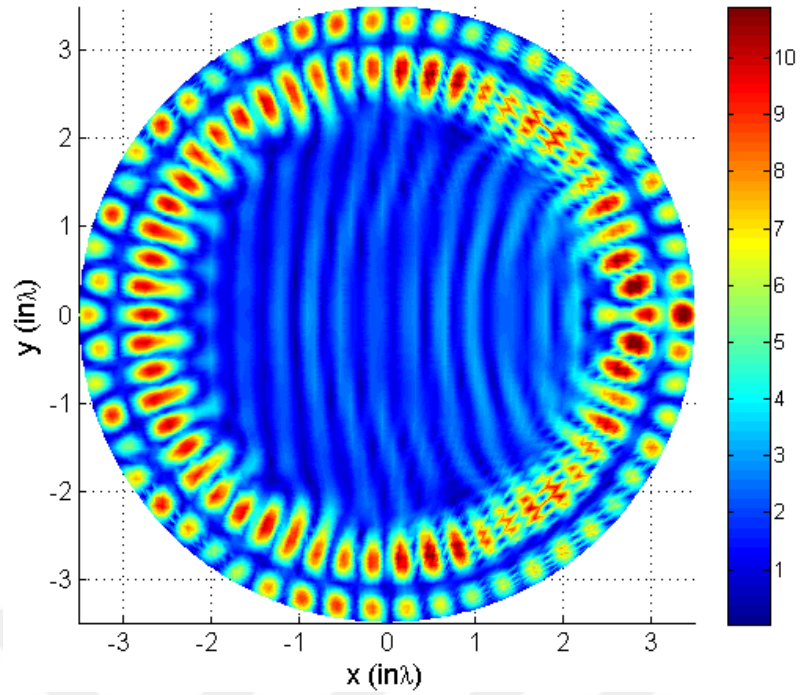


Figure 3. 14: The magnitude of the total magnetic field inside the cylinder at  $R = 3.5\lambda$  and  $n = 1.6905$ .

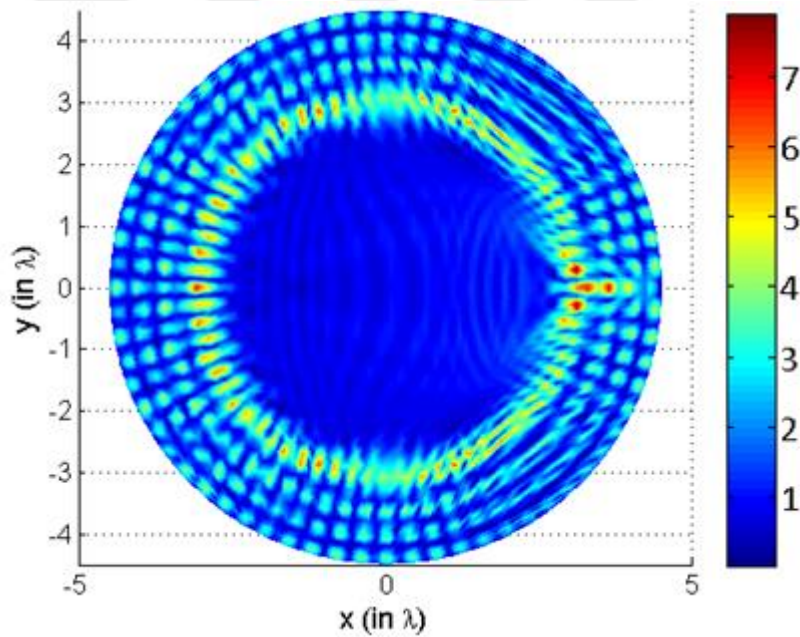


Figure 3. 15: The magnitude of the total magnetic field inside the cylinder at  $R = 4.5\lambda$  and  $n = 1.8911$ .

### 3.5 Conclusions

The formulation of perfectly matched layer is utilized together with SEM formulation. In addition, accuracy of SEM is demonstrated by solving for the scattered field from perfectly conducting cylinders. With the use of SEM, we could accurately perform



field analysis of photonic nanojets in dielectric lossless micro cylinders. Strong light focusing at the shadow side of the micro-cylinder is reported. Advantageous features of SEM allow the observation of commonly reported nanojet scenarios as well as the least pointed out transition region where resonance mode appears under certain conditions. The creation of whispering gallery mode types is plainly observed. One may be unaware of these special modes under the case of plane wave illumination with FDTD method that needs a coupling technique to excite the resonance the mode.

Previously reported results are exactly reproduced in the current study that validates the accuracy of the formulation and implementation of the numerical analysis based on SEM. The most important is the observation of the unique light distribution property that is associated with a resonance mode behavior. Depending on the parameters of the micro-cylinder, radius ( $R$ ) and refractive index ( $n$ ) strong field enhancement occurs and different number of rings appears within the cylinder. These features can be attributed to whispering gallery modes supported in micro-discs. The captured whispering gallery modes by spectral element method have also been verified using solution by Mie theory.



## 4. RESONANCE DYNAMICS OF DIELECTRIC CYLINDERS

In this chapter, first we explore the on resonance and off resonance optical response of dielectric cylinders excited by normal incident plane waves. Both analytical method based on Mie theory and numerical method implemented with spectral element method are undertaken in the study. We demonstrate that whispering gallery mode characteristic of resonance behavior is strongly dependent on the refractive index and radius changes. Two different scenarios are also considered in the current study in order to verify the strong field confinement; one is under Bessel beam illumination and the other is the introduction of non-homogeneity in the material forming the cylinder. Strong power enhancement up to three orders of magnitude is attainable with small micro-cylinders. Finally, the plane wave illumination is replaced by a point source in order to investigate the existence whispering gallery mode under this kind of excitation.

### 4.1 Tuning Optical Resonances Of Dielectric Cylinders

There are two special cases discussed in the previous chapter where an expected photonic nano-jet disappears, and instead, whispering gallery mode (WGM) is realized. These two cases can be realized at parameters  $(R, n) = (3.50\lambda, 1.70)$  and  $(R, n) = (4.50\lambda, 2.0)$ . In this work, we focus on the case when  $(R, n) = (3.50\lambda, 1.70)$  to exploit resonance behavior under the detuning of the structural and material parameters. Figure 4.1 shows the field magnitude inside and outside the dielectric cylinder of radius  $R = 3.50\lambda$  due to an illuminating plane wave as computed by SEM in the neighborhood of resonance at four different refractive indices: (a)  $n = 1.6995$ , (b)  $n = 1.7000$ , (c)  $n = 1.7005$ , and (d)  $n = 1.7010$ . Figure 4.1(b) shows the calculated field distribution for resonance case. It is clearly evident that whispering gallery mode characteristic confines photons at around the exterior part of the dielectric cylinder. When there is a small decrement in the refractive index value changing from 1.7000 to 1.6995 ( $\Delta n = 5 \times 10^{-4}$ ) as in the case in Figure 4.1(a), there is a mix of both WGM and photonic nano-jet. Two rings in the field distribution appear and focusing at the

boundary of the cylinder occurs. When we continue reducing the refractive index, the focal point of light is expected to move towards the exterior section of the cylinder and appearance of the symmetric field rings should be destroyed. Such claims can be evidenced in Figure 4.2(a). We keep the dimensions of the cylinder the same in the two figures, Figures 4.1 and 4.2, however, change the refractive index to a low value such as  $n=1.60$ , the disappearance of WGM action is obvious and only focusing behavior appears in the total field distribution.

It is logical to expect that if one continues to reduce the refractive index further, in addition to complete disappearance of the WGM behavior very weak light focusing at the outside of the cylinder survives. There will be an indication of only photonic nano-jets and WGM mechanism is lost. Photonic nano-jet will become longer and the peak position of the total field occurs further away from the shadow side of the micro-cylinder.

Contrary to the previous case, Figure 4.1(a), we now increase the refractive index by  $\Delta n = 5 \times 10^{-4}$ , then the total field plot in Figure 4.1(c) is obtained. Again, small perturbation is not enough to completely destroy the WGM. When we slightly continue to increase refractive index  $\Delta n = 1 \times 10^{-3}$ , photonic nano-jets dominates over WGM as demonstrated in Figure 4.1(d). Further increase of refractive index will focus light at the interior section of the micro-cylinder. Consequently, both WGM and photonic nano-jets are expected to be lost. To verify these claims, we prepared Figure 4.2(b) where the refractive index value is assumed to be  $n=1.80$ . Due to the increase in the refractive index contrast between the cylinder and the embedded environment, there is strong field focusing. It is important to note that the micro-cylinder is removed from resonance condition to off resonance region by large deviation of the refractive index. By means of Figure 4.2, it is now obvious and clear that reducing refractive index value such as  $n = 1.6$  yields photonic nano-jets type of field manipulation. On the other hand,  $n = 1.8$  enforces field localization taking place towards the inside of the cylinder. The field radiation pattern deviates from the nano-jet like behavior.

In Figure 4.3, the total field magnitude inside and outside of the dielectric cylinder is shown for the refractive index  $n = 1.7$  due to an illuminating plane wave as computed by SEM in the neighbourhood of resonance at (a)  $R = 3.5005$ , (b)  $R = 3.5010$ , respectively. As can be seen from the figure, a small increment in the radius of the micro-cylinder results in losing resonance behaviour even though the perturbed field

rings occupy the boundary of the structure. It should be noted that the deterioration of the resonance condition becomes more trivial as we continue to increase radius from 3.5005 to 3.010. When we compare Figure 4.1(d), Figure 4.2(b) and Figure 4.3(b), the radius increment case closely resembles the characteristics of the refractive index increment case.

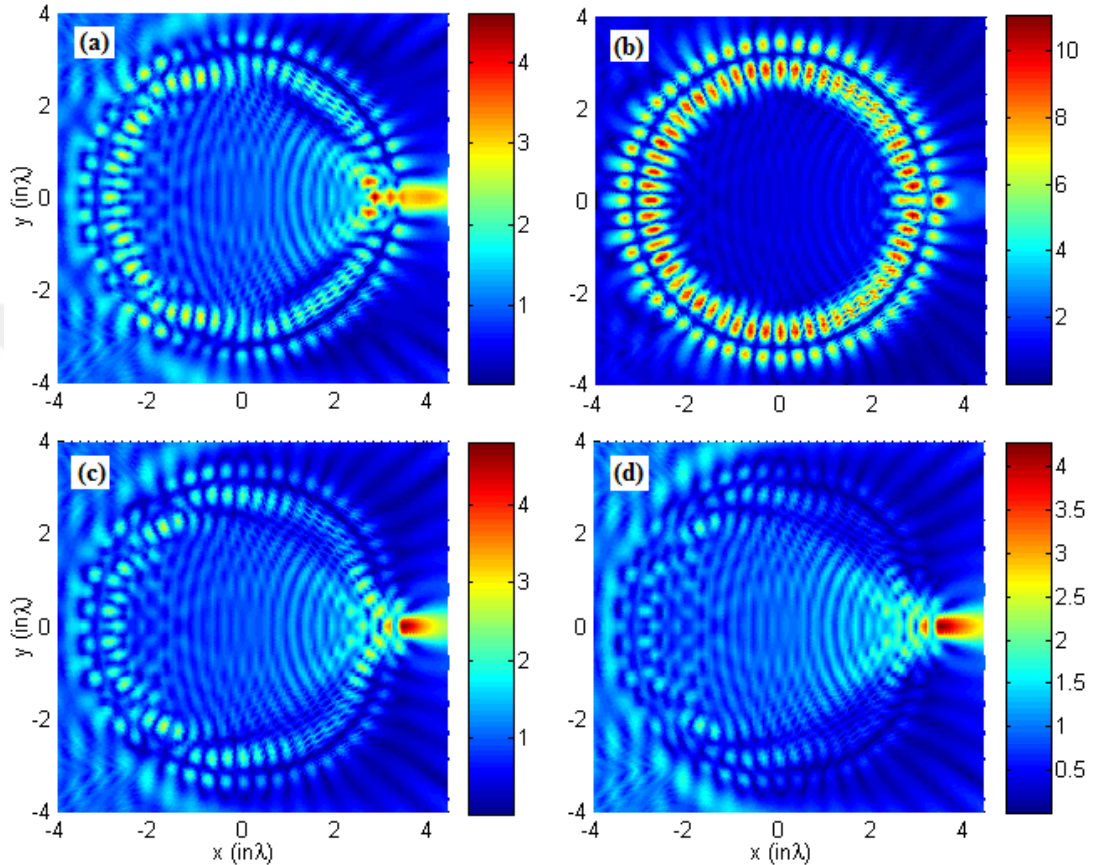


Figure 4. 1: Total field absolute value inside and outside of the dielectric cylinder of radius  $R = 3.5\lambda$  due to an illuminating plane wave as computed by SEM in the neighborhood of resonance at (a)  $n = 1.6995$ , (b)  $n = 1.7000$  (maximum), (c)  $n = 1.7005$ , and (d)  $n = 1.7010$ .

The transverse field distributions along the x-axis for four cases including resonance and off-resonance conditions are provided in Figure 4.4. The presence of the two rings is seen in Figure 4.4(b). The perturbation of the refractive index either reducing or increasing yields unique features. The resonance case provides the maximum field localization. As a result, the peak amplitude in Figure 4.4(b) is more than two times higher than the other cases. The deteriorated cases in Figure 4.4 a), 6(c) and 6(d) produce focusing of beam at certain positions and then exponentially decaying amplitude occupies the shadow side of the cylinder. In the resonance case, the field amplitude inside the cylinder stays almost the same. On the other hand, due to the field

focusing for the rest cases, there is slowly increasing field amplitude and quickly reaching at the maximum value at the focal point. One last remark regarding Figure 4.4(b) is that the absence of the symmetric field profile in resonance case is due to the case that we present the sum of incident and scattered field.

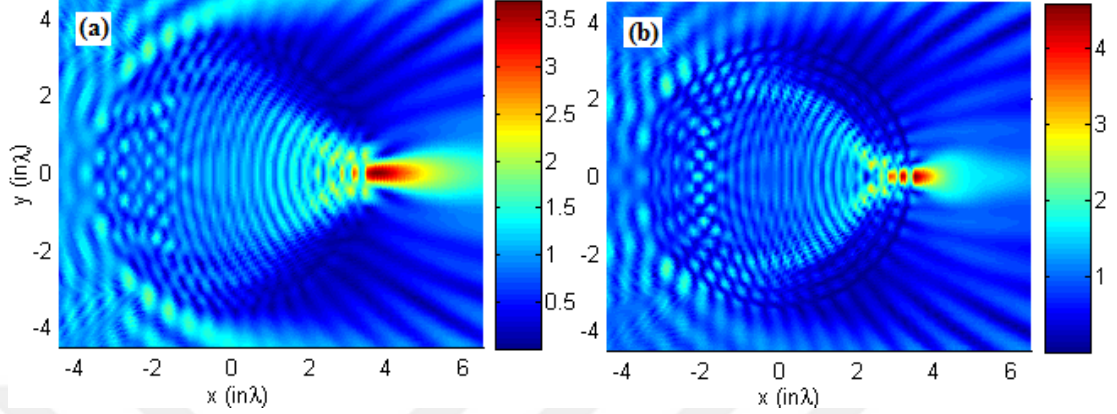


Figure 4. 2: (a) Total field absolute value inside and outside of the dielectric cylinder of radius  $R = 3.5\lambda$  due to an illuminating plane wave as computed by SEM in the neighborhood of resonance at (a)  $n = 1.6$  , (b)  $n = 1.8$  .

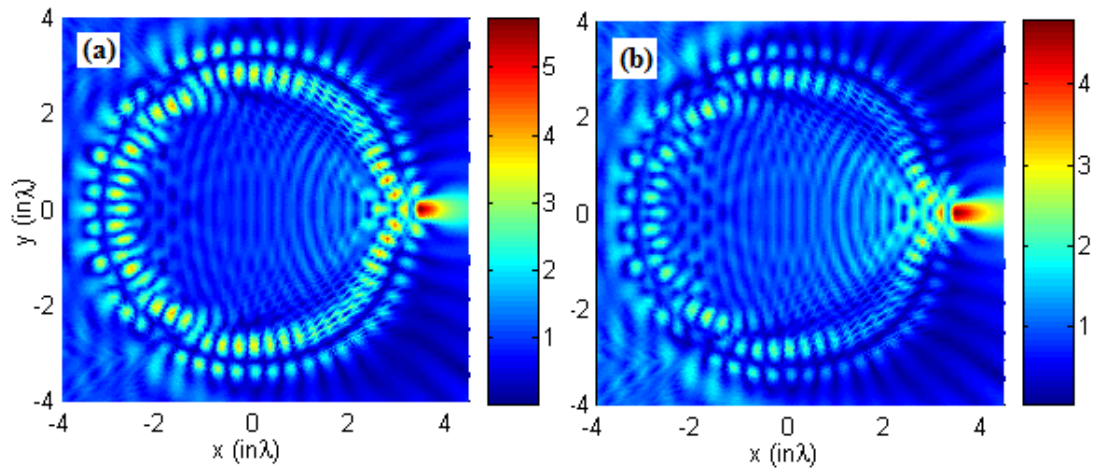


Figure 4. 3: Total field magnitude inside and outside of the dielectric cylinder of refractive index  $n = 1.7$  due to an illuminating plane wave as computed by SEM in the neighbourhood of resonance at (a)  $R = 3.5005$  , (b)  $R = 3.5010$  , respectively.

For another resonance condition appears with parameters of micro-cylinder,  $R = 4.50\lambda$  and  $n = 2.00$  . The absolute value of the total field for the resonance case is given in Figure 4.5(b). The WGM behaviour with five individual rings is observed. The deviations of the refractive index value produce the results presented in Figure 4.5(a), 5(c) and 5(d). Similar to previous case, the resonance condition provides largest field enhancement that has almost two times higher peak value compared to the rest.

Depending on the case, whether refractive index decreases or increases, the field focusing occurs and WGM characteristic disappears.

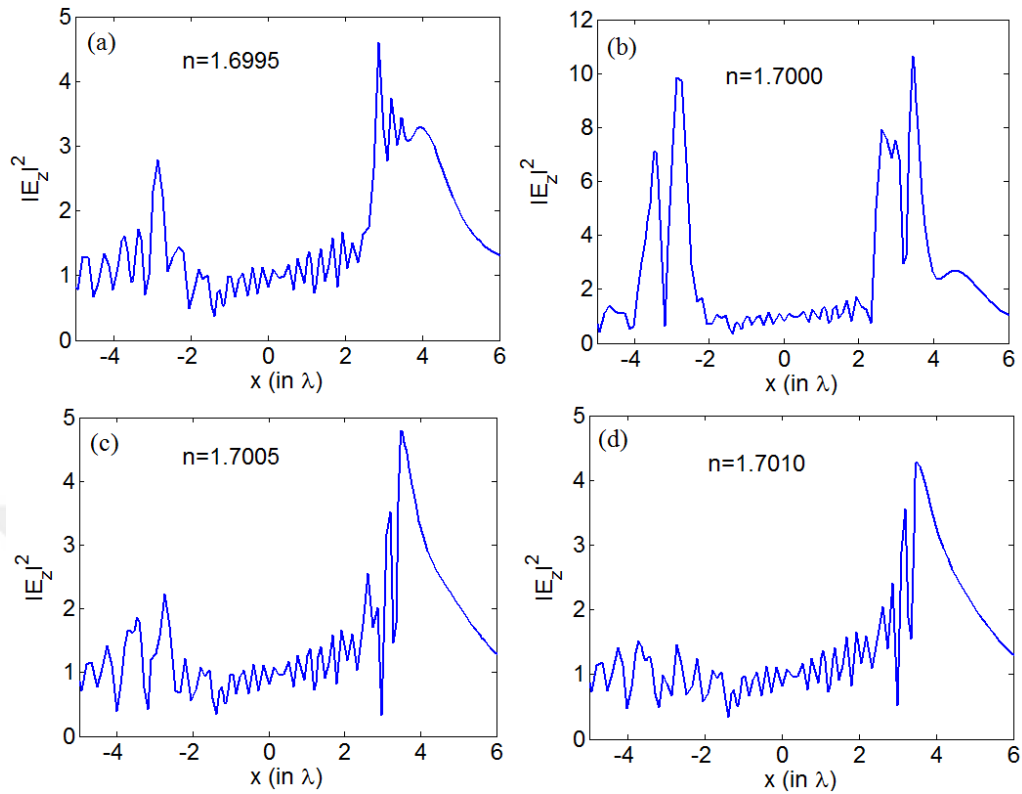


Figure 4. 4: Magnitude of the electric field profile along the x-axis passing through the micro-cylinder's center. Data presented in Figure 4.1 is used to plot the transverse field variations for four cases: (a):  $n = 1.6995$ , (b)  $n = 1.7000$  (on-resonance), (c)  $n = 1.7005$ , and (d)  $n = 1.7010$ .

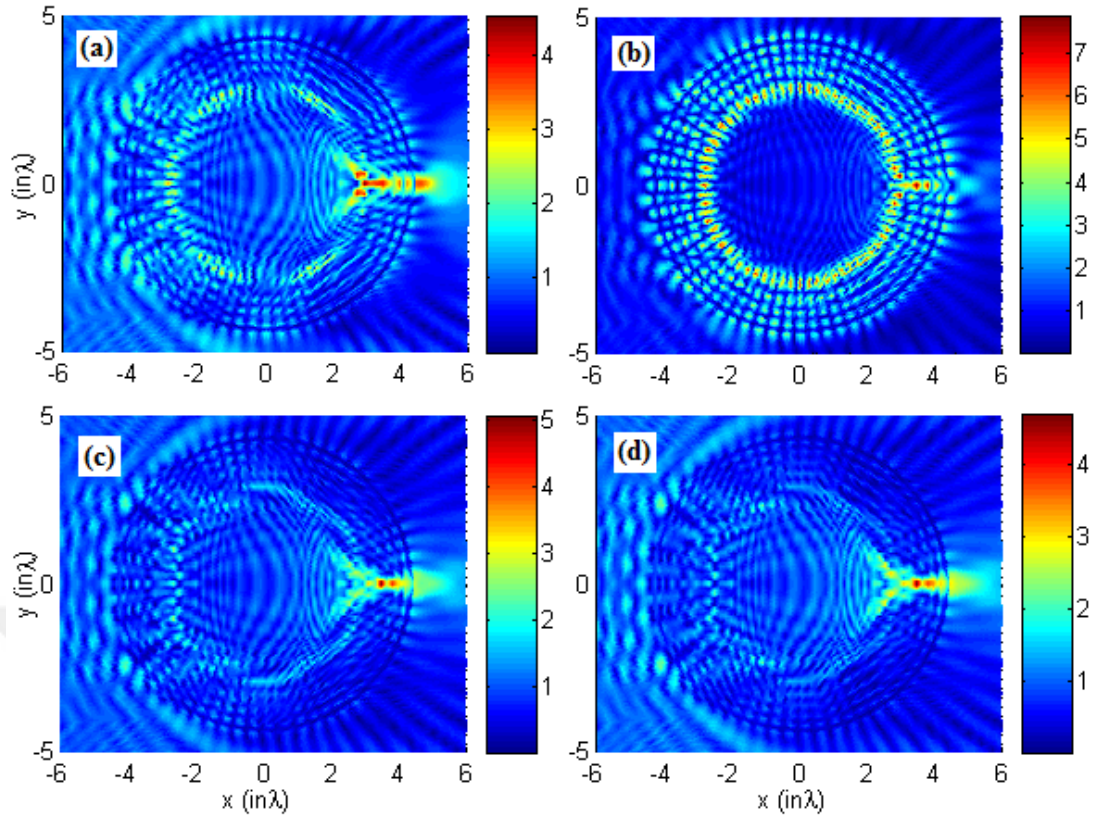


Figure 4. 5: Magnitude of the total field inside and outside of the dielectric cylinder of radius  $R = 4.5\lambda$  due to an illuminating plane wave as computed by SEM in the neighbourhood of resonance at (a)  $n = 1.9995$ , (b)  $n = 2.0000$  (maximum), (c)  $n = 2.0005$ , and (d)  $n = 2.0010$ .

## 4.2 Results Of Mie Theory

Figure 4.6 shows the magnitude of the field inside the dielectric cylinder of radius  $R = 3.5\lambda$  due to an illuminating plane wave as calculated by Mie theory in the neighbourhood of resonance at Figure 4.6(a1)  $n = 1.6795$ , Figure 4.6(b1)  $n = 1.6800$ , Figure 4.6 (c1)  $n = 1.6805$  (maximum). The contributions of the mode  $m = 27$  to the overall absolute value of the field are shown in Figure 4.6 (a2), Figure 4.6 (b2) and Figure 4.6 (c2) at  $n = 1.6795, 1.6800$ , and  $1.6805$ , respectively.

In order to verify the presence of the resonance and emphasize its features, we deployed Mie theory. Thanks to the analytical formulations, resonance cases can be easily calculated. The electric field plots for the inside of the cylinder assure the presence of the modes.



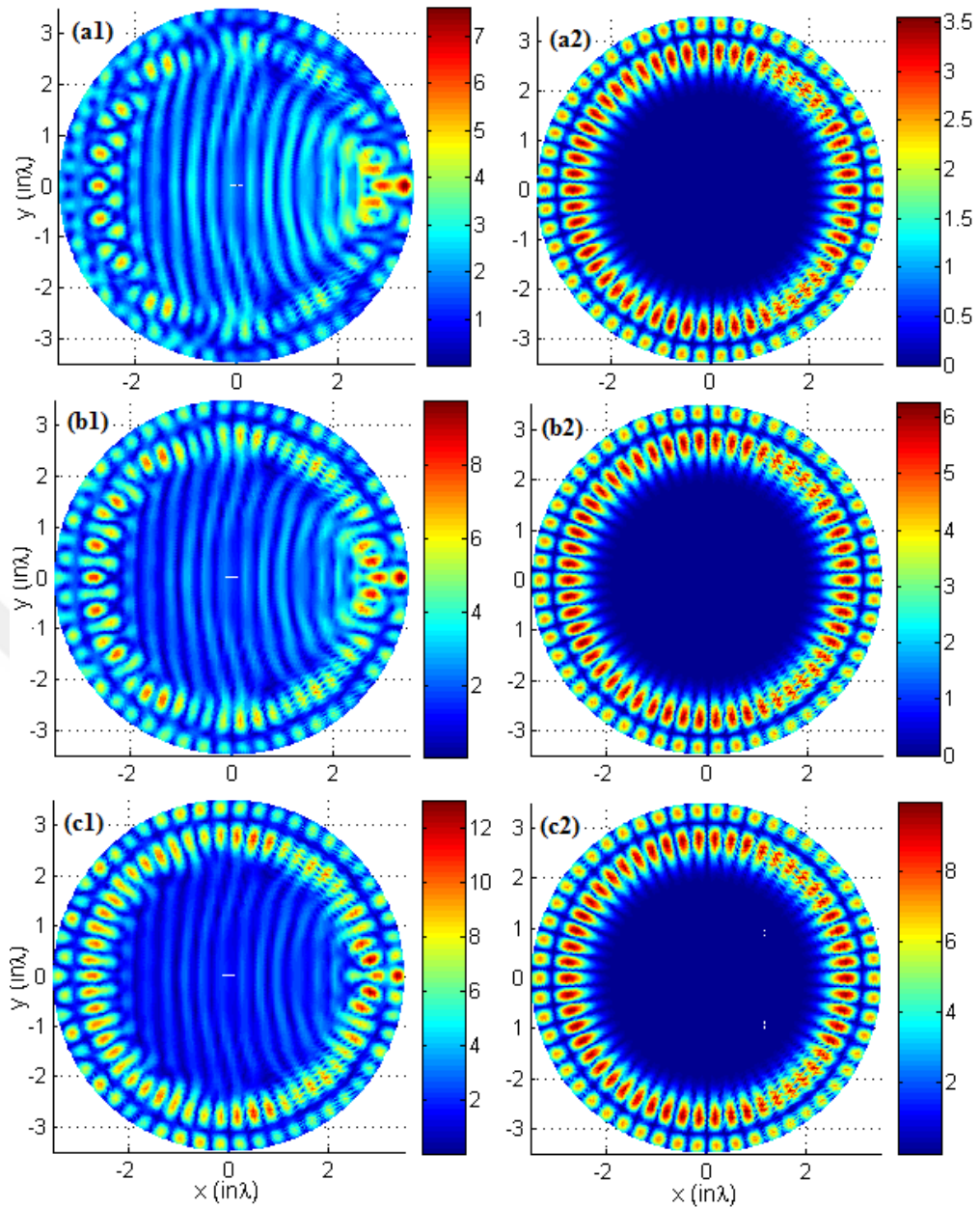


Figure 4. 6: Field magnitude inside the dielectric cylinder of radius  $R = 3.5\lambda$  due to an illuminating plane wave as calculated by Mie theory in the neighbourhood of resonance at (a1)  $n = 1.6795$ , (b1)  $n = 1.6800$ , (c1)  $n = 1.6805$  (maximum). The contributions of the mode  $m = 27$  to the overall intensity are shown in (a2), (b2) and (c2) at  $n = 1.6795, 1.6800, \text{ and } 1.6805$ , respectively.

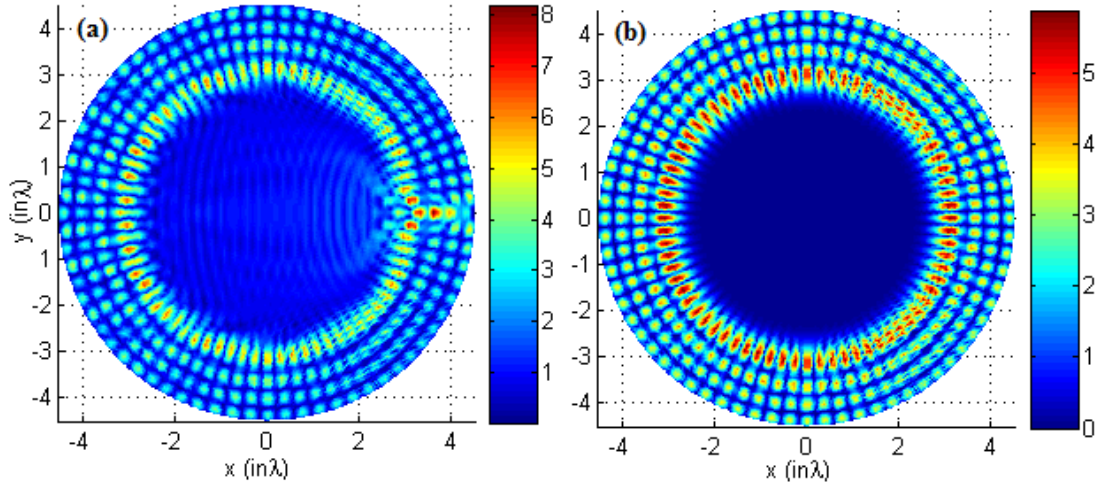


Figure 4. 7: Total field magnitude inside the dielectric cylinder of radius  $R = 4.5\lambda$  and at  $n = 1.97259$  due to an illuminating plane wave as calculated by Mie theory: (a) For  $m := 0 \rightarrow 120$ , (b) The contribution of the mode number  $m = 36$ .

In order to be consistent, we also calculated the resonance values of the second case with Mie theory. We repeated Mie theory calculation to obtain the resonance mode for the second test case  $R = 4.5\lambda$ . In Figure 4.7, the magnitude of electric field obtained from Eq. 3.6 is shown inside the dielectric micro-cylinder at  $R = 4.5\lambda$  and  $n = 1.97259$  for: (a) the summation interval  $m := 0 \rightarrow 120$ , and (b) Mode contribution to resonance at  $m = 36$ . Here, we should note that the series truncation ( $m := 0 \rightarrow 120$ ) is considered as Mie theory encounters numerical divergence [3], [73], [74]. The deviation in the refractive index value is 1.37%. As it can be clearly seen, results obtained by Mie theory and SEM have high degree of match. In order to avoid any confusion, it is worthy to point that the fifth ring shown in Figure 4.5(b) lies near to the surface of the cylinder but not inside the cylinder, and that ring is absent in Figure 4.7 as the field is plotted only inside the cylinder.

In order to make correct comparisons between SEM and Mie theory, we fixed the radii values to either  $R = 3.50\lambda$  or  $R = 4.50\lambda$  and search the resonance by using Mie theory. When we obtain refractive index value, the difference between the two methods is very small (the differences between SEM and Mie theory are 1.14% and 1.37% for  $(R, n) = (3.50\lambda, 1.70)$  and  $(R, n) = (4.50\lambda, 2.0)$ , respectively). That difference is due to the nature of the two methods: computational approach vs. analytical one, and the two do have relatively small numerical errors.

### 4.2.1 Discussions

Either strong focusing of light or enhanced field localization is very important in the field of nano-photonics. Most recent approaches attempt to achieve such aims with plasmonics or meta-material based designs. Meanwhile, simple dielectric micro-cylinder scalable to any electromagnetic spectrum possesses the two unique properties under different structural parameters.

Light interaction with cylindrical and spherical particles of different size has been studied for more than 100 years [75]. Unique light manipulation capabilities of such scatterers has given rise to important technological applications covering diverse fields from communication, to metrology, and spectroscopy.

The two different operating regimes show unique light manipulation features. The resonance condition, WGM is the output of constructive interference effect yielding strongly localized field distribution with symmetric pattern. Any detuning in the size of the cylinder or material refractive index affect the nature of light interference. The resonance condition is associated with Q-factor. As long as there is high-Q in the structure, the sharp peak in the spectrum domain can be easily detuned via small changes of the radius or refractive index. The other operating region, photonic nano-jet is a consequence of lensing effect. Again the radius and refractive index value determine the location and beam diverging characteristics of the focused light at the back side of the cylinder.

The goal of the study is to question the response and sensitivity of the resonances of dielectric micro-cylinders to opto-geometric parameters under normal incident plane wave condition. We altered refractive index and radius of the dielectric cylinder in order to see their crucial roles for manipulating photons. As demonstrated in the results, both refractive index and radius variation have critical role for losing the resonance condition.

Even though we did not provide results with respect to wavelength detuning, the diameter of the micro-cylinder is expressed in terms of operating wavelength. As a result, the sensitivity of the resonance condition to R change is the same with respect to wavelength.

Even though we explore single optical resonator with SEM, it is logical to extend the analysis domain covering more than one resonator such as coupled micro-disk or micro-spheres. Such a coupled system can be in general composed of different size

and shape [48], [76]. Besides, different type of light illumination can be implemented. Perfect circular symmetry for the cylinders is accepted in the analysis. It is important to explore the effect of certain type irregularities that may occur in practice during the fabrication of the structure. That aspect will be studied in a separate study in the future. It is important to point out that the two resonance conditions are selected to test the on and off resonance behaviours. It is expected to have other resonance cases with different number of rings for various values of radius and refractive index of the micro-cylinders. We do not intend to capture and list all resonance conditions such that other number of rings appears in the field plot. Instead of that, detuning parameters for the two selected cases with two and five rings inform us about the basic properties of the micro-cylinders under the plane-wave illumination.

Near-field imaging, high-resolution microscopy, optical lithography, low threshold micro-cavity lasing, and single molecule sensing are some of the potential applications of small micro-cylinder [77]. We should note that there is always trade-off between resonance and off-resonance operations. One usually desires to have high-Q resonance condition in some applications, such as low threshold micro-cavity lasing. On the other hand, any unintended perturbation of the structural parameters may destroy the resonance condition and one cannot obtain the targeted output. Very sensitive resonator biosensors become also susceptible to other environmental changes as well. Careful selection of the micro-cylinders' parameters is important depending on the targeted applications.

### 4.3 Resonance Under Different Mechanism

Before we present the analysis under the perpendicular incident plane wave excitation, it is worthy to consider a different excitation scheme. That is, we briefly test the resonance system with Bessel beam in order to realize the consequences on the resonance behaviour. Such type of source is important especially for particle manipulation and optical tweezers [78].

The mathematical expression for the new type of source is given as follows:

$$E_z^{inc} = J_0(\gamma |y|) \exp(-jx \sqrt{k^2 - \gamma^2}) \quad (4.1)$$

where  $\gamma = 0.6$ , and  $J_0$  is the Bessel function of the zero order. In Figure 4.8(a), the magnitude of the electric field in the main lobe of the Bessel beam is shown and it is equal to 0.1666 in the point propagating tangentially to the periphery of the cylinder.

The magnitude of the total field inside and outside the cylinder, whose radius and refractive index are set to  $R = 3.5\lambda$  and  $n = 1.7$ , is shown in Figure 4.8(b). As can be seen from the figure, it is not necessary for two-ring resonance mode to appear with plane wave illumination only, but different excitation mechanisms may produce WGM whose field magnitude depends on the illuminating wave magnitude near to the periphery of the cylinder. It is important to note that, under plane wave illumination and at the parameters, i. e., at  $R = 3.5\lambda$  and  $n = 1.7$ , the magnitude of the total incident-scattered field is found to be 10.9 as shown in Figure 3.10, and drops to around 2 in the case of illumination by Bessel beam.

Mie theory which solves Maxwell's equations with a quasi-analytical solution rigorously was intensively utilized in electromagnetic scattering problems. Photonic nano-jet analysis, by the aid of Mie theory, can also be performed analytically as shown earlier in this chapter. Although when the characteristic dimensions of the scattering object becomes much larger than the wavelength, improper algorithms may lead to considerable numerical errors [21], Mie theory can be used to visualize the details of resonance in dielectric micro-cylinders while having a good match with SEM [60]. However, if some perturbation is introduced to the problem, the analytical solution then turns to be hardly found. For instance, if a square region inside the dielectric cylinder is assigned with different refractive index, Mie theory cannot be applied.

For the purpose of investigating the resonance behavior, a square region of difference refractive index is introduced and whole problem is solved by the SEM. In figure 4.9(a), a cylinder of  $R = 2.8\lambda$ , and  $n_1 = 1.5$  is illuminated by a plane wave, and a typical photonic nanojet is produced. A square region of  $1.9\lambda \times 1.9\lambda$  with refractive index of  $n_2 = 1.33$  is introduced in the center of the cylinder as shown in Figure 4.9(b). As it can be seen clearly from the figure, the photonic nanojet behavior is almost destroyed. However, under resonance modes, such perturbation has almost no effect on the field forming resonance regardless of the value of  $n_2$  as long as this material does not cover the region where resonance takes place. The corresponding figures are not included for the sake of brevity, however, we only show the case when a square region of  $2.4\lambda \times 2.4\lambda$  with refractive index of  $n_2 = 1.33$  is located at the center of a cylinder whose radius and index are  $R = 3.5\lambda$  and  $n_1 = 1.7$  as seen from the color map

plot in Figure 4.10. The effect of the square region on the scattered field from the cylinder can be clearly observed, however, the resonance behavior remains unchanged compared with Ref. 59. The associated field magnitude along the x-axis is presented in Figure 4.11.

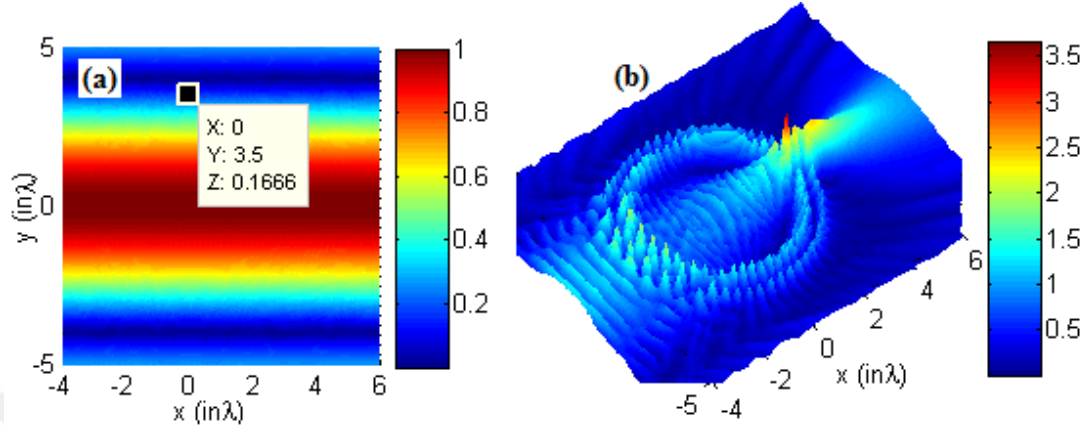


Figure 4. 8: Illumination by Bessel's beam at  $\gamma = 0.6$  (a) magnitude of the exciting incident field produced by Bessel's beam, and (b) magnitude of the total scattered-incident field (3D view) inside and outside the dielectric cylinder whose parameters are  $R, n = 3.5 \lambda, 1.7$ .

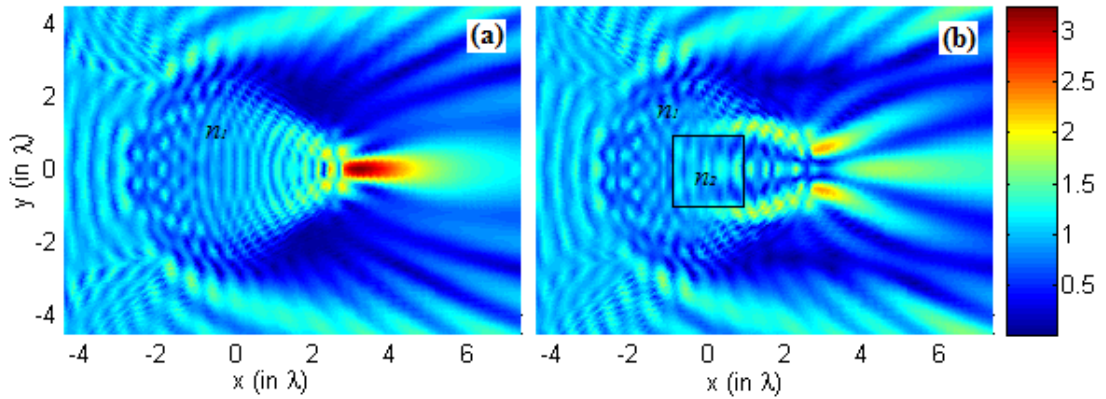


Figure 4. 9: Magnitude of the total field inside and outside a dielectric cylinder of radius  $R = 2.8 \lambda$  for (a)  $n_1 = 1.5$ , and (b)  $n_1 = 1.5, n_2 = 1.33$ .

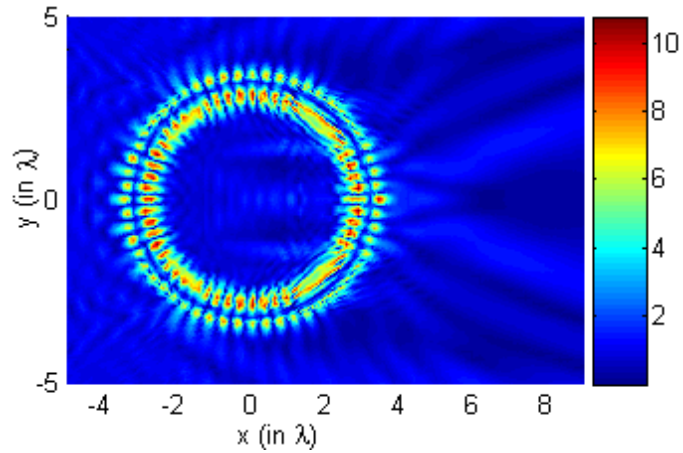


Figure 4. 10: Magnitude of the total field inside and outside a dielectric cylinder of radius  $R = 3.5\lambda$  at  $n_1 = 1.7$ , and has a square region of  $n_2 = 1.33$  and  $2.4\lambda \times 2.4\lambda$  at its center.

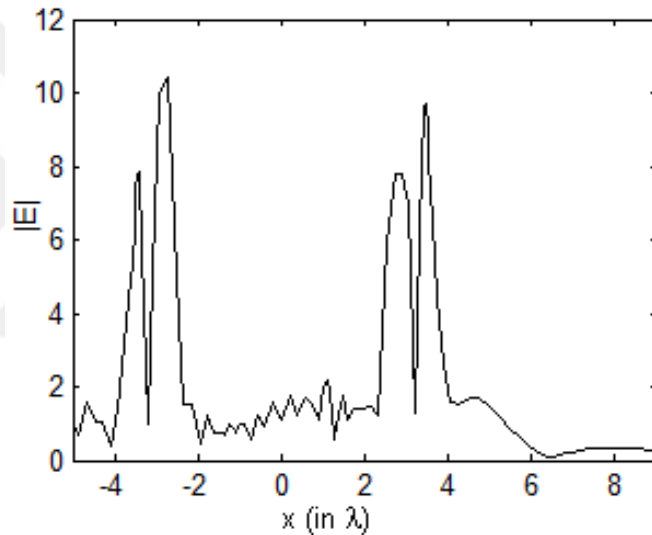


Figure 4. 11: Magnitude of the total field along x-axis for the case in Figure 4.8.

#### 4.4 Resonance Mode Tracking

We focus on the two-ring resonance condition, i.e., the case when  $(R, n) = (3.50\lambda, 1.70)$  is taken as the starting point. From this configuration, we traced the same type of resonance condition and monitored field enhancement property of the micro-cylinder.

Although, in section 4.1 we demonstrated that an increment in the refractive index of about  $\Delta n = 0.0005$  or a similar one in the radius  $R$  leads to the absence of WGM, one should not forget that it is a one-to-one relationship between  $R$  and  $n$ . That is, if  $n$  is taken as 1.60, one can search for the radius at which the same type of resonance takes

place, hence there is a corresponding value for a different refractive index value. As a result, one can assume that searching for possible  $R$  and  $n$  values would give us specific trend for a particular WGM.

For this purpose, we try in this work to capture the pairs of  $R$  and  $n$  so that WGM behavior is dominant over the photonic nano-jet case that is special form of lensing property with small spot size. Such tracking is performed by SEM.

In Table 4.1, 16 pairs of  $R$  and  $n$  are presented. All of these cases provide the same type of WGM, i.e., two-ring resonance mode. It is worth to point that the radius of the dielectric cylinder, and hence the dimensions of the computational domain is normalized with respect to the incident wavelength  $\lambda$  to make consistent comparison between each case.

Some pairs from the table are chosen for demonstration purpose. In Figure 4.12, we show the magnitude of the total field, i.e., sum of scattered and incident field under the plane wave illumination. The designated area covers the inside and outside of the dielectric cylinders with the following parameters: (a)  $(R, n) = (3.5198\lambda, 1.69)$ , (b)  $(R, n) = (3.2245\lambda, 1.85)$ , (c)  $(R, n) = (2.847491\lambda, 2.1)$  and (d)  $(R, n) = (2.7198007\lambda, 2.2)$ . It is worth to point that all figures have the same physical boundaries in the x-y plane. The rings sizes and refractive indices vary for each figure. One can surprisingly observe the large field magnitudes especially in the cases of Figure 4.12 (c) and (d) as compared to the other two cases (Figure 4.12 (a) and (b)) while the magnitude of the exciting plane wave is unity for each case. The resonance condition in all cases produces highly localized light with large field magnitude. Exceptional case with very high light magnitude can as well occur. Figure 4.12 (c) and (d) can be given as an example for this observation. It is worth to mention that the field magnitude increases as we continuously decrease the radius of the cylinder.

The associated normalized intensity (square of total field) to the case shown in Figure 4.12 (c) along the x-axis is plotted in Figure 4.13. While the intensity of the incident plane wave is unity, the resultant intensity inside the cylinder reaches about  $4 \times 10^5$  times that of the incident intensity. Such intensity is extremely high and it is not discussed in the literature to the best of our knowledge.



Table 4. 1:  $(R, n) =$  pairs at which 2-ring resonance appears

$n$	$R$ (in $\lambda$ )	$n$	$R$ (in $\lambda$ )
1.50	3.9380	1.90	3.14158
1.60	3.7082	1.95	3.06267
1.69	3.5198	2.00	2.98752
1.70	3.5000	2.05	2.915878
1.72	3.4607	2.10	2.847491
1.75	3.4034	2.15	2.7822063
1.80	3.3117	2.20	2.7198007
1.85	3.2245	2.25	2.6600939

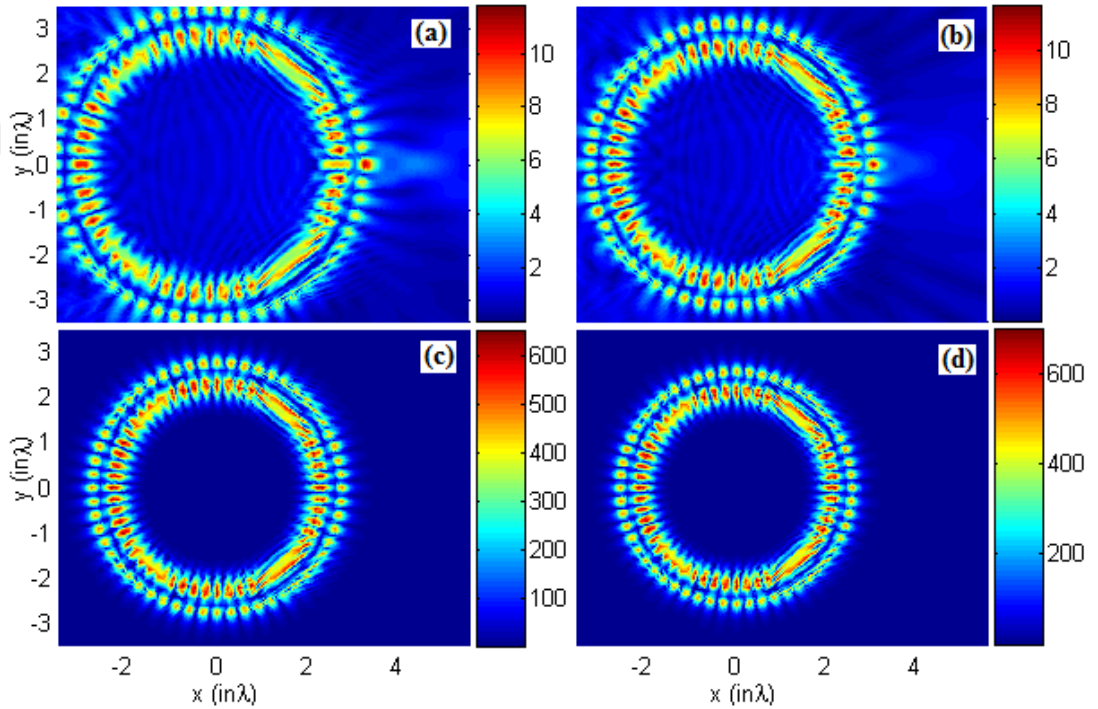


Figure 4. 12: Magnitude of the total scattered-incident field due to plane wave illumination inside and outside the dielectric cylinders of radius and refractive index (a)  $(R, n) = (3.5198\lambda, 1.69)$  , (b)  $(R, n) = (3.2245\lambda, 1.85)$  , (c)  $(R, n) = (2.847491\lambda, 2.1)$  and (d)  $(R, n) = (2.7198007\lambda, 2.2)$  .

In Figure 4.14, we use the numerically captured pairs to extrapolate the relation between  $R$  and  $n$  using cubic spline extrapolation. As can be seen,  $R$  is inversely proportional to the refractive index  $n$  . As mentioned earlier, the difficulty in capturing resonance increases while searching for the corresponding radius as the refractive index increases. That explains the reason to have different amount of numbers after the decimal points for different cases given in Table 4.1.

The points designated with markers are numerically captured. All the points are extrapolated to estimate the resonance mode's trend. One can wonder the limits for the smaller radius cylinder with high refractive index materials vs. larger radius of cylinder with smaller refractive index. Both directions have their own potentials. The easy manufacturing of larger cylinders with flexible low-refractive index material selection makes one side attractive for sensing and lasing applications. On the other hand, smaller cylinders with large refractive index material produce larger free-spectral range and small mode volume. Such properties are of paramount importance in photonics integrated circuits.

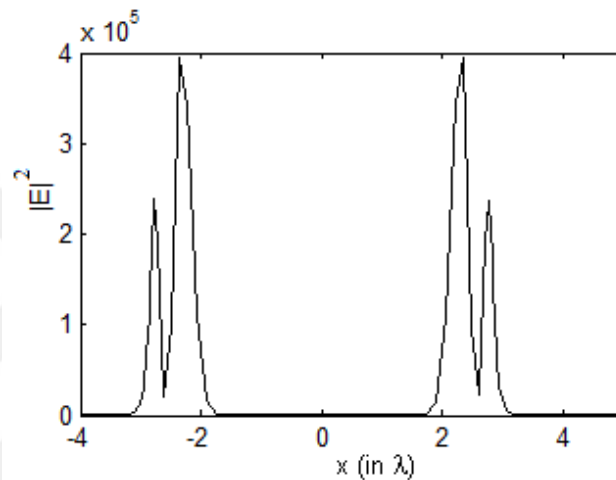


Figure 4. 13: Magnitude of the total field along the x-axis for the case in Figure 4.8

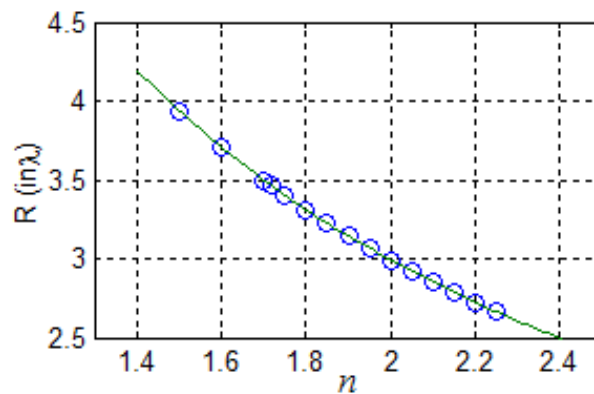


Figure 4. 14: Radius versus refractive index variation for the same type of resonance mode with dielectric micro-cylinder. Data points captured with SEM are plotted with markers. Cubic spline extrapolation of the relation between the physical parameters defining the micro-cylinder where two-ring resonance takes place.

#### 4.4.1 Discussions

It is important to attract the reader's attention to the following formula that governs constructive interference condition for resonance mode:

$$\frac{2\pi}{\lambda} n(2\pi R) = m(2\pi), \quad (4.2)$$

in which  $m$  is an integer number. Although it seems from Figure 4.13 that the multiplication of the radius and the associated refractive index results roughly in a constant, this formula misses some important details about resonance reported in this article such as high field magnitudes and number of rings (type of WGM) when resonance takes place. More importantly, required fine tuning of radius of micro-cylinder can not be obtained by Eq. 4.2. The sensitive dependency of resonance, in order to take place, on the significant digits of either radius or refractive index can never be captured using Eq. 4.2. The significance of the dielectric micro-cylinders as an optical resonator sustaining strong field enhancement is due to the fact that, high-resolution microscopy, near-field imaging, optical lithography, low threshold micro-cavity lasing, and almost single molecule sensing are feasible thanks to the pioneering studies carried out in the field [77], [79].

It is limited to find different types of transparent dielectric materials for the incident light. Meanwhile, manufacturing smaller or larger radius cylinders is only bounded by the capability of manufacturing techniques. Hence, it becomes an important question to see the boundary of the relation between  $R$  and  $n$  for a specific WGM. Even though it becomes impossible to manufacture the micro-cylinders with such a large number of digits after the decimal point, it is conceptually insightful to capture the relation between the parameters of the dielectric micro-cylinder such that same kind of resonance mode is generated.

Finally, in addition the cases reported in Ref. 59, we provide another two cases as shown in Figures 4.15 (a) and 4.15 (b) representing one-ring and three-ring resonators, respectively, where similar  $R$ - $n$  relation takes place. Figure 4.15 (b) is obtained by Mie theory for diversity and convenience. Here, it is important to point that one may need to consider accurate tracking for either radius or refractive index in order to capture resonance. In other words, number of significant digits increases as intensity does. For such tracking, resonance may be missed if the exact parameters are not introduced.

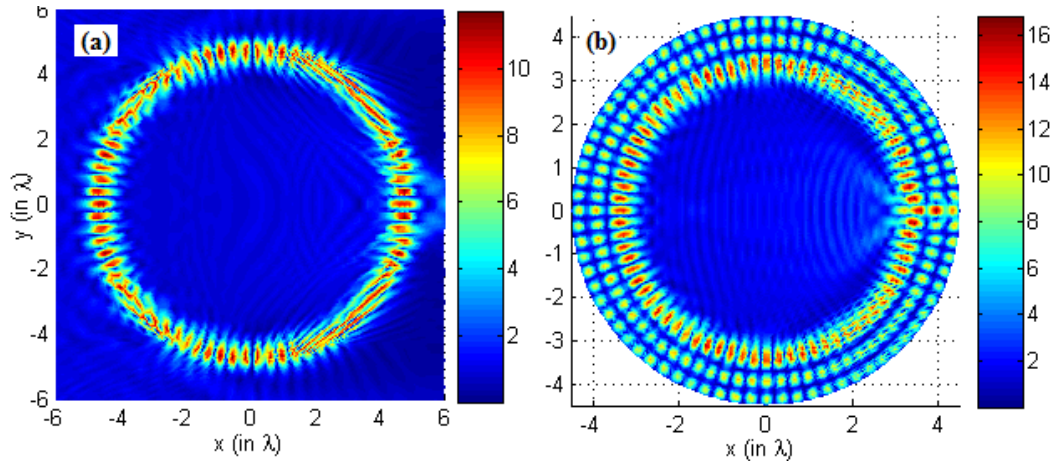


Figure 4. 15: Magnitude of the total field resulting from a plane-wave illuminated dielectric cylinder of (a)  $R = 5.0\lambda$ ,  $n = 1.4$ , and (b)  $R = 4.5\lambda$ ,  $n = 1.905$ .

#### 4.5 Point Source Illumination

Two illuminations scenarios were so far applied; the first is the plane-wave illumination, and the other is Bessel-beam illumination. Under both scenarios, WGMs are captured. It is worthy to check whether WGMs still exist under other types of illumination. For this aim, point source illumination is applied. In this type, the propagation directions of the wave touching the surface of the cylinder are not parallel to each other and that makes it different than plane wave illumination. Figure 4.16 presents the schematic of the photonic structure in which  $d$  represents the distance from the source to the cylinder's closest point, and  $\theta$  stands for the angle between propagation direction and the horizontal axis at the point shown in the figure. In Figure 4.17, the real part of the source field is plotted along x-axis. As can be seen from the figure, the field decays rapidly as it propagates farther from the source location.

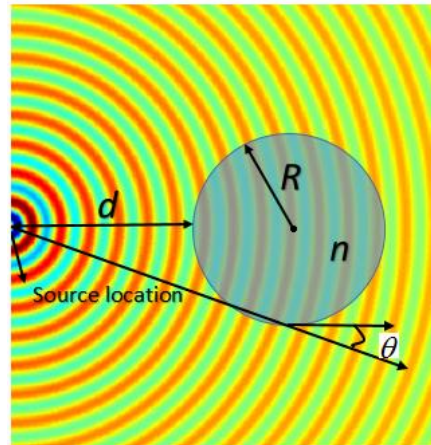


Figure 4. 16: Schematic representation of the photonic structure illuminated by a point source.

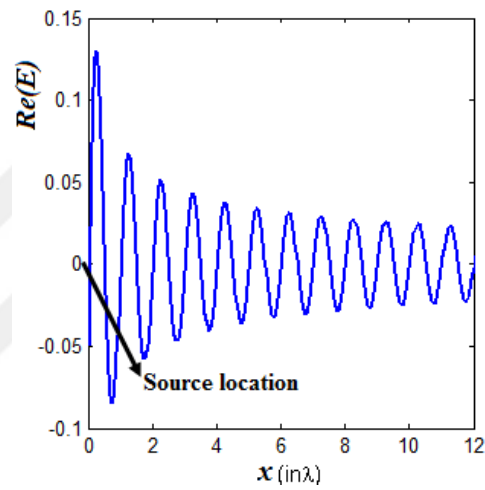


Figure 4. 17: Real part of the electric field generated by a point source.

The photonic nanojets resulted from the point source illumination placed for the physical parameters  $(R, n) = (3\lambda, 1.5)$  are shown in Figure 4.18 when the source is placed at (a)  $d = 15\lambda$ , (b)  $d = 10\lambda$ , (c)  $d = 5\lambda$ , (d)  $d = 3\lambda$ . As can be clearly seen from the figure, as the source gets closer to the micro-cylinder, the photonic jet gets longer and farther from the cylinder's surface.

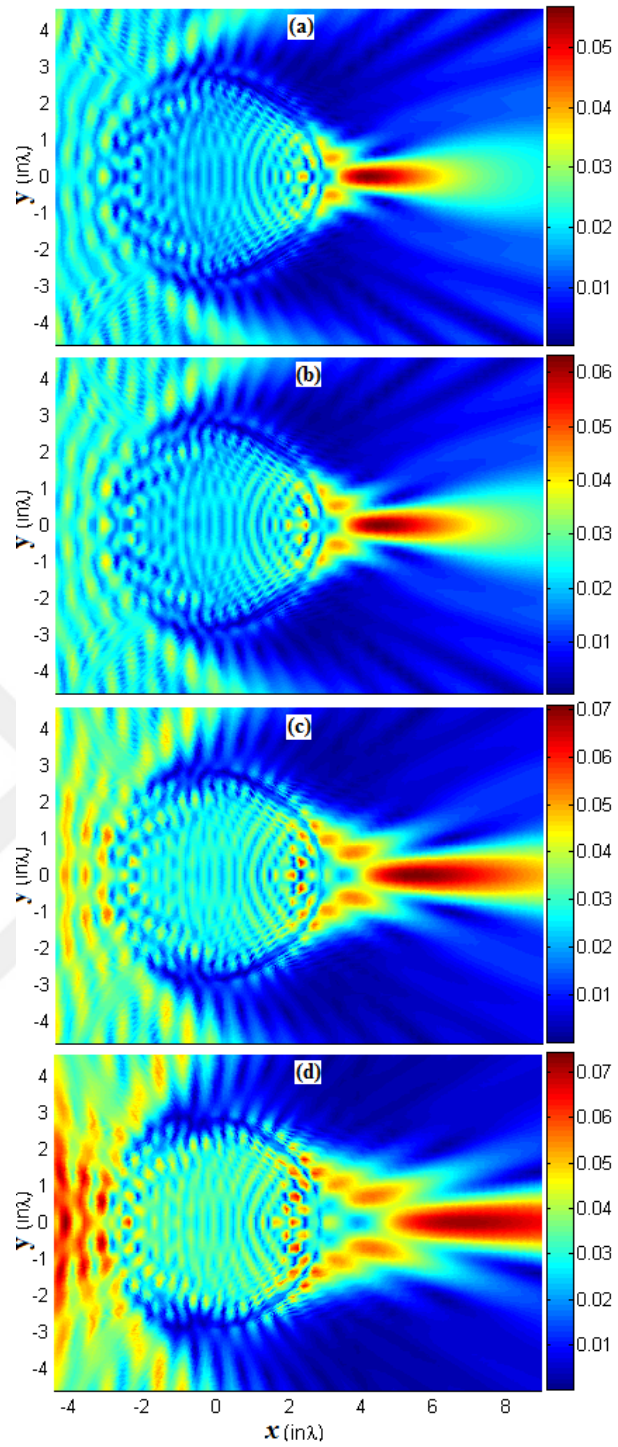


Figure 4. 18: Illumination by a point source placed at different positions for  $R, n = 3\lambda, 1.5$  (a)  $d = 15\lambda$  , (b)  $d = 10\lambda$  , (c)  $d = 5\lambda$  , (d)  $d = 3\lambda$  .

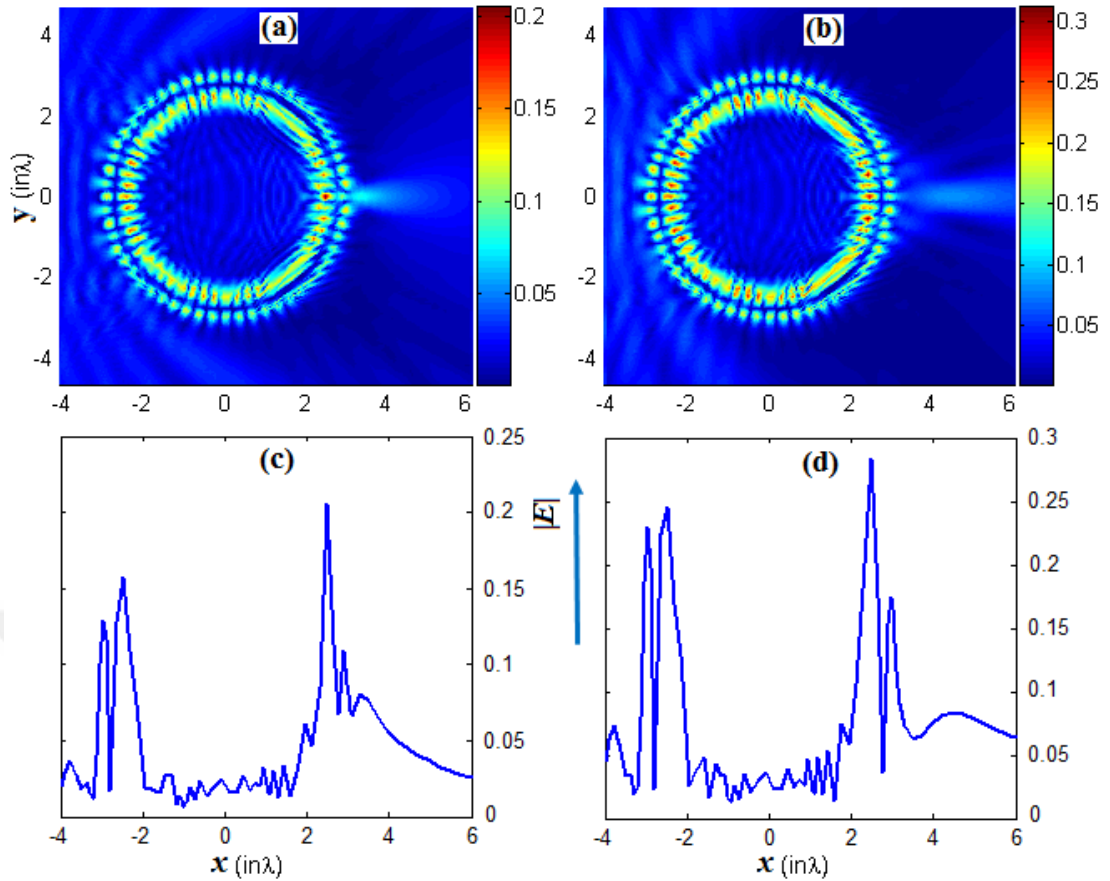


Figure 4. 19: Illumination by a point source placed at different positions for  $R = 3.06267\lambda$ ,  $n = 1.95$  (a)  $d = 10\lambda$ , (b)  $d = 5\lambda$ , the associated field magnitudes along x-axis are shown in (c) and (d), respectively.

It is worthy now to check the existence of WGMs. For this purpose, a case under which WGM takes place is randomly selected from table 4.1. Figure 4.19 shows the field magnitudes resulting from illumination by a point source placed at different positions for  $R = 3.06267\lambda$ ,  $n = 1.95$  when (a)  $d = 10\lambda$ , and (b)  $d = 5\lambda$ , and the associated field magnitudes along x-axis are shown in (c) and (d) for (a) and (b) respectively.

#### 4.6 Conclusions

We have shown that lossless dielectric cylinders with different refractive index and radii illuminated by a linearly polarized plane wave or Bessel beam or a point source produce two separate characteristics, whispering gallery mode vs. photonic nano-jets. The resonance condition yields enhanced field localization inside the micro-cylinder. On the other hand, structural deformations ruins the symmetric electric field formation and strong focusing of light at the shadow side of the cylinder appears close to the

cylinders' surface. Solutions of high accuracy spectral element method and Mie theory agree well with each other except the case that there is a shift for the resonance condition. Understanding the roles of the structural parameters for destroying the resonance condition is critical to develop biosensing applications or observe the effects of the unintended structural deformations.

In conclusion, the capability of confining light at small volume with strong light intensity can pave the way for enhanced light and matter interaction in the resonator's mode volume. Consequently, plenty of important applications covering lasers, sensors, nonlinear optics and quantum QED can get benefit from the successful achievement of compact optical resonators. The relation between  $R$  and  $n$  is numerically extracted for two-ring resonance mode by SEM. Tuning one parameter and finding the other becomes possible with the performed study in the current work. Compact micro-cylinders yield strong field confinement with exceptionally large light intensity. In addition, excitation by Bessel beam illumination and introduction of a different material inside micro-cylinders are considered to investigate the associated resonance behavior.



## **5. CYLINDERS OF DIFFERENT SHAPES AND PROPERTIES**

In this chapter, we study the forward and backward plane wave illuminations of hemicylindrical dielectric particles with different radii and refractive indices. Near field effects providing strong field enhancement and narrow beam width are obtained from hemicylindrical particles, which can be associated with whispering gallery modes (WGMs) and photonic nano-jets. In addition, photonic nanojets resulting from corrugated cylinders (with irregular boundaries) under normally incident plane-wave illumination are studied. Different level of corrugations induced at the boundaries of the dielectric micro-cylinders produce strong light focusing as well as photonic nanojet with unique performance compared to perfectly smooth cylinders. Finally, SEM is utilized due to its accuracy to investigate homogenous and isotropic magneto-dielectric micro-cylinders embedded in air background when illuminated by a unit-intensity plane wave.

### **5.1 Hemi Cylinders**

#### **5.1.1 Introduction**

Two main theories could be implemented to describe light-matter interactions; the first one is Mie theory in which electromagnetic plane wave scattering by a homogeneous and isotropic sphere is widely studied. According to this theory, the electric field is decomposed into inner and outer parts for the inside and outside of sphere and expressed in a vector spherical harmonic expansion to obtain radial and angular dependence of solutions that satisfy Maxwell's equations. Based on Mie theory, optical fields both inside and outside of the low absorbing 3D sphere are subject to the light wave and characterized by focusing spaces called inner and outer focuses of the fields [80]. The second theory is geometric or ray optics, in which light field is approximated to discrete rays to model the propagation of light. Based on ray theory, it is stated that if  $n$  is greater than 2, beam focusing exists inside the dielectric sphere and if  $1 < n < 2$  the focal point is outside of the sphere, where  $n$  stands for the refractive

index of the sphere [81]. What if the focal point is just on the boundary of the sphere, this phenomenon is called “photonic nano-jet” (PNJ) effect, in which case an intense optical jet-like region is generated on the free space shadow side of the surface. It should also be noted that the spherical aberration manifests itself as imperfect focusing at the exit interface of the sphere. In general, the spherical aberrations decrease as the refractive index increases. Using Ray theory, a reduction about 42% was calculated in the (transverse) spherical aberration with a sufficiently high refractive index sphere around  $n \approx 2$  while comparing with that of a sphere having a lower refractive index of  $n \approx 1.5$  [82].

Long before, the spatial distributions of the internal and near external electromagnetic fields have already been investigated when dielectric cylinders and spherical structures having large sizes compared to the incident wavelength of light were plane-wave-illuminated [83], [84]. It was observed that the inner and outer focuses of the field resulting from spherical (cylindrical) particle surface curvature lead to relevant deformations of the incident phase wavefront. Therefore, when a spherical (cylindrical) particle is illuminated from the spherical curvature of the surface, the structure acts as a refractive lens that strongly focuses light within a subwavelength volume (area) [49]. Dielectric microspheres can also be implemented as microcavities providing high Q-factors and a small mode volume, which properties lead to a strong optical feedback within the cavity [85]-[91]. As already known, the spatial configuration of the internal field of the spherical particle is determined by the type of excited resonant mode. The optical field inside the particle is concentrated in a narrow ring layer near its surface, forming a morphology-dependent resonance (MDR) sometimes referred to as a whispering gallery mode [92]. These optical resonances are standing waves created by internal reflections just below the curved surface of the resonator. WGM modes are supported by the geometries of circular symmetry and localized near the surface along the equator of the WGM. Another case of light scattering is non-spherical particles for the implementation of the resonant conditions to excite their resonant modes. The intensity of the internal field, then, becomes much higher than in the absence of the field resonance case, which also has a particular effect on the external field in the region of the PNJ [93]. For spherical particles, it was proved that the effect of resonant PNJ narrowing is due to the field leakages of the resonantly excited WGM. Therefore, depending on the increase in Q-factor corresponding intensities of existing PNJs decrease near the microparticle surface at the distances of

the order of the wavelength in a medium [94], [95]. It was also investigated that for non-spherical resonators, reduction in PNJ effect may still exist due to WGM modes [96].

Various practical applications such as high-density data storage and high-resolution optical imaging may require the creation of PNJs or streams with different geometries. To date, the formation of PNJs and their applications have already been developed using dielectric particles of different three-dimensional (3D) forms in non-resonant modes and cylindrical and spherical form in resonant (WGM) modes [85]-[91]. As an example, the numerical investigations of a PNJ formation was reported for the hemispherical particles illuminated from the curvilinear surface in transmitting non-resonant mode [97]. Nevertheless, to the best of authors' knowledge, hemicylindrical particles on transmission mode were investigated only in one illumination direction (from the spherical surface under the normal illumination), but not in the backward illumination (from the flat surface). Moreover, the WGM or other resonant effects in hemicylindrical particles have not investigated yet. The existence of PNJ effect for hemicylindrical dielectric particles was not reported previously, too.

### **5.1.2 SEM Results**

Directional emission of light from the hemicylindrical microcavity is presented, and this effect is attributed to the PNJs generated in the mesoscale hemicylinder. Second, the influence of forward and backward excitations to the PNJ properties is discussed for hemicylindrical particles. Moreover, it was noticed from numerical calculations that even though WGM resonators usually show higher quality factor (Q-factor) which considerably weakens the PNJ effect, hemicylindrical aided PNJs are influenced relatively small in WGM regime. It is known that the effects of PNJs cannot be predicted on the basis of geometrical optics or scalar diffraction theory [85]-[91]. Therefore, it is essential to study the propagation of electromagnetic waves through such elements by using Maxwell's equations. In order to evaluate the PNJ performance, the numerical results of this study are carried out using the spectral element method (SEM). The reason for choosing SEM for the PNJ evaluation is due to its lower computational cost and better accuracy when compared with finite difference method or finite element method [52]-[58].

The schematic representation of the studied geometry in the x-y plane is shown in Figure 5.1. The hemicylinder has a radius of  $R$  and refractive index of  $n$  embedded in an air medium. The computational domain is terminated by perfectly matched layers (PML) as an absorbing boundary condition. We follow two types of plane wave illumination throughout the SEM calculations due to the asymmetric nature of the proposed hemicylinder: propagation direction coinciding with the positive x-axis is denoted as forward excitation, and propagation coinciding with the negative x-axis is referred as backward excitation.

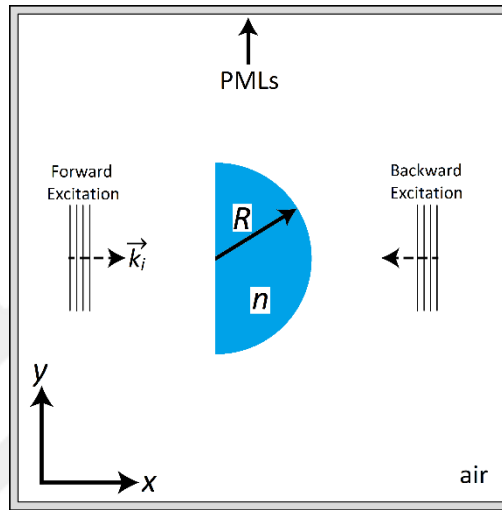


Figure 5. 1: The schematic of the hemicylindrical particle and definition of forward and backward excitation.

In order to make a comparison with the results reported in the third chapter, the hemicylindrical structures with different geometries  $(R,n)=(3.5\lambda,1.7)$  and  $(R,n)=(2.93\lambda,2.0)$  were exposed to backward illumination. Corresponding total scattered fields with their magnitudes are shown in Figure 5.2(a) and 5.2(b), respectively. In both combinations of parameters, a typical PNJ is formed in the shadow side of the hemicylinder. The parameters  $(R,n)=(3.5\lambda,1.7)$  whose associated field solution is presented in Figure 5.2(a) are chosen intentionally to compare the results with that obtained in the case of a perfect cylinder. In the third chapter, there are two modes of resonance where a regular cylinder is illuminated by a perpendicularly incident plane wave. One of these modes occurs at  $(R,n)=(3.5\lambda,1.7)$ . However, the resonance does not take place in a hemicylindrical object, see Figure 5.2(a). The same parameters considered in Figure 5.2(b) will be studied again later in this letter under forward excitation scheme. It should also be noted that a hot spot was observed at the center of the curvilinear surface of the particle as in Figure 5.2(b),

which can be attributed to the resonant wave configurations inside the hemicylinder under the selected parameters of the particle. In addition, while the associated FWHMs are calculated to be the same ( $\text{FWHM}=0.44\lambda$ ) for the two cases shown in Figure 5.2, corresponding maximum intensity (square of the magnitude of the total field) of the case  $(R,n)=(3.5\lambda,1.7)$  is 1.31 times larger than the second case of  $(R,n)=(2.93\lambda,2.0)$ . Compared to that obtained in full cylinders as in chapter 3, PNJ effect still exists with hemicylindrical structure, see Figure 5.2. However, the position of the light localization is slightly away from the flat end surface, see the field cross-sections in Figure 5.3. In addition, as can be observed from the figure, the decay length of a PNJ obtained from a hemicylindrical structure decreases as refractive index increases at a fixed radius and the focal point reaches near to the structure.

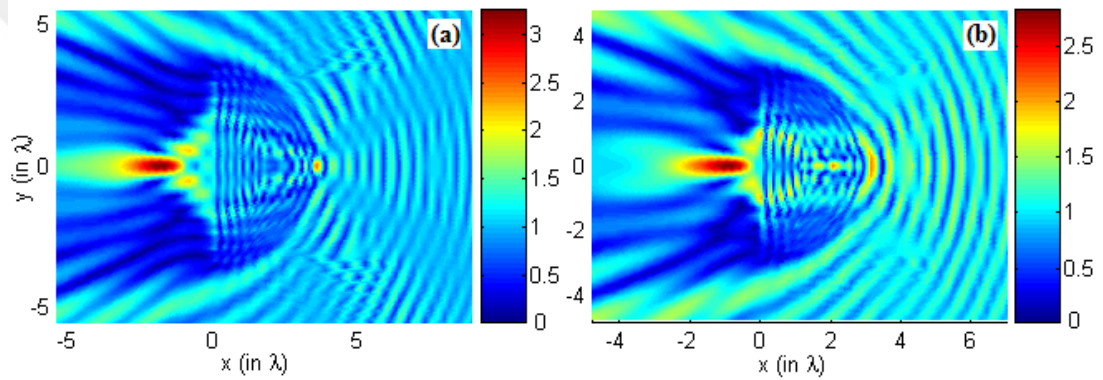


Figure 5. 2: The magnitude of the total scattered field due to plane wave illumination (backward excitation) inside and outside the hemicylinder with the radius and the refractive index values (a)  $(R,n)=(3.5\lambda,1.7)$ , (b)  $(R,n)=(2.93\lambda,2.0)$ .

In addition to backward illumination, we present the field distributions of the forward illumination to realize optical differences between backward and forward excitation schemes. Figure 5.4 represents corresponding magnitude of the total scattered fields for forward plane wave illumination of the hemicylinder having radii and refractive indices (a)  $(R,n)=(1.5\lambda,1.65)$ , (b)  $(R,n)=(1.5\lambda,1.55)$ , (c)  $(R,n)=(2.93\lambda,2.0)$  and (d)  $(R,n)=(2.96\lambda,2.0)$ . Corresponding FWHMs are calculated to be  $0.512\lambda$ ,  $0.498\lambda$ ,  $0.585\lambda$  and  $0.575\lambda$ , respectively. In contrast with backward illumination, resonant WGMs are excited by forward illumination of the hemicylinder with the associated azimuthal mode number,  $m=14$  and radial mode number,  $l=1$  in Figure 5.4(a) and 5.4(b),  $(m,l)=(32,1)$  in Figure 5.4(c),  $(m,l)=(32,2)$  in Figure 5.4(d). The magnitude of the total scattered field is also calculated for forward plane wave illumination of the hemicylinder having  $n=2.0$  and radii of  $2.93\lambda$  and  $2.96\lambda$ . The cross-section of the

calculated fields along the line of symmetry are taken for varying refractive indices and superimposed in Figure 5.5 to better observe the resonance peaks inside the structure. It can be clearly seen from the figure that one peak is obtained in the case of  $R=2.93\lambda$  whereas in the case of  $R=2.96\lambda$  two peaks exist inside the structure, which implies corresponding radial number equals  $l=2$ .

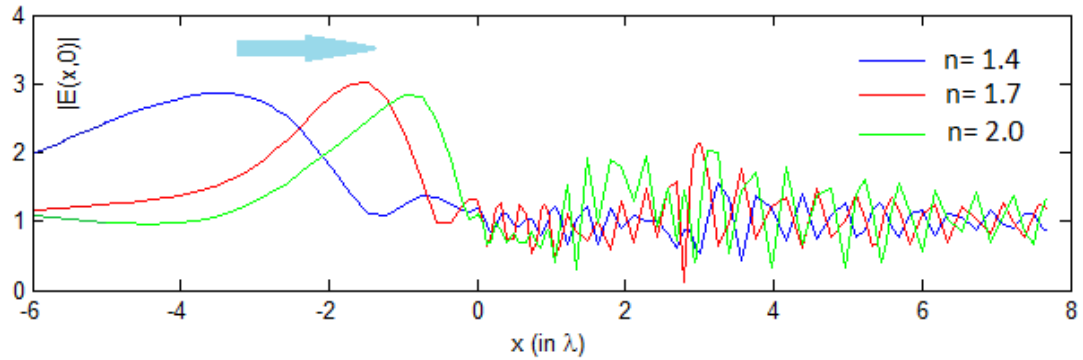


Figure 5. 3: The magnitude of the total scattered-incident field due to plane wave illumination (back excitation) along the line of symmetry for  $R=2.93\lambda$  and different refractive indices.

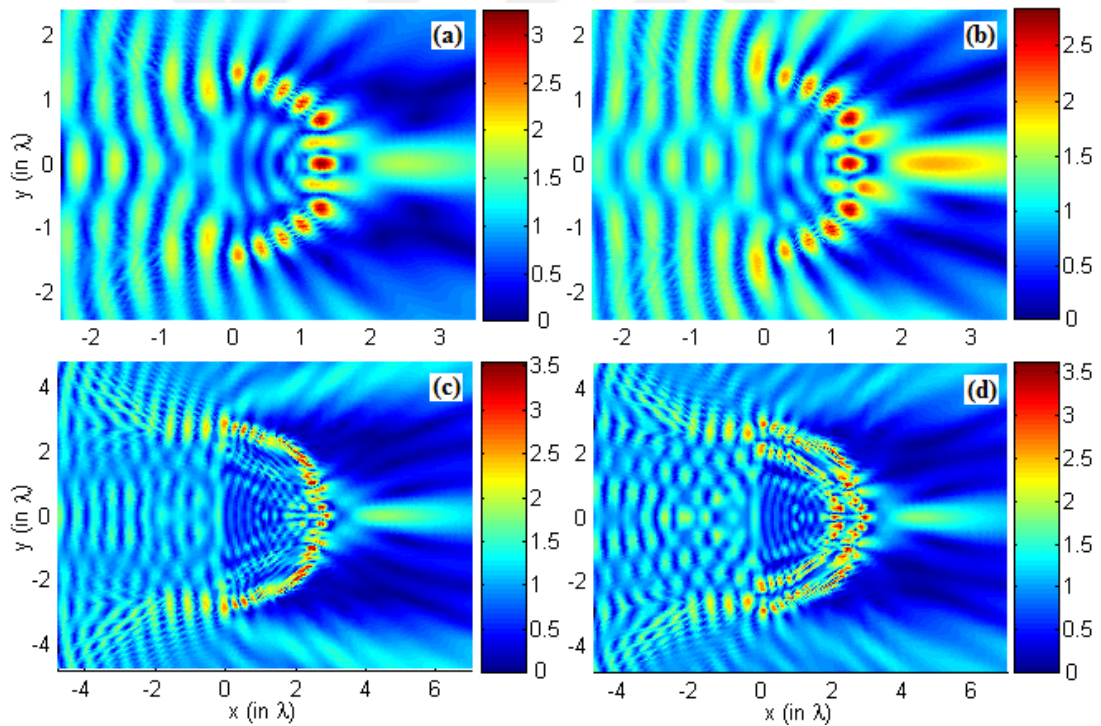


Figure 5. 4: The magnitude of the total scattered field for forward plane wave illumination of the hemicylinder with the radius and refractive index of (a)  $(R,n)=(1.5\lambda,1.65)$ , (b)  $(R,n)=(1.5\lambda,1.55)$ , (c)  $(R,n)=(2.93\lambda,2.0)$ , and (d)  $(R,n)=(2.96\lambda,2.0)$ .

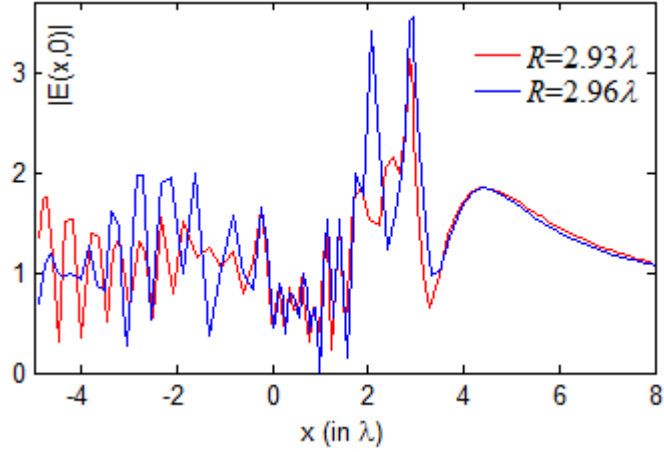


Figure 5. 5: The magnitude of the total scattered field in the case of forward excitation along the line of symmetry while setting  $n=2.0$  and  $R=\{2.93\lambda, 2.96\lambda\}$ .

Figure 5.6 is prepared to investigate the dependence of WGM resonant modes on the refractive index of the particle. For that reason, the hemicylinder with the radius and the refractive index  $(R,n)=(2.96\lambda, 1.46)$  is forward-illuminated by a plane-wave and the corresponding azimuthal mode number  $m=28$  and radial mode number  $l=1$  is obtained, which were  $(m,l)=(32,2)$  in the case of  $(R,n)=(2.96\lambda, 2.0)$ . The associated FWHM of the case  $(R,n)=(2.96\lambda, 1.46)$  is calculated as  $0.668\lambda$ , which was  $0.575\lambda$  in the case of  $(R,n)=(2.96\lambda, 2.0)$ . Investigating the results shown in Figures 5.4 and 5.6, one can claim that the WGM properties (mode number) existing inside the hemicylinder directly depends on the permittivity and radius of the particle. Furthermore, excitation of the resonances with a low Q-factor does not influence the PNJ performance. The decay length, as well as the FWHM of the PNJ, remain the same as in the non-resonant case. So if the FWHM of the PNJ changes slowly we have a small Q-factor of the hemicylindrical resonant. Such less relevance of PNJ effect on the WGM resonances could be interpreted like the following: Under the resonant excitation, the optical field inside the particle changes its spatial configuration taking the shape characteristic for the field of the unit (separated) eigenmode. In so doing, the optical field intensity increases outside the particle near the surface, at the expense of “outflow” of this excited mode through a transparent interface. It is also noticed from the field distributions demonstrated in Figures 5.4 and 5.6 that narrowing the beam spot of PNJ as reported in [94] exists only near the particle’s surface at distances less than  $\lambda/3$  and then, the PNJ broadens to non-resonant sizes. A small change in the radius

and refractive index of particles lifts the degeneracy of WGM modes, which provides WGM waves for passing in close range of the standing waves.

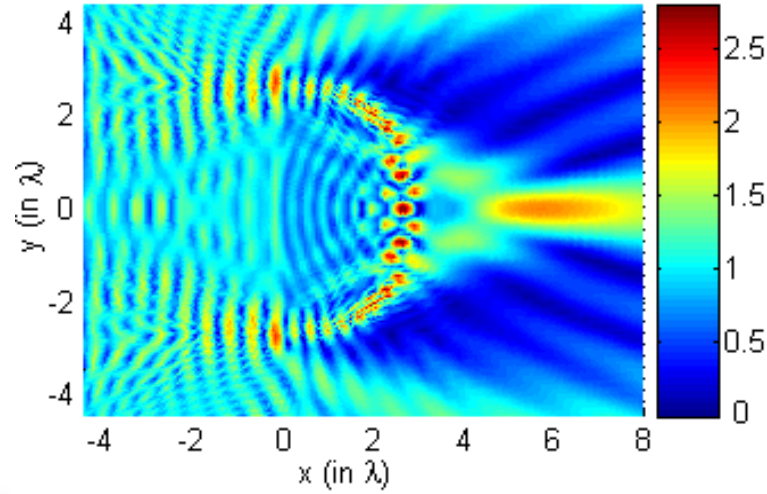


Figure 5. 6: The magnitude of the total scattered field for forward plane wave illumination of the hemicylinder with the radius and refractive index of  $(R,n)=(2.96\lambda,1.46)$ .

## 5.2 Photonic Nanojet Under The Deformation Of Circular Boundary

In the current study, some attention is also paid to the plane-wave illuminated, corrugated, dielectric micro-cylinders. Corrugation of the sidewall surface naturally occurs as a result of imperfect nature of fabrication, however in our work we consider a specific type of corrugation which possesses an azimuthal symmetry. There are many examples of photonic microstructures with such geometrical properties. They include differently profilated fibers, see Ref. [98], or fibers with hexagonal cross-section, see Ref. [99], which can be obtained by various technologies. Another example is represented by the hexagonally-shaped high-index nanowires, as illustrated in Refs. [100], [101]. To understand the role of surface corrugation in the focusing properties, in this work, we selected a relatively simple case with the surface corrugation described by two spatial harmonics.

Cylinders with uniform boundaries are subdivided into sufficiently large number of elements so that accuracy of SEM is not affected, and all elements have same number of nodes as continuous Galerkin method is employed. In addition to regular dielectric cylinders, we intentionally modulate the surface of the cylinder and designate that structure as corrugated cylinder. For a regular structure, there is constant radius,  $R_0$



and refractive index,  $n$ . On the other hand, corrugated cylinder has radius expressed in polar coordinate as:

$$R = R_0 \left| 1 + \frac{\beta}{R_0} \sin(m_1 \varphi) \sin(m_2 \varphi) \right| \quad (5.1)$$

where,  $R_0$  is average radius,  $\beta/R_0$  is the ratio of deformation of boundary to the average radius,  $m_1$  and  $m_2$  are the two periods of the variations of the corrugated boundary (in this work, they are chosen to be integer numbers) with  $\varphi$  being the azimuth angle. Note that when either  $m_1 = 0$  or  $m_2 = 0$ , Eq. 5.1 turns out to be cylinder with constant radius,  $R_0$ .

In Figure 5.7, the GLL grids ( $N \times N = 9 \times 9$ ) are shown in the 12 elements for a regular cylinder in Figure 5.7 (a) of constant radius  $R_0 = 4\lambda$ , and for a corrugated cylinder of  $R_0 = 4\lambda$ ,  $m_1 = 6$ ,  $m_2 = 4$ , and  $\beta = 0.3$  in Figure 5.7 (b). It is possible to discretize the cylinder into higher number of elements, in this case the SEM can be viewed as the h-version of FEM. However, we instead increased the order of polynomial (p-version of FEM) and reduced the number of elements in such a way that the conditional number of Jacobi matrix is increased. It is noteworthy to point that this resolution ( $N \times N = 9 \times 9$ ) is chosen in Figure 5.7 for the purpose of clear demonstration only. However, in order to avoid numerical errors arising from low resolution, the resolution  $N \times N = 20 \times 20$  is applied in this work for each element.

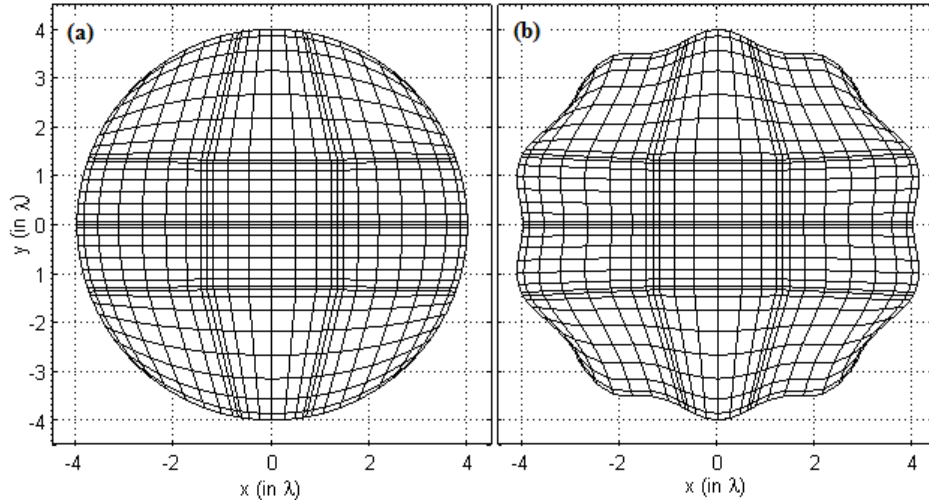


Figure 5. 7: The GLL grids ( $N \times N = 9 \times 9$ ) in the 12 elements for a regular cylinder (a) of radius  $R_0 = 4\lambda$ , and (b) for a corrugated cylinder of  $R_0 = 4\lambda$ ,  $m_1 = 6$ ,  $m_2 = 4$ , and  $\beta = 0.3$

### 5.2.1 Results of SEM

The variation in the radius of a corrugated cylinder is defined in the current study as:

$$\Delta R \% = \frac{R_{\max} - R_{\min}}{R_0} \times 100\% \quad (5.2)$$

Table 5.1 shows the percentage variations of radius change which is essentially determined by  $\beta$  coefficient for four different shapes of corrugated micro-cylinders. The corresponding geometrical plots of cylinders are shown in Figure 5.8. Whereas the associated distributions of the total field obtained by SEM are shown in Figure 5.9.

Table 5. 1: Variations of radius in terms of incident wavelength

$(m_1, m_2, \beta)$	$\Delta R\%$	$\Delta R$
(10, 2, 0.2)	8.075	$0.363 \lambda$
(10, 2, 0.4)	16.150	$0.727 \lambda$
(10, 4, 0.2)	8.504	$0.382 \lambda$
(10, 4, 0.4)	17.029	$0.766 \lambda$

There are important remarks that can be drawn from Figure 5.9. Even though there is large deformation on the surface of the dielectric cylinder as shown in Figure 5.9 (a), the strong light focusing at the back region of the structure with nanojet type field distribution appears. This observation informs us that one does not need very smooth and corrugation free cylinder's surface in order to obtain light focusing. When we keep periodicity parameters constant but increase modulation depth, light gets focused again as indicated in Figure 5.9 (b). The accompanied side lobes share some portion of the energy of the central beam.

Figure 5.9 (c) and 5.9 (d) are prepared to make comparison in terms of the role of periodicity variables. These parameters affect the light focusing behavior and less nanojet type of field distribution occur. Moving from the case Figure 5.9 (a) to 5.9 (d), nanojet type of focusing characteristic disappears but strong light focusing with short field of depth occurs.

The length of nanojet gets longer because of boundaries shape. That observation triggers the idea that by manipulating the boundary of the cylinder one can get enhanced photonic nanojet behaviour. This is indeed an exciting future research direction. By incorporating an optimization algorithm into the searching parameter space for improved results there will be optimum case yielding superior photonic nanojet type field distribution.

Table 5. 2: Variations of radius in terms of incident wavelength

$(m_1, m_2, \beta)$	$\Delta R\%$	$\Delta R$
(10, 2, 0.111)	8.067	$0.202 \lambda$
(10, 2, 0.222)	16.134	$0.403 \lambda$
(10, 4, 0.111)	8.506	$0.213 \lambda$
(10, 4, 0.222)	17.012	$0.425 \lambda$

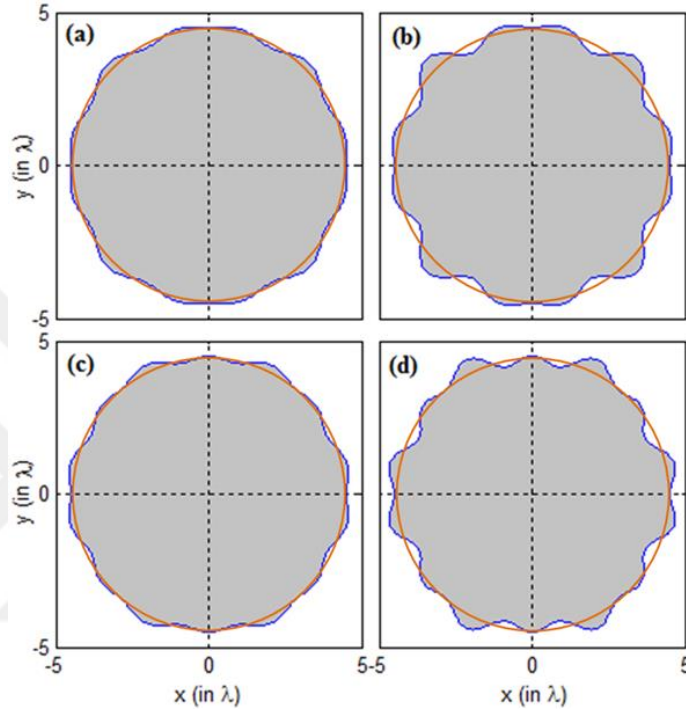


Figure 5. 8: The dielectric corrugated cylinder of average radius  $R_0 = 4.5 \lambda$  plotted at (a)  $m_1 = 10, m_2 = 2$ , and  $\beta = 0.2$ , (b)  $m_1 = 10, m_2 = 2$ , and  $\beta = 0.4$ , (c)  $m_1 = 10, m_2 = 4$ , and  $\beta = 0.2$ , and (d)  $m_1 = 10, m_2 = 4$ , and  $\beta = 0.4$ . Perfect cylinders with  $R_0 = 4.5 \lambda$  are superimposed in each case for easy inspection of the irregular boundaries with respect to ideal case.

One of the critical question to be asked here is what would be the performance of dielectric cylinder if the radius is reduced. We have induced same percentage corrugations shown in Figure 5.9 as presented in Table 5.2. Figure 5.10 shows the field magnitude inside and outside the dielectric corrugated cylinder of refractive index  $n = 1.7$  and average radius  $R_0 = 2.5 \lambda$  due to an illuminating plane wave as computed by SEM for (a) a perfect cylinder, (b)  $m_1 = 10, m_2 = 2, \beta = 0.111$ , (c)  $m_1 = 10, m_2 = 2, \beta = 0.222$ , (d)  $m_1 = 10, m_2 = 4, \beta = 0.111$ , and (e)  $m_1 = 10, m_2 = 4, \beta = 0.222$ .

In order to have focusing of light, we increase the refractive index from 1.50 to 1.70 in this case. When we inspect all four cases comparing with regular cylinder in Figure

5.10 (a), we observe that 8% corrugation does not terminate light focusing property. Doubling corrugation percentage still yields lensing effect with such a small dielectric cylinder.

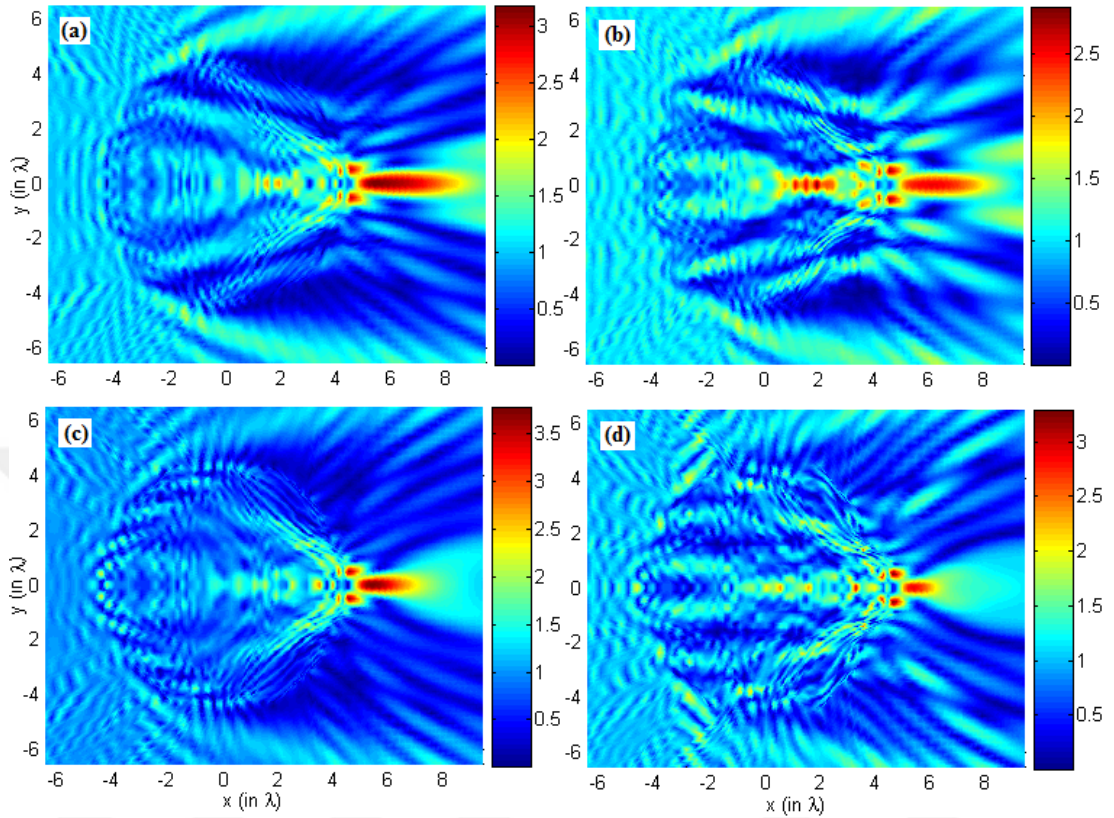


Figure 5. 9: Field magnitude inside and outside the dielectric corrugated cylinder of refractive index  $n = 1.5$  and average radius  $R_0 = 4.5\lambda$  due to a normally incident plane-wave as computed by SEM for the four cases shown in Figure 5.8.

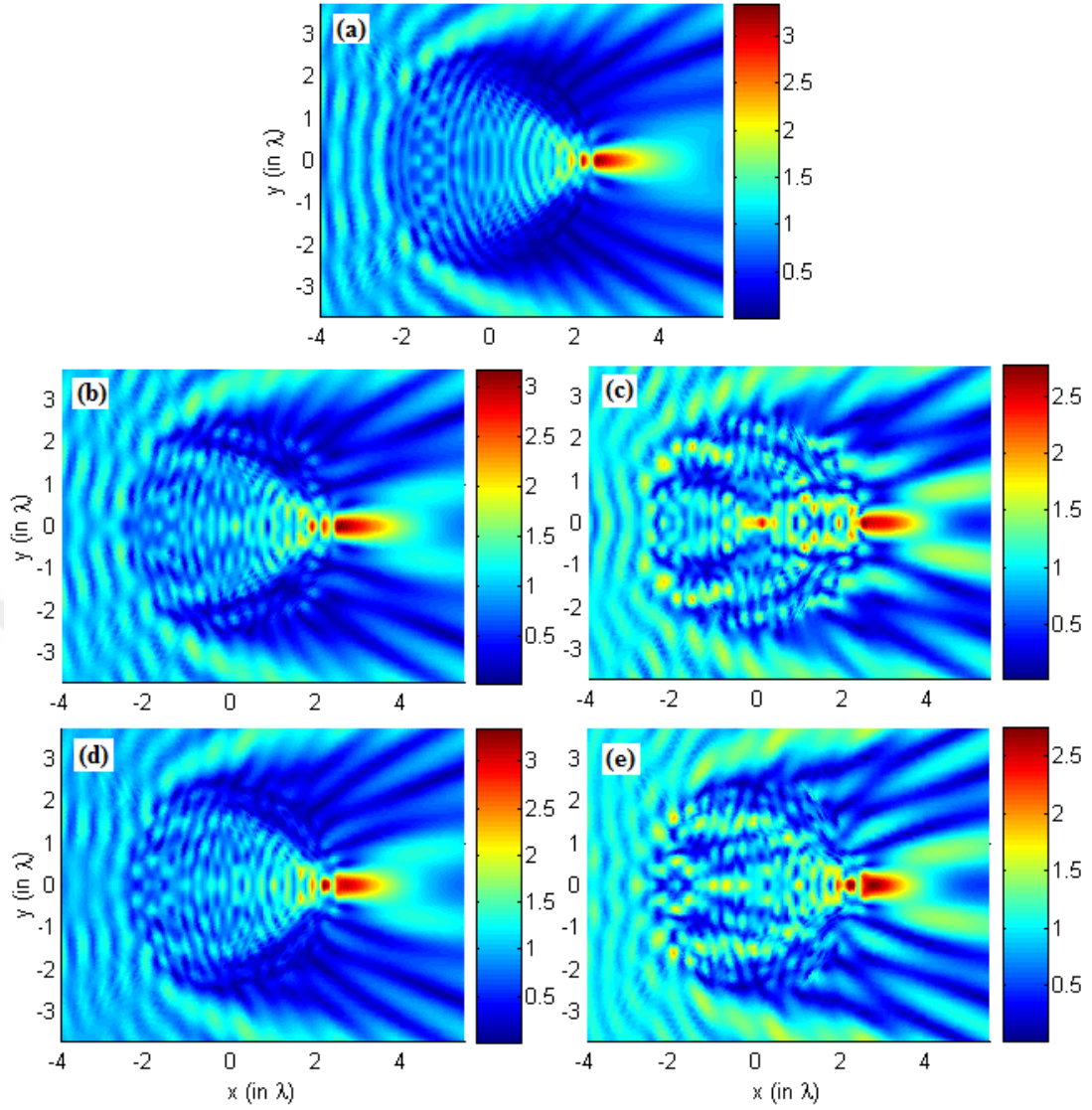


Figure 5. 10: Field magnitude inside and outside the dielectric corrugated cylinder of refractive index  $n = 1.7$  and average radius  $R_0 = 2.5\lambda$  due to a normally incident plane-wave as computed by SEM for (a) a circular cylinder, (b)  $m_1 = 10$ ,  $m_2 = 2$ , and  $\beta = 0.111$ , (c)  $m_1 = 10$ ,  $m_2 = 2$ , and  $\beta = 0.222$ , (d)  $m_1 = 10$ ,  $m_2 = 4$ , and  $\beta = 0.111$ , and (e)  $m_1 = 10$ ,  $m_2 = 4$ , and  $\beta = 0.222$ .

### 5.2.2 Resonance

In order to demonstrate the accuracy of the spectral element method (SEM), Ref. [59] has reported some results that differ from light focusing phenomenon in photonic jet. In other words, when a lossless dielectric micro-cylinder is illuminated by a perpendicularly incident plane wave, instead of obtaining a photonic nanojet, resonance behavior is realized inside the micro-cylinder. There are various designs of cavities with large Q-factors that emerged in the photonic applications [85]. Optical

resonators such as spheres, cylinders, and disks form essential parts of passive and active devices [102], [103]. While the former includes add/drop filters, tunable filters, and chemical /pressure sensors, nonlinear oscillators, low-threshold lasers, and optical modulator/switches are among the active device applications [103]. Special attention has been given to light when it is focused with an isolated single dielectric cylinder due to unique subwavelength field focusing capability of such structures [49], [104]. In Ref. [104], it is demonstrated that whispering gallery mode characteristic of resonance behavior is strongly dependent on the refractive index and radius of regular cylinders. That is, detuning of the either parameter deteriorates the resonance action and creates yet photonic nanojets. However, we interestingly find that this strong dependency doesn't take place in the case of corrugated micro-cylinders.

A corrugated micro-cylinder of  $R_0 = 2.5\lambda$  with  $m_1 = 16$ ,  $m_2 = 4$ , and  $\beta = 0.18$  is considered and the associated geometrical plot is shown in Figure 5.11(a). The corresponding total field distribution at a refractive index of  $n = 1.452$  is introduced in Figure 5.11(b) in 3D view. As it can be clearly seen from the figure, whispering gallery mode (WGM) with mode number 19 takes place of intensity ( $E_z E_z^*$ ) about 8 times the intensity of the incident plane wave.

In the case of regular cylinders, the authors in Ref. [77] showed that if a change of 0.0005 is introduced in either  $R$  or  $n$ , WGM can be significantly reduced. However, the situation is different in the case of corrugated cylinders. To support the latter argument, the electric field distribution inside and outside the dielectric corrugated cylinder whose parameters are:  $R_0 = 2.5\lambda$ ,  $m_1 = 16$ , and  $m_2 = 4$  is plotted at  $n = 1.452$ ,  $\beta = 0.12$  (Fig. 9(a)),  $n = 1.452$ ,  $\beta = 0.18$  (Fig. 9(b))  $n = 1.452$ ,  $\beta = 0.22$  (Figure 5.12(c)), and  $n = 1.455$ ,  $\beta = 0.18$  (Figure 5.12(d)). It is important to note that although much larger variations either in refractive index or in the tortuosity is introduced, WGM can be still visualized.

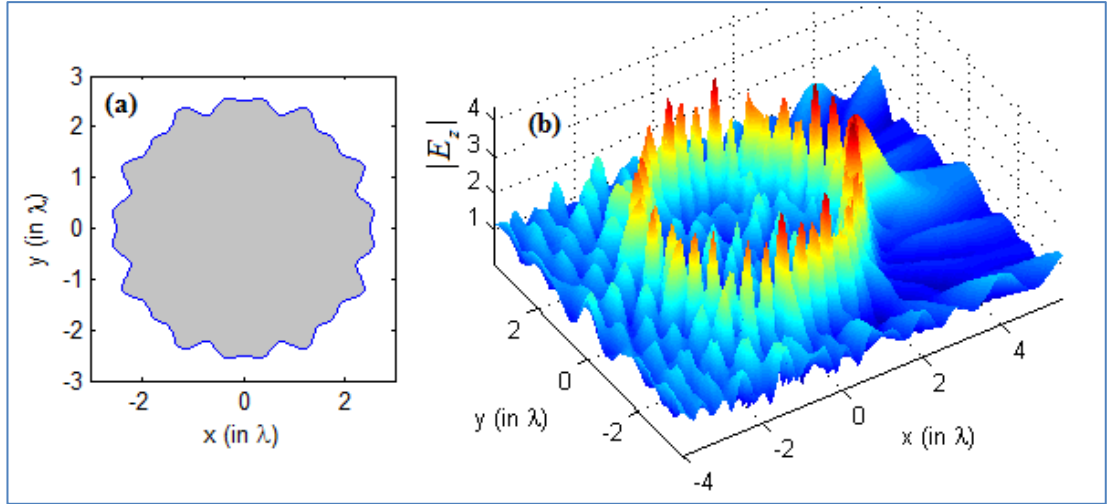


Figure 5. 11: The dielectric corrugated cylinder of average radius  $R_0 = 2.5 \lambda$  (a) plotted at  $m_1 = 16$ ,  $m_2 = 4$ , and  $\beta = 0.18$ , and (b) the SEM solution ( $|E_z|$ ) at  $n = 1.452$  due to a normally incident plane-wave propagating in positive x direction.

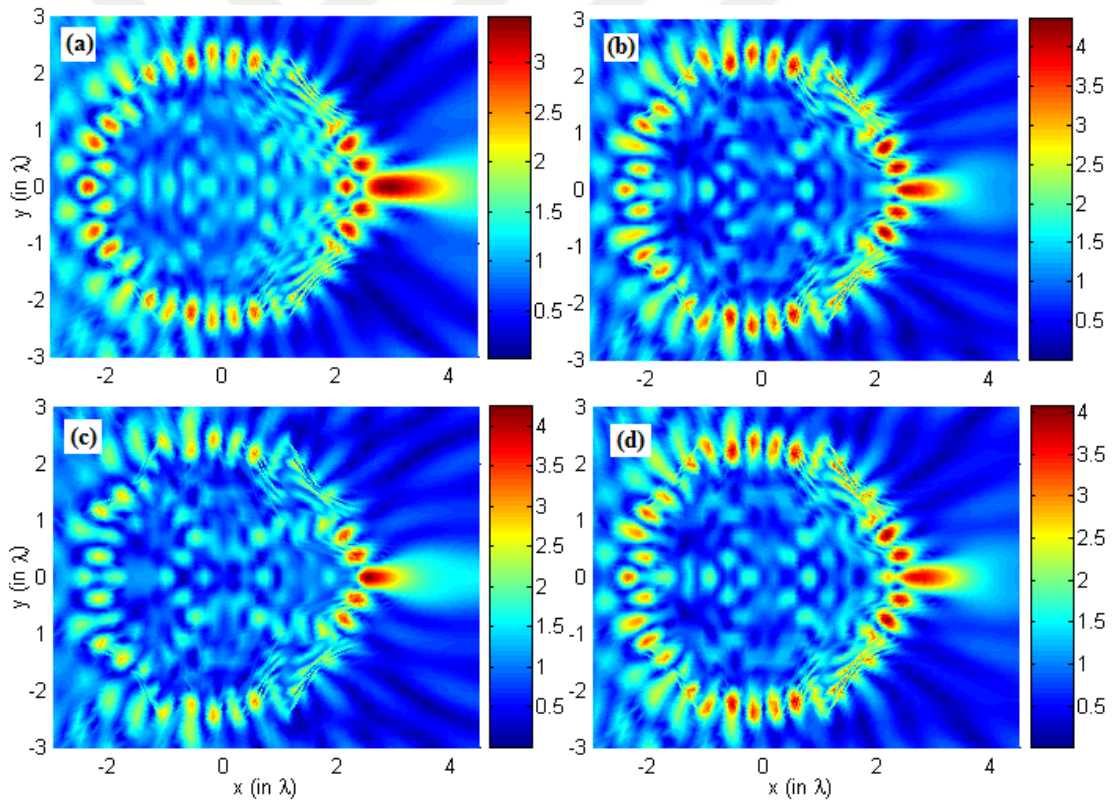


Figure 5. 12: Field magnitude inside and outside the dielectric corrugated cylinder of average radius  $R_0 = 2.5 \lambda$ ,  $m_1 = 16$ ,  $m_2 = 4$  due to a normally incident plane-wave as computed by SEM for (a)  $n = 1.452$ ,  $\beta = 0.12$ , (b)  $n = 1.452$ ,  $\beta = 0.18$ , (c)  $n = 1.452$ ,  $\beta = 0.22$ , and (d)  $n = 1.455$ ,  $\beta = 0.18$ .

### 5.3 Magnetic Cylinders

Many theoretical and experimental researches have been devoted to the study of magnetic properties of thin films [105-106], [113-117]. This is due to the unusual electromagnetic scattering features of magneto-dielectric small particles. However, such behavior is difficult to achieve due to the non-magnetic property of natural optical materials. Hopefully, some recent researches presented unambiguous experimental evidence that a single low-loss dielectric sphere for moderate refractive index is found to radiate fields identical to those from equal amplitude crossed electric and magnetic dipoles, and interestingly similar to fields obtained due to magneto-dielectric spheres [117].

Loss-free compact non-magnetic, dielectric micro-cylinders acting as optical resonators have been intensively investigated over the last few decades. In this section, SEM is utilized due to its accuracy to investigate homogenous and isotropic magneto-dielectric micro-cylinders embedded in air background when illuminated by a unit-intensity plane wave. In addition to the extremely large field enhancement reported in this work, details of scattered field is also presented at unit refractive index ( $n=1$ ) for the first time to the best of our knowledge. Finally, field distribution due to a magneto-dielectric square object is introduced. In cases when  $n=1$ , we confirm on the fact that very negligible on-axis backscattering is obtained.

#### 5.3.1 Results of scattered field

The schematic view of the photonic medium under investigation is demonstrated in Figure 2.1 in which the magnetic property is considered. A typical solution to the electric field is presented in Figure 5.13 for an incident plane wave of one unit in magnitude excites a magneto-dielectric cylindrical object of radius  $R = 3\lambda$  with  $\epsilon_r = \mu_r = 1.5$  (recall that the refractive index is  $n = \sqrt{\epsilon_r \mu_r}$ , then  $n = 1.5$  in this case). As can be clearly seen from the figure, the cylinder scatters the field in such a way that photonic nanojet behavior which is expected from a perfect dielectric cylinder is almost absent.



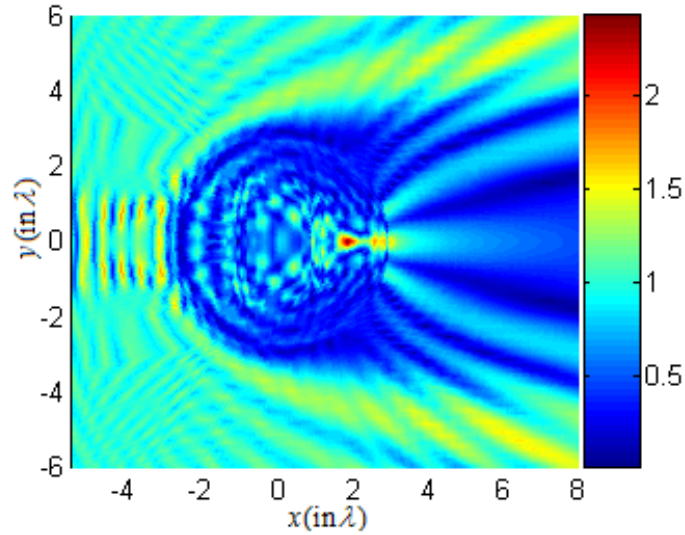


Figure 5.13: SEM solution to the incident-scattered field ( $E_z^{inc} + E_z^s$ ) inside and outside of a magnetodielectric cylinder of radius  $R = 3\lambda$  and with  $\varepsilon_r = \mu_r = 1.5$

Kerker et. al [105] investigated a number of unusual electromagnetic scattering effects resulting from a relatively small magnetic sphere illuminated by a plane wave. Some of these special cases were found interesting according to the authors, mainly the case in the small-particle limit of  $n=1$ , i.e.,  $\varepsilon_r = 1 / \mu_r$ . In addition, Kerker and his colleagues predicted that a small particle with diameter much smaller than the wavelength of operation may have a zero forward scattering, but a significantly larger (even orders of magnitude) scattering in all other directions when  $\varepsilon_r = (4 - \mu_r) / (2\mu_r + 1)$  condition is satisfied. Even though the quasi-static limit analysis predicts this case, it has been shown that this condition is still valid for magneto-dielectric spheres of moderate size [106]. In fact, the interest in this issue has been revisited in both theoretical studies [107], [108] and experimental ones [109]-[111].

By using SEM formulation, we have numerically simulated this case ( $\varepsilon_r = (4 - \mu_r) / (2\mu_r + 1)$ ) but with a relatively larger diameter ( $R = 3\lambda$ ) at  $\mu_r = 3$  and presented the solution in Figure 5.14 (Real part of the field) and Figure 5.15 (Field magnitude) which provides an inside about the field intensity.

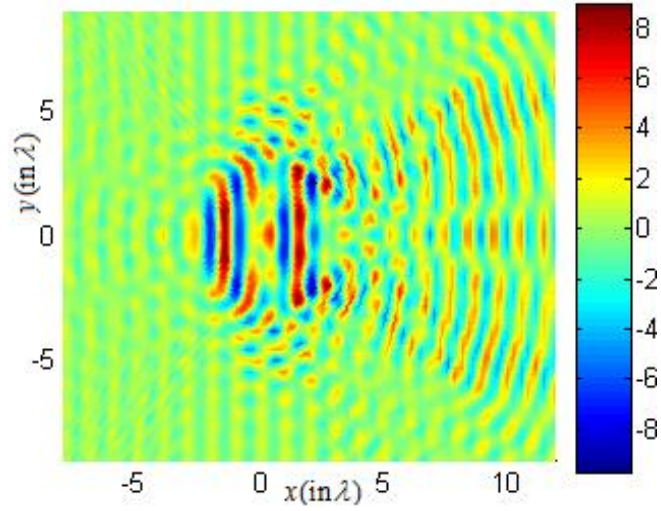


Figure 5. 14: SEM solution to the real of incident-scattered field ( $E_z^{inc} + E_z^s$ ) inside and outside of a magnetodielectric cylinder of radius  $R = 3\lambda$  and with  $\mu_r = 3$  and  $\varepsilon_r = (4 - \mu_r) / (2\mu_r + 1)$ .

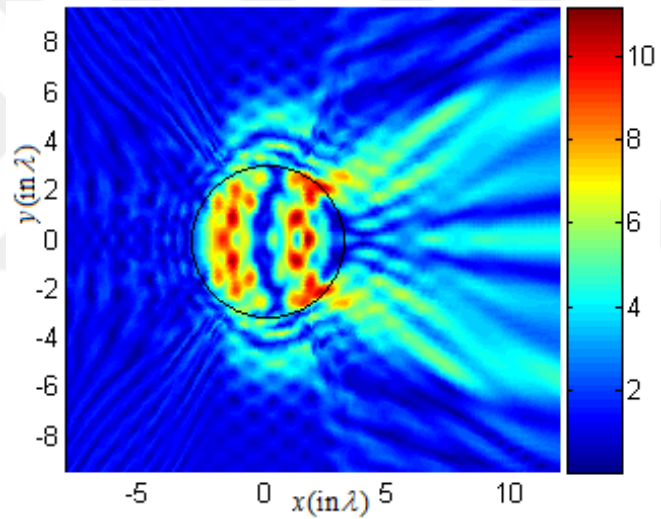


Figure 5. 15:  $|E_z^{inc} + E_z^s|$  inside and outside of a magneto-dielectric cylinder of radius  $R = 3\lambda$  and with  $\mu_r = 3$  and  $\varepsilon_r = (4 - \mu_r) / (2\mu_r + 1)$ .

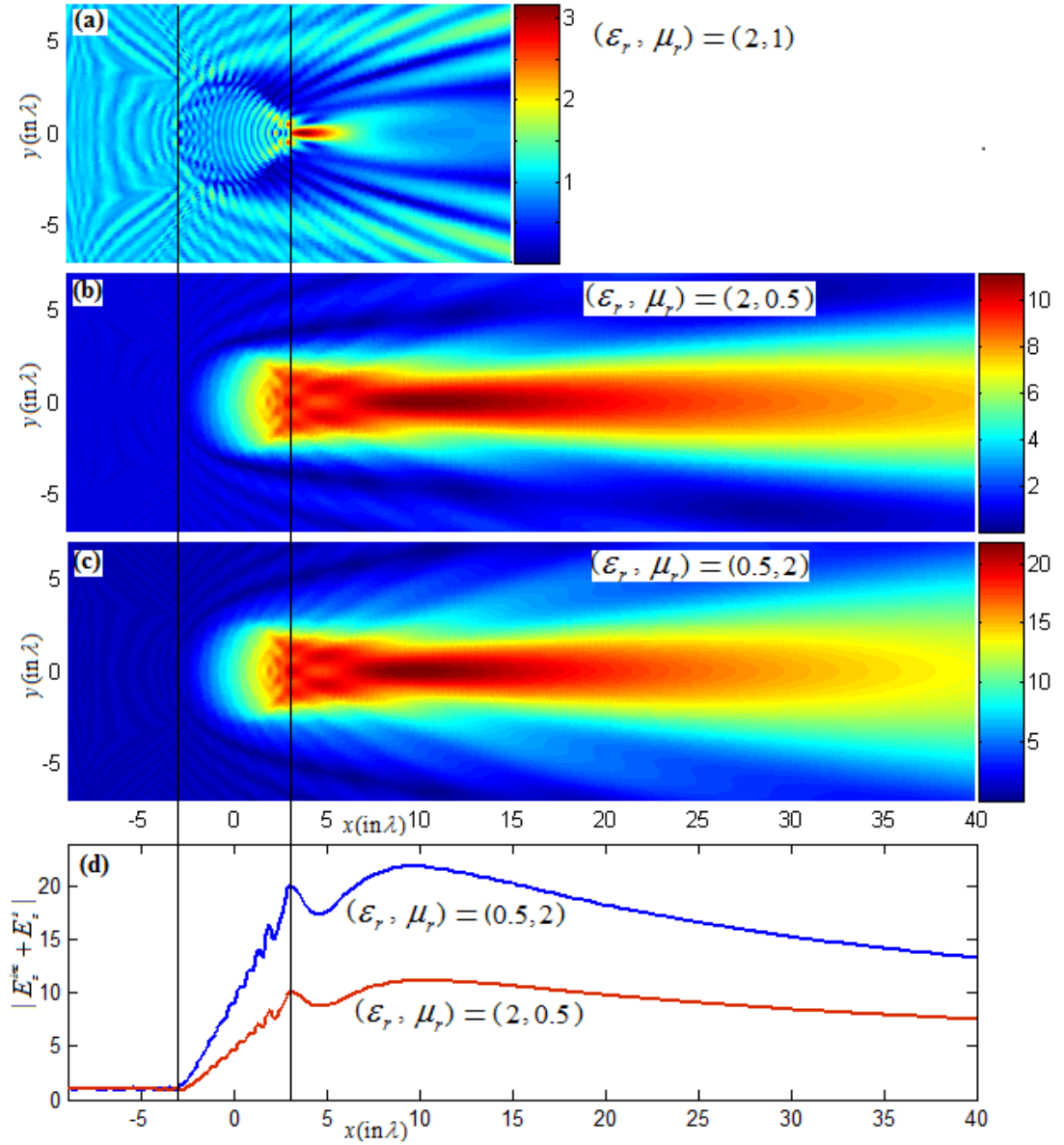


Figure 5. 16: Magnitudes of total fields ( $|E_z^{inc} + E_z^s|$ ) for a micro-cylinder of radius  $R = 3\lambda$ , (a)  $\epsilon_r = 2, \mu_r = 1$ , (b)  $\epsilon_r = 2, \mu_r = 0.5$ , (c)  $\epsilon_r = 0.5, \mu_r = 2$  (c) field magnitudes along propagation direction, i.e., along  $y = 0$ , for the cases in part (a) and (b). Dimensions are normalized with  $\lambda$ .

Recalling the case of small-particle limit of  $n = 1$ , i.e.,  $\epsilon_r = 1 / \mu_r$ , and in order to realize the scattered field distribution associated to this case, we simulate the problem first by assuming that the cylindrical particle is nonmagnetic, i.e.,  $\mu_r = 1$ , and has a radius of  $R = 3\lambda$ . Figure 5.16 (a) shows the magnitude of total field inside and outside the dielectric cylinder whose  $\epsilon_r = 2$ , i.e.,  $n = \sqrt{2}$ . As expected, a typical photonic nanojet behavior is obtained. However, for the case when  $\epsilon_r = 2 = 1 / \mu_r$ , ( $n = 1$ ) the associated field distribution is shown in Figure 5.16(b). Large scattering takes place

behind the cylinder and starts to build up from inside the cylinder. Noteworthy to point that, meanwhile the incident radiation has a unit intensity, the intensity of scattered field is more than a hundred times. Although this large intensity is pointed in Ref. [105] from the derived ratio between forward to backward scatter along the axis of propagation (i.e., along  $y = 0$ ), one may miss the complete picture without inspecting the field distribution.

Moreover, Ref. [105] finds no difference whether  $\epsilon_r > 1$  or  $\mu_r > 1$  as long as  $n = \sqrt{\epsilon_r \mu_r} = 1$ . However this is not the case. Figure 5.16(c) presents the field's magnitude when  $\mu_r = 2 = 1 / \epsilon_r$  and as it can be seen, the magnitude is almost twice that of the case when  $\epsilon_r = 2 = 1 / \mu_r$ , as also shown in the one-dimensional plot along  $y = 0$  in Figure 5.16(d). Based on Eq. (2.5), this difference is expected since both cases have unequal right-hand-side terms.

In addition, it is impossible to solve for the field analytically when objects of irregular geometries are considered. For instance, if an object of square shape is simply considered, numerical methods turn to be the only means by which the solution can be obtained. In Figure 5.17, the total incident-scattered field due to a square cylinder of  $3\lambda \times 3\lambda$  and whose  $\mu_r = 1.4$  and  $\epsilon_r = 1 / 1.4$  is presented. As it can be seen, a normalized intensity of about 530 is obtained although the object has lower permeability than that presented in Figure 5.16 (c). Finally it is worthy to point that the scattered field reduces as permeability approaches 1.

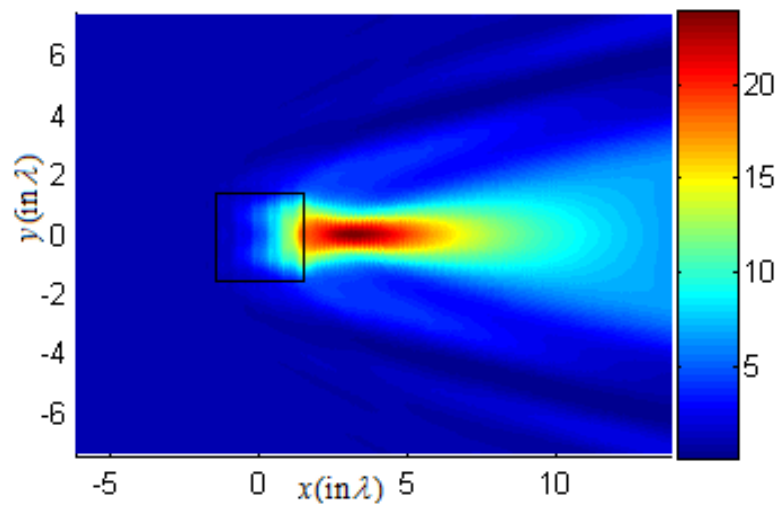


Figure 5. 17:  $|E_z^{inc} + E_z^s|$  inside and outside of a magnetodielectric square cylinder with  $3\lambda \times 3\lambda$  and whose  $\mu_r = 1.4$  and  $\epsilon_r = 1 / 1.4$ .

## 5.4 Conclusion

First, we demonstrated the directional emission from WGM cavity and attributed it to the PNJs generated in the hemicylindrical particle. Although WGMs resonators usually show higher quality factor, hemicylindrical aided PNJs show relatively small influences of WGM regime to PNJ properties. It was also noticed from the study that the quality of a PNJ under back excitation performs better than forward excitation (intensity up to 3 times). In addition, under forward excitation, when the radial mode number increases, the PNJ quality (FWHM, intensity) decreases. For the particles with the non-circular cross-section, the size parameter scaling depends on both the orientation and the shape of the particle. The spatial shape of existing PNJ also does not vary significantly under resonance mode. Thus, WGMs based hemicylindrical PNJs may offer a great promise for the investigation of the fundamentals of light-matter interaction and in the development of wide range of applications such as dynamical filtering devices and sensors. Moreover, due to the scale invariance of Maxwell's equations, obtained results may be scaled to operate in different frequency bands.

Spectral element method is utilized for the study of special dielectric cylinders such that deformations are induced by means of corrugated surfaces. The generated corrugated cylinders are excited under the plane wave illumination and light interaction with the structure is observed. We found that corrugated cylinders may perform in a similar manner to perfectly smooth micro-cylinders under certain conditions while providing nanojet characteristics and focusing property. The results show that one may not need very smooth boundaries to strongly focus light with dielectric micro-cylinders. That is, typical photonic nanojets can be produced.

In terms of the depths of the micro-cylinder's tortuosity investigated in the current paper, the corrugated sub-wavelength light focusing property can be associated with nano-jets and engineering the parameters yield strong field confinement and slowly diffracting beam propagation.

Resonance behavior is captured and it is found that the associated WGM doesn't have strong dependency on the cylinders parameters when compared with that occurs in cylinders with regular boundaries. The significance of the dielectric micro-cylinders as an optical resonator sustaining strong field enhancement is due to the fact that, high-resolution microscopy, near-field imaging, optical lithography, low threshold micro-

cavity lasing, and almost single molecule sensing are feasible thanks to the pioneering studies carried out in the field [77], [79], [112].

Finally, we investigate lossless magneto-dielectric scatterers with cylindrical and square shapes under illuminating with a plane wave by using spectral element method. Lifting the limitation of having non-magnetic case in the study allows engineering the light forward/backward scattering and extremely large forward light intensity enhancement. The presented results will be applied to improve the efficiency and performance of many photonic devices including solar cells, biosensors, lasers, and photo-detectors.



## 6. CONCLUSION

The last three decades have recently seen good progress in computational electromagnetics. The need behind this progress arises from the fact that engineers started to work in the very fine details of complex problems where analytical methods were found to fail in modeling such problems. Finite difference methods were first utilized by engineers during mid of the last century due to the associated simplicity in solving partial differential equations governing a certain system. Soon after, during 1960s, finite element method was devised and utilized as another tool for engineers. In fact, thanks to the continuous improvements in the semiconductor technology that provides a perfect environment for the utilization of numerical methods by means of computers.

In this thesis, the spectral element method, which was devised during mid of 1980s for the purpose of handling the simulation of fluid mechanics, is applied to investigate photonic nanojets. That is, the set of governing equations derived from Maxwell's equations is spatially formulated by the spectral element method as introduced in chapter 2. This set of equations governs the incident and scattered field from an arbitrary object whose magnetic permeability and permittivity are provided. Here, it is noteworthy to point out that most of electromagnetic problems are unbounded. Therefore, the perfectly matched layer is utilized to truncate the domain in order to find the associated unique solution.

The application of spectral element method to a given domain involves spatial discretization to that domain into elements. The elemental deformation may affect the accuracy offered by the spectral element method. Although we were careful in the choice of elements, spectral element method still dominates other numerical methods under large deformations. To illustrate this fact, in sec. 2.4, we presented a comparison in one and two dimensional problems among SEM, FEM and FDM.

Then, in chapter 3, we numerically investigate scattering of light by a dielectric, non-magnetic cylinder by SEM. We accurately solve scattering by dielectric

microcylinders. Interesting cases, which finite difference time-domain method couldn't capture with a moderate resolution, are presented and discussed in this thesis. Verification of the obtained results is then presented using the analytical solution of Mie theory.

After that, we have both numerically and analytically shown that lossless dielectric cylinders with different refractive index and radii illuminated by a linearly polarized plane wave produce two separate characteristics, whispering gallery mode vs. photonic nano-jets. The resonance condition yields enhanced field localization inside the micro-cylinder. On the other hand, structural deformations ruins the symmetric electric field formation and strong focusing of light at the shadow side of the cylinder appears close to the cylinders' surface. Solutions of high accuracy spectral element method and Mie theory are found to agree well with each other except the case that there is a shift for the resonance condition. In addition, the resonance condition is also investigated under different types of illuminations, that is, Bessel beam and point source are utilized to excite the electromagnetic structures and the resonance behavior is also captured.

In chapter 5, we study the forward and backward plane wave illuminations of hemicylindrical dielectric particles with different radii and refractive indices. Near field effects providing strong field enhancement and narrow beam width are obtained from hemicylindrical particles, which can be associated with whispering gallery modes (WGMs) and photonic nano-jets. In addition, photonic nanojets resulting from corrugated cylinders (with irregular boundaries) under normally incident plane-wave illumination are studied. Different level of corrugations induced at the boundaries of the dielectric micro-cylinders produce strong light focusing as well as photonic nanojet with unique performance compared to perfectly smooth cylinders. Finally, SEM is utilized due to its accuracy to investigate homogenous and isotropic magneto-dielectric micro-cylinders embedded in air background when illuminated by a unit-intensity plane wave. Even though non-magnetic characteristics the of natural materials at the optical frequencies presently limits the practical realization of the investigated magneto-dielectric medium, nano-engineered artificial materials as in the case of metamaterials and transformation optics may provide the desired  $\epsilon_r$  and  $\mu_r$  values.



## REFERENCES

- [1] **A. Kwan, J. Dudley, and E. Lantz**, “Who really discovered Snell’s law?” *Phys. World*, 15(4), 2002.
- [2] **L. Rayleigh**, “On the light from the sky, its polarization and colour,” *Phil. Mag.* Vol. 41, 447–454, 1871.
- [3] **C. F. Bohren and D. R. Huffman**, *Absorption and Scattering of Light by Small Particles*, Wiley, 1998.
- [4] **B. Luk’yanchuk, Y. W. Zheng, and Y. F. Lu**, “Laser cleaning of solid surface: Optical resonance and near-field effects,” *Proc. SPIE*, 4065, 576–587, 2000.
- [5] **H. J. Münzer, M. Mosbacher, M. Bertsch, J. Zimmermann, P. Leiderer, and J. Boneberg**, “Local field enhancement effects for nanostructuring of surfaces,” *J. Microsc.* 202(Pt 1), 129–135, 2001.
- [6] **M. Mosbacher, H.-J. Münzer, J. Zimmermann, J. Solis, J. Boneberg, and P. Leiderer**, “Optical field enhancement effects in laser-assisted particle removal,” *Appl. Phys., A Mater. Sci. Process.* 72(1), 41–44, 2001.
- [7] **Y. W. Zheng, B. S. Luk’yanchuk, Y. F. Lu, W. D. Song, and Z. H. Mai**, “Dry laser cleaning of particles from solid substrates: experiments and theory,” *J. Appl. Phys.* 90(5), 2135–2142, 2001.
- [8] **B. Luk’yanchuk**, 2nd ed., *Laser Cleaning*, World Scientific, 2002.
- [9] **Y. F. Lu, L. Zhang, W. D. Song, Y. W. Zheng, and B. S. Luk’yanchuk**, “Laser writing of a subwavelength structure on silicon (100) surfaces with particle enhanced optical irradiation,” *JETP Lett.* 72(9), 457–459, 2000.
- [10] **P. Leiderer, C. Bartels, J. König-Birk, M. Mosbacher, and J. Boneberg**, “Imaging optical near-fields of nanostructures,” *Appl. Phys. Lett.* 85(22), 5370–5372, 2004.
- [11] **S. M. Huang, M. H. Hong, Y. F. Lu, B. S. Luk’yanchuk, W. D. Song, and T. C. Chong**, “Pulsed laser-assisted surface structuring with optical near-field enhanced effects,” *J. Appl. Phys.* 92(5), 2495–2500, 2002.
- [12] **K. Piglmayer, R. Denk, and D. Bäuerle**, “Laser-induced surface patterning by means of microspheres,” *Appl. Phys. Lett.* 80(25), 4693–4695, 2002.
- [13] **N. Chaoui, J. Solis, C. N. Afonso, T. Fourrier, T. Muehlberger, G. Schrems,**

- M. Mosbacher, D. Bäuerle, M. Bertsch, and P. Leiderer**, “A high-sensitivity in situ optical diagnostic technique for laser cleaning of transparent substrates,” *Appl. Phys., A Mater. Sci. Process.* 76(5), 767–771, 2003.
- [14] **P. Leiderer, C. Bartels, J. König-Birk, M. Mosbacher, and J. Boneberg**, “Imaging optical near-fields of nanostructures,” *Appl. Phys. Lett.* 85(22), 5370–5372, 2004.
- [15] **B. S. Luk'yanchuk, Z. B. Wang, W. D. Song, and M. H. Hong**, “Particle on surface: 3D - effects in dry laser cleaning,” *Appl. Phys., A Mater. Sci. Process.* 79(4-6), 747–751, 2004.
- [16] **A. Heifetz, K. Huang, A. V. Sahakian, X. Li, A. Taflove, and V. Backman**, “Experimental confirmation of backscattering enhancement induced by a photonic jet,” *Appl. Phys. Lett.* 89(22), 221118, 2006.
- [17] **S.-C. Kong, A. Sahakian, A. Heifetz, A. Taove, and V. Backman**, “Robust detection of deeply subwavelength pits in simulated optical data-storage disks using photonic jets,” *Appl. Phys. Lett.* 92(21), 211102, 2008.
- [18] **S. Yang, A. Taflove, and V. Backman**, “Experimental confirmation at visible light wavelengths of the backscattering enhancement phenomenon of the photonic nanojet,” *Opt. Express* 19(8), 7084–7093, 2011.
- [19] **V. N. Astratov, J. P. Franchak, and S. P. Ashili**, “Optical coupling and transport phenomena in chains of spherical dielectric microresonators with size disorder,” *Appl. Phys. Lett.* 85(23), 5508–5510, 2004.
- [20] **G. Kattawar, C. Li, P. W. Zhai, and P. Yang**, “Electric and magnetic energy density distributions inside and outside dielectric particles illuminated by a plane electromagnetic wave,” *Opt. Express* 13(12), 4554–4559, 2005.
- [21] **A. V. Itagi and W. A. Challener**, “Optics of photonic nanojets,” *J. Opt. Soc. Am.* A 22(12), 2847–2858, 2005.
- [22] **A. V. Kanaev, V. N. Astratov, and W. Cai**, “Optical coupling at a distance between detuned spherical cavities,” *Appl. Phys. Lett.* 88(11), 2006.
- [23] **K. J. Yi, H. Wang, Y. F. Lu, and Z. Y. Yang**, “Enhanced Raman scattering by self-assembled silica spherical Microparticles,” *J. Appl. Phys.* 101(6), 063528, 2007.
- [24] **S. Lecler, S. Haacke, N. Lecong, O. Crégut, J.-L. Rehspringer, and C.**

- Liu, Y. Zhou, and M. H. Hong**, “Laser micro/nano fabrication in glass with tunable-focus particle lens array,” *Opt. Express* 16(24), 19706–19711, 2008.
- [26] **C. M. Ruiz and J. J. Simpson**, “Detection of embedded ultra-subwavelength-thin dielectric features using elongated photonic nanojets,” *Opt. Express* 18(16), 16805–16812, 2010.
- [27] **T. Wang, C. Kuang, X. Hao, and X. Liu**, “Subwavelength focusing by a microsphere array,” *J. Opt.* 13(3), 035702, 2011.
- [28] **S. Yang, A. Taflove, and V. Backman**, “Experimental confirmation at visible light wavelengths of the backscattering enhancement phenomenon of the photonic nanojet,” *Opt. Express* 19(8), 7084–7093, 2011.
- [29] **A. Darafsheh and V. N. Astratov**, “Periodically focused modes in chains of dielectric spheres,” *Appl. Phys. Lett.* 100(6), 061123, 2012.
- [30] **Z. B. Wang, Z. Yi, and B. Luk’yanchuk**, “Near-field focusing of dielectric microspheres: Super-resolution and field-invariant parameter scaling,” arXiv:1304.4139, 2013.
- [31] **H. Guo, Y. Han, X. Weng, Y. Zhao, G. Sui, Y. Wang, and S. Zhuang**, “Near-field focusing of the dielectric microsphere with wavelength scale radius,” *Opt. Express* 21(2), 2434–2443, 2013.
- [32] **C.-Y. Liu and Y. Wang**, “Real-space observation of photonic nanojet in microspheres,” *Physica E* 61, 141–147, 2014.
- [33] **C.-Y. Liu**, “Ultra-high transmission of photonic nanojet induced modes in chains of core-shell microcylinders,” *Phys. Lett. A* 376(45), 3261–3266, 2012.
- [34] **C.-Y. Liu**, “Superenhanced photonic nanojet by core-shell microcylinders,” *Phys. Lett. A* 376(23), 1856–1860, 2012.
- [35] **Y. Takakura, H. Halaq, S. Lecler, S. Robert, and B. Sauviac**, “Single and dual photonic jets with tipped waveguides: An integral approach,” *IEEE Photonics Technol. Lett.* 24(17), 1516–1518, 2012.
- [36] **C.-Y. Liu**, “Tunable photonic nanojet achieved by core-shell microcylinder with nematic liquid crystal,” *J. Mod. Opt.* 60(7), 538–543, 2013.
- [37] **B. Ounnas, B. Sauviac, Y. Takakura, S. Lecler, B. Bayard, and S. Robert**, “Single and Dual Photonic Jets and Corresponding Backscattering Enhancement With Tipped Waveguides: Direct Observation at Microwave Frequencies,” *IEEE Trans. Antenn. Propag.* 63(12), 5612–5618, 2015.
- [38] **M. Guo, Y. H. Ye, J. Hou, and B. Du**, “Experimental far-field imaging properties of high refractive index microsphere lens,” *Photonics Research* 3(6), 339–342, 2015.

- [39] **C.-Y. Liu and K.-L. Hsiao**, "Direct imaging of optimal photonic nanojets from core-shell microcylinders," *Opt. Lett.* 40(22), 5303–5306, 2015.
- [40] **Z. Chen, A. Taflove, and V. Backman**, "Photonic nanojet enhancement of backscattering of light by nanoparticles: a potential novel visible-light ultramicroscopy technique," *Opt. Express* 12, 1214-1220, 2004.
- [41] **S. Lecler, Y. Takakura, and P. Meyrueis**, "Properties of a three-dimensional photonic jet," *Opt. Lett.* 30(19), 2641–2643, 2005.
- [42] **A. Devilez, B. Stout, N. Bonod, and E. Popov**, "Spectral analysis of three-dimensional photonic jets," *Opt. Express* 16, 14200-14212, 2008.
- [43] **P. Ferrand, J. Wenger, A. Devilez, M. Pianta, B. Stout, N. Bonod, E. Popov, and H. Rigneault**, "Direct imaging of photonic nanojets," *Opt. Express* 16, 6930-6940, 2008.
- [44] **M.-S. Kim, T. Scharf, S. Mühlig, C. Rockstuhl, and H. P. Herzig**, "Engineering photonic nanojets," *Opt. Express* 19, 10206-10220, 2011.
- [45] **Z. Wang, W. Guo, L. Li, B. Luk'yanchuk, A. Khan, Z. Liu, Z. Chen, and M. Hong**, "Optical virtual imaging at 50 nm lateral resolution with a white-light nanoscope," *Nature Commun.* 2, 218, 2011.
- [46] **V. R. Dantham, P. B. Bisht, C. K. R. Nambodiri**, "Enhancement of Raman scattering by two orders of magnitude using photonic nanojet of a microsphere," *J. Appl. Phys.* 109, 103103, 2011.
- [47] **S.-C. Kong, A. Sahakian, A. Taflove, and V. Backman**, "Photonic nanojet-enabled optical data storage," *Opt. Express* 16, 13713-13719, 2008.
- [48] **A. M. Kapitonov and V. N. Astratov**, "Observation of nanojet-induced modes with small propagation losses in chains of coupled spherical cavities," *Opt. Lett.* 32, 409-411, 2007.
- [49] **A. Heifetz, S-C. Kong, A. V. Sahakian, A. Taflove, and V. Backman**, "Photonic nanojets," *J. Comput. Theor. Nanosci.* 6, 1979–1992, 2009.
- [50] **Sadiku, Matthew NO**. Numerical techniques in electromagnetics. CRC press, 2000.
- [51] **D.T. Paris and F.K. Hurd**, *Basic Electromagnetic Theory*, McGraw-Hill, New York, p. 166, 1969.
- [52] **C. W. Steele**, A spectral method for field computation, *IEEE Transactions on Magnetism*, vol. mag-19, 6, 1983.
- [53] **O. Z. Mehdizadeh and M. Paraschivoiu**, "Investigation of a two-dimensional spectral element method for Helmholtz's equation," *Journal. of Computational. Phys.*, vol. 189, pp. 111–129, 2003.

- [54] **J. Lee, T. Xiao, and Q. H. Liu**, “A 3-D spectral-element method using mixed-order curl conforming vector basis functions for electromagnetic fields,” *IEEE Transactions On Microwave Theory and Techniques*, vol. 54-1, pp. 437-444, 2006.
- [55] **J. Lee and Q. H. Liu**, “A 3-D spectral-element time-domain method for electromagnetic simulation,” *IEEE Trans. On Microwave Theory and Technique*, vol. 55-5, pp. 983-991, 2007.
- [56] **J. Lee, J. Chen, and Q. H. Liu**, “A 3-D Discontinuous Spectral Element Time-Domain Method for Maxwell’s Equations”, *IEEE Transactions on Antennas and Propagation*, vol. 57, no. 9, 2009.
- [57] **J. Lee, J. Chen, and Q. H. Liu**, “A 3-D Discontinuous Spectral Element Time-Domain Method for Maxwell’s Equations”, *IEEE Transactions on Antennas and Propagation*, vol. 57, no. 9, 2009.
- [58] **Chen, Jiefu, Joon-Ho Lee, and Qing Huo Liu**, "A High-Precision Integration Scheme for the Spectral-Element Time-Domain Method in Electromagnetic Simulation”, *IEEE Transactions on Antennas and Propagation*, vol. 57, no. 10, 2009.
- [59] **I. Mahariq, H. Kurt, H. I. Tarman, and M. Kuzuoğlu**, “Photonic Nanojet Analysis by Spectral Element Method”, *IEEE Photonics Journal*, 6(5), pp. 1-14, 2014.
- [60] **I. Mahariq, and H. Kurt**, “On- and off-optical-resonance dynamics of dielectric microcylinders under plane wave illumination”, *Journal of the Optical Society of America B*, Vol. 32.6, pp. 1022-1030, 2015.
- [61] **I. Mahariq, V. Astratov, and H. Kurt**, “Persistence of photonic nanojet formation under the deformation of circular boundary”, *Journal of the Optical Society of America B*, 33.4: 535-542, 2016.
- [62] **I. Mahariq, and H. Kurt**, “Strong field enhancement of resonance modes in dielectric micro-cylinders”, *Journal of the optical society of America B*, 33.4, 656-662, 2016.
- [63] **I. Mahariq, H. Kurt, and M. Kuzuoğlu**, “Questioning Degree of Accuracy Offered by the Spectral Element Method in Computational Electromagnetics”, *Applied Computational Electromagnetics Society Journal*, vol. 22.7, 2015.
- [64] **I. Mahariq, N. Eti, and H. Kurt** “Engineering Photonic Nano-jet Generation ”, *Computational Electromagnetics International Workshop*, July 4-6, 2015. Izmir, Turkey.
- [65] **N. Eti, I. Mahariq, and H. Kurt** “Mode Analysis and Light Confinement of

Optical Rib Waveguides in Various Air Slot Configurations”, 17th International Conference on Transparent Optical Networks, July 5-9, 2015, Budapest, Hungary.

- [66] **A.T. Patera**. A spectral element method for fluid dynamics: Laminar flow in a channel expansion. *Journal of Computational Physics*, 54:468–488, 1984.
- [67] **Deville, Michel O., Paul F. Fischer, and Ernest H. Mund**, High-order methods for incompressible fluid flow. Vol. 9. Cambridge University Press, 2002.
- [68] **Karniadakis, George, and Spencer Sherwin**. Spectral/hp element methods for computational fluid dynamics. Oxford University Press, 2013.
- [69] **M. Kuzuoglu, and R. Mittra**, "A systematic study of perfectly matched absorbers," *Frontiers in Electromagnetics*, IEEE Press, 2000.
- [70] **S. J. Hesthaven, S. Gottlieb, and D. Gottlieb**, Spectral methods for time-dependent problems, Cambridge University Press, 2007.
- [71] **O. Deville, F. P. Fischer, and E. Mund**, High-order methods for incompressible fluid flow, Vol. 9. Cambridge University Press, 2002.
- [72] **J. W. Gordon, and A. C. Hall**, "Transfinite element methods: blending-function interpolation over arbitrary curved element domains," *Numer. Math*, vol. 21.2, pp. 109-129, 1973.
- [73] **W. J. Wiscombe**, "Improved Mie scattering algorithms," *Appl. Opt.* 19, 1505–1509, 1980.
- [74] **V. E. Cachorro and L. L. Salcedo**, "New improvements for Mie scattering calculations," *J. Electromagn. Waves Appl.* 5, 913–926, 1991.
- [75] **W. Hergert and T. Wriedt**. Mie Theory 1908–2008 Present developments and interdisciplinary aspects of light scattering, Univ. Bremen, 2008.
- [76] **S.V. Boriskina and L. Dal Negro**, "Self-referenced photonic molecule bio chemical sensors", *Opt. Lett.*, Vol 35, no. 14, 2496-2498, 2010.
- [77] **S.V. Boriskina**, "Spectrally-engineered photonic molecules as optical sensors with enhanced sensitivity: a proposal and numerical analysis" *J. Opt. Soc. Am. B*, 23, 1565-1573, 2006.
- [78] **H. Kurt and M. Turduev**, "Generation of a two-dimensional limited-diffraction beam with self-healing ability by annular-type photonic crystals," *Journal of Optical Society of America B*, 29, 1245, 2012.
- [79] **Y. Li, A. V. Maslov, N. I. Limberopoulos, A. M. Urbas, and V. Astratov**, "Spectrally resolved resonant propulsion of dielectric microspheres," *Laser Photonics Review*, 9, 263, 2015.

- [80] **R.K. Chang and Y.-Le Pan**, “Linear and non-linear spectroscopy of microparticles: Basic principles, new techniques and promising applications,” *Faraday Discuss.* 137, 9-36, 2008.
- [81] **I. V. Minin and O. V. Minin**, *Diffraction optics and nanophotonics: Resolution below the diffraction limit.* Springer, 2015.
- [82] **B. Born, J. D. Krupa, S. Geoffroy-Gagnon, and J. F. Holzman**, “Integration of photonic nanojets and semiconductor nanoparticles for enhanced alloptical switching,” *Nature Communications.* 6, 8097, 2015.
- [83] **J. F. Owen, R. K. Chang, and P. W. Barber**, “Internal electric field distributions of a dielectric cylinder at resonance wavelengths,” *Opt. Lett.* 6, 540-542, 1981.
- [84] **D. S. Benincasa, P. W. Barber, J. Z. Zhang, W. F. Hsieh, and R. K. Chang**, “Spatial distribution of the internal and near-field intensities of large cylindrical and spherical scatters,” *Appl. Opt.* 26, 1348-1356, 1987.
- [85] **L. Rayleigh**, “The problem of the Whispering Gallery,” *Philosophical Magazine.* 20, 1001-1004, 1910.
- [86] **G. C. Righini, Y. Dumeige, P. Féron, M. Ferrari, G. Conti, D. Ristic, and S. Soria**, “Whispering gallery mode microresonators: Fundamentals and applications,” *Rivista del Nuovo Cimento.* 34, 435-490, 2011.
- [87] **A. Chiasera, Y. Dumeige, P. Féron, M. Ferrari, Y. Jestin, G.N. Conti, S. Pelli, S. Soria, and G.C. Righini**, “Spherical whispering-gallery-mode microresonators,” *Laser and Photonics Reviews.* 4, 457-482, 2010.
- [88] **M. L. Gorodetsky, A. A. Savchenkov, V. S. Ilchenko**, “Ultimate Q of optical microsphere resonators,” *Optics Letters.* 21, 453-455, 1996.
- [89] **M. L. Gorodetsky, A. E. Fomin**, “Geometrical theory of whispering-gallery modes,” *IEEE Journal of Selected Topics in Quantum Electronics.* 12, 33-39, 2006.
- [90] **M. H. Fields, J. Popp, and R. K. Chang**, “Nonlinear optics in microspheres,” *Progress in Optics.* 41, 1-96, 2000.
- [91] **A. Coillet, R. Henriot, K. Huy, M. Jacquot, L. Furfaro, I. Balakireva, L. Larger, Y. Chembo**, “Microwave photonics systems based on whispering-gallery mode resonators,” *J Vis Exp.* 78, 610, 2013.
- [92] **P. W. Barber and S. C. Hill**, “Light Scattering by Particles: computational methods,” *World Scientific.* 2, 1990.
- [93] **M. J. Mendes, I. Tobias, A. Marti, and A. Luque**, “Light Concentration in the Near Field of Dielectric Spheroidal Particles with Mesoscopic Sizes,” *Opt. Express.* 19, 16207–16222, 2011.

- [94] **A. Heifetz, J. J. Simpson, S. C. Kong, A. Taflove, V. Backman**, “Subdiffraction optical resolution of a gold nanosphere located within the nanojet of a Mie-resonant dielectric microsphere,” *Optics Express*. 15, 17334-17342, 2007.
- [95] **S. Lee, L. Li and Z. Wang**, “Optical resonances in microsphere photonic nanojets,” *Journal of Optics*. 16, 15704, 2014.
- [96] **N. Eti, I. H. Giden, Z. Hayran, B. Rezaei, and H. Kurt**, "Manipulation of photonic nanojet using liquid crystals for elliptical and circular core-shell variations," published online in *Journal of Modern Optics*, 2017.
- [97] **C. Y. Liu**, “Photonic nanojet shaping of dielectric non-spherical microparticles,” *Physica E*. 64, 23–28, 2014.
- [98] **Y. Chongchang, Q. Cheng, Z. Wen, W. Yue, and W. Huaping**, “The design and manufacture of profiled multi-channeled hollow polyester fibers,” *Fibers and Polymers* 10, pp. 657-661, 2009.
- [99] **O. Podrazký, I. Kašík, P. Peterka, J. Aubrecht, J. Cajzl, J. Proboštová, and V. Matějec**, “Preparation of optical fibers with non-circular cross-section for fiber lasers and amplifiers,” *Proc. of SPIE Vol. 9450, 94501A*, 2015.
- [100] **S.-H. Gong, S.-M. Ko, M.-H. Jang, and Y.-H. Cho**, “Giant Rabi splitting of whispering gallery polaritons in GaN/InGaN core-shell wire,” *Nano Lett.* 15, pp 4517–4524, 2015.
- [101] **C. Xu, J. Dai, G. Zhu, G. Zhu, Y. Lin, J. Li, and Z. Shi**, “Whispering-gallery mode lasing in ZnO microcavities,” *Laser Photonics Rev.* 8, pp. 469–494, 2014.
- [102] **J. Heebner, R. Grover, T. Ibrahim, and T. A. Ibrahim**, *Optical Micro Resonators: Theory, Fabrication, and Applications*, Springer, 2007.
- [103] **A. B. Matsko and V. S. Ilchenko**, “Optical resonators with whispering-gallery modes,” *IEEE J. Sel. Top. Quantum Electron.* 12(15), 2006.
- [104] **M. S. Kim, T. Scharf, S. Mühlig, C. Rockstuhl, and H. P. Herzig**, “Photonic nanojets,” *Opt. Express* 19, 10206, 2011.
- [105] **M. Kerker, D. S. Wang, and C. L. Giles**, “Electromagnetic scattering by magnetic spheres,” *J. Opt. Soc. Am.* 73, 765–767, 1983.
- [106] **A. Alú and N. Engheta**, “How does zero forward-scattering in magneto dielectric nanoparticles comply with the optical theorem,” *J. Nanophoton.* 4(1), 041590, 2010.
- [107] **B. García-Cámara, F. González, F. Moreno, and J. M. Saiz**, “Exception for the zero-forward-scattering theory,” *J. Opt. Soc. Am. A* 25, 2875, 2008.



- [108] **B. García-Cámara, J. M. Saiz, F. González, and F. Moreno**, “Nanoparticles with unconventional scattering properties: Size effects” *Opt. Commun.* 283, 490, 2010.
- [109] **R.V. Mehta, R. Patel, R. Desai, R.V. Upadhyay, and K. Parekh**, “Experimental evidence of zero forward scattering by magnetic spheres,” *Phys. Rev. Lett.* 96, 127402, 2006.
- [110] **B. García-Cámara, F. Moreno, F. González, and J. M. Saiz**, “Comment on ‘Experimental evidence of zero forward scattering by magnetic spheres’,” *Phys. Rev. Lett.* 98, 179701, 2007.
- [111] **H. Ramachandran and N. Kumar**, “Comment on ‘Experimental evidence of zero forward scattering by magnetic spheres’,” *Phys. Rev. Lett.* 100, 229703, 2008.
- [112] **Y. E. Geints, A. A. Zemlyanov, E. K. Panina**, “Photonic jets from resonantly excited transparent dielectric microspheres,” *J. Opt. Soc. Am. B*, 29(4), pp. 758-762, 2012.
- [113] **F. A. Pinheiro, A. S. Martinez, and L. C. Sampaio**, “New effects in light scattering in disordered media and coherent backscattering cone: system of magnetic particles,” *Phys. Rev. Lett.* vol. 84, pp. 1435–1438, 2000.
- [114] **F. A. Pinheiro, A. S. Martinez, and L. C. Sampaio**, “Vanishing of energy transport and diffusion constant of electromagnetic waves in disordered magnetic media,” *Phys. Rev. Lett.* vol. 85, pp. 5563–5566, 2000.
- [115] **F. A. Pinheiro, A. S. Martinez, and L. C. Sampaio**, “Multiple scattering of electromagnetic waves in disordered magnetic media: localization parameter, energy transport velocity and diffusion constant,” *Braz. J. Phys.* vol. 31, pp. 65–70, 2001.
- [116] **F. A. Pinheiro, A. S. Martinez, and L. C. Sampaio**, “Electromagnetic scattering by small magnetic particles,” *J. Magn. Mater.* vol. 226, pp. 1951–1953, 2001.
- [117] **J. Geffrin, B. García-Cámara, R. Gómez-Medina, P. Albella, L. Froufe-Pérez, C. Eyraud, A. Litman, R. Vaillon, F. González, M. Nieto-Vesperinas, J. J. Sáenz, and F. Moreno**, “Magnetic and electric coherence in forward- and back-scattered electromagnetic waves by a single dielectric subwavelength sphere,” *Nat. Commun.* vol. 3, pp. 1171, 2012.



## APPENDIX

This is a sample code for meshing a cylinder

```
% Define the bounding curves in terms of s and t
```

```
XAB=inline('y'); YAB=A(2)*Ls1(S) + B(2)*Ls2(S);
```

```
XBC=B(1)*Lt1(T) + C(1)*Lt2(T); YBC=B(2)*Lt1(T) + C(2)*Lt2(T);
```

```
XDC=D(1)*Ls1(S) + C(1)*Ls2(S); YDC=D(2)*Ls1(S) + C(2)*Ls2(S);
```

```
XAD= A(1)*Lt1(T) + D(1)*Lt2(T);YAD=A(2)*Lt1(T) + D(2)*Lt2(T);
```

```
% Construct the maps (x,y)=(F(s,t),G(s,t))
```

```
X(:,:,elmt) = XAB(-sqrt(R^2-(YAB).^2)).*Lt1(T) + XDC.*Lt2(T) + ...
```

```
    XAD.*Ls1(S) + XBC.*Ls2(S) - ...
```

```
    A(1)*Ls1(S).*Lt1(T) - ...
```

```
    B(1)*Ls2(S).*Lt1(T) - ...
```

```
Y(:,:,elmt) = YAB.*Lt1(T) + YDC.*Lt2(T) + ...
```

```
    YAD.*Ls1(S) + YBC.*Ls2(S) - ...
```

```
    A(2)*Ls1(S).*Lt1(T) - ...
```

```
    B(2)*Ls2(S).*Lt1(T) - ...
```

```
    C(2)*Ls2(S).*Lt2(T) - ...
```

```
    D(2)*Ls1(S).*Lt2(T);
```

```
% Compute the Jacobian
```

```
J = abs((Ds * X(:,:,elmt))' .* (Dt * Y(:,:,elmt)) - (Dt * X(:,:,elmt)) .* (Ds * Y(:,:,elmt))');
```

```
Area(:,:,elmt) = wt' * J * ws;
```

```
% Compute the metrics
```

```
DsDx=(Dt * Y(:,:,elmt))./J;
```

```

DsDy=-(Dt * X(:, :, elmt))./J;
DtDx=-(Y(:, :, elmt) * Ds')./J;
DtDy=(X(:, :, elmt) * Ds')./J;
for p=1:Ntp, for q=1:Nsp
    G11(p,q)=wt(p)*ws(q)*(DsDx(p,q)*DsDx(p,q)+DsDy(p,q)*DsDy(p,q))*J(p,q);
    G12(p,q)=wt(p)*ws(q)*(DsDx(p,q)*DtDx(p,q)+DsDy(p,q)*DtDy(p,q))*J(p,q);
    G22(p,q)=wt(p)*ws(q)*(DtDx(p,q)*DtDx(p,q)+DtDy(p,q)*DtDy(p,q))*J(p,q);
    Jw(p,q)=wt(p)*ws(q)*J(p,q)    ;
end, end
G(:, :, elmt)=[diag(G11(:)) diag(G12(:)); diag(G12(:)) diag(G22(:))];
ML(:, :, elmt)=diag(Jw(:));
H(:, :, elmt)=DD'*G(:, :, elmt)*DD-Mur*ks*Epsr*ML(:, :, elmt);
% Second element
elmt=2;
A=[-R/3 R/3]; B=[-R/3 0]; C=[R/3 0]; D=[R/3 R/3];
XAB=A(1)*Ls1(S) + B(1)*Ls2(S); YAB=A(2)*Ls1(S) + B(2)*Ls2(S);
XBC=B(1)*Lt1(T) + C(1)*Lt2(T); YBC=B(2)*Lt1(T) + C(2)*Lt2(T);
XDC=D(1)*Ls1(S) + C(1)*Ls2(S); YDC=D(2)*Ls1(S) + C(2)*Ls2(S);
XAD= A(1)*Lt1(T) + D(1)*Lt2(T); YAD=A(2)*Lt1(T) + D(2)*Lt2(T);

% Construct the maps (x,y)=(F(s,t),G(s,t))
X(:, :, elmt) = XAB.*Lt1(T) + XDC.*Lt2(T) + ...
    XAD.*Ls1(S) + XBC.*Ls2(S) - ...
    A(1)*Ls1(S).*Lt1(T) - ...
    B(1)*Ls2(S).*Lt1(T) - ...
    C(1)*Ls2(S).*Lt2(T) - ...
    D(1)*Ls1(S).*Lt2(T);

```

```

Y(:,:,elmt) = YAB.*Lt1(T) + YDC.*Lt2(T) + ...
    YAD.*Ls1(S) + YBC.*Ls2(S) - ...
    A(2)*Ls1(S).*Lt1(T) - ...
    B(2)*Ls2(S).*Lt1(T) - ...
    C(2)*Ls2(S).*Lt2(T) - ...
    D(2)*Ls1(S).*Lt2(T);

% Compute the Jacobian

J = abs((Ds * X(:,:,elmt))' .* (Dt * Y(:,:,elmt)) - (Dt * X(:,:,elmt)) .* (Ds *
Y(:,:,elmt)')));
Area(:,:,elmt) = wt' * J * ws;

% Compute the metrics

DsDx=(Dt * Y(:,:,elmt))./J;
DsDy=-(Dt * X(:,:,elmt))./J;
DtDx=-(Y(:,:,elmt) * Ds')./J;
DtDy=(X(:,:,elmt) * Ds')./J;

for p=1:Ntp, for q=1:Nsp
    G11(p,q)=wt(p)*ws(q)*(DsDx(p,q)*DsDx(p,q)+DsDy(p,q)*DsDy(p,q))*J(p,q);
    G12(p,q)=wt(p)*ws(q)*(DsDx(p,q)*DtDx(p,q)+DsDy(p,q)*DtDy(p,q))*J(p,q);
    G22(p,q)=wt(p)*ws(q)*(DtDx(p,q)*DtDx(p,q)+DtDy(p,q)*DtDy(p,q))*J(p,q);
    Jw(p,q)=wt(p)*ws(q)*J(p,q)    ;
end, end

G(:,:,elmt)=[diag(G11(:)) diag(G12(:)); diag(G12(:)) diag(G22(:))];
ML(:,:,elmt)=diag(Jw(:));
H(:,:,elmt)=DD'*G(:,:,elmt)*DD-Mur*ks*Epsr*ML(:,:,elmt);

```



## **CURRICULUM VITAE**

**Name-Surname** : Ibrahim MAHARIQ  
**Country** : Turkey  
**Date of birth and place** : 05-02-1980, Palestine  
**E-mail** : ibmahariq@gmail.com

### **Education:**

- **BSc** : Department of Electrical & Computer Eng. Palestine Polytechnic University
- **MSc** : Department of Electrical and Electronics Engineering, Middle East Technical University.
- **PhD1** : Department of Engineering Sciences, Middle East Technical University
- **PhD2** : Department of Electrical and Electronics Engineering, TOBB Economic and Technology University,

**Languages** : Arabic, English, Turkish

### **Publications:**

- **I. Mahariq**, H. Kurt, H. I. Tarman, and M. Kuzuoğlu, “Photonic Nanojet Analysis by Spectral Element Method”, IEEE Photonics Journal, 6(5), pp. 1-14, 2014.
- **I. Mahariq**, and H. Kurt, “On- and off-optical-resonance dynamics of dielectric microcylinders under plane wave illumination”, Journal of the Optical Society of America B, Vol. 32.6, pp. 1022-1030, 2015.

- **I. Mahariq**, V. Astratov, and H. Kurt, “Persistence of photonic nanojet formation under the deformation of circular boundary”, *Journal of the Optical Society of America B*, 33.4: 535-542, 2016.
- **I. Mahariq**, and H. Kurt, “Strong field enhancement of resonance modes in dielectric micro-cylinders”, *Journal of the Optical Society of America B*, 33.4: 656-662, 2016.
- **I. Mahariq**, H. Kurt, and M. Kuzuoğlu, “Questioning Degree of Accuracy Offered by the Spectral Element Method in Computational Electromagnetics”, *Applied Computational Electromagnetics Society Journal*, vol. 22.7, 2015.
- **I. Mahariq**, N. Eti, and H. Kurt, “Engineering Photonic Nano-jet Generation”, *Computational Electromagnetics International Workshop*, July 4-6, 2015. Izmir, Turkey.
- N. Eti, **I. Mahariq**, and H. Kurt, “Mode Analysis and Light Confinement of Optical Rib Waveguides in Various Air Slot Configurations”, *17th International Conference on Transparent Optical Networks*, July 5-9, 2015, Budapest, Hungary.  
The following manuscripts are currently under review:
- **I. Mahariq** and H. Kurt, “Investigation of Strong Field Enhancement Resulting from Magnetodielectric Cylinders”, *IEEE Photonics Technology Letters*.
- **I. Mahariq**, H. Giden, I. V. Minin, O. V. Minin, and H. Kurt “Strong electromagnetic field localization near the surface of hemicylindrical particles”, *Optical and Quantum Electronics*.